Investigation of Small Molecule Diffusion in Complex Fluids Using Fluorescence Correlation Spectroscopy

A Thesis Presented for the

Master of Science

Degree

The University of Tennessee, Knoxville

Grant Allen Foley

December 2024

Copyright © 2024 by Grant Allen Foley

All rights reserved.

ACKNOWLEDGEMENTS

To my Mom, Dad, and brother, Sam, thank you for all of your love and support, without which none of this would be possible.

ABSTRACT

Complex fluids are a class of liquids whose microscopic heterogeneity has proven advantageous in several biological and industrial applications. While rheological and structural characterization studies have been the primary forms of examining complex fluids, the translational diffusion behavior of small molecules within these systems has been less explored. Fluorescence correlation spectroscopy (FCS) is a useful technique for measuring translational diffusion rates of small molecules based on fluorescence intensity fluctuations arising from fluorophores moving through a small volume of focused laser light. Here, an FCS instrument utilizing two-photon excitation has been fully constructed and calibrated, and the examination of small molecule dynamics within two classes of complex fluids, bicontinuous microemulsions and giant unilamellar vesicles, using FCS will be presented. In the bicontinuous microemulsion study, specific focus was given to the impact of surfactant structure on small molecule diffusion. It was concluded that the length of the head group and overall size and bulkiness of the surfactant in the interfacial layer provided the largest impact on probe diffusion. For the GUV studies, bacterial cellular membranes contain branched chain fatty acids, contrasting with mammalian cells that contain unsaturated lipids. FCS results have revealed that GUVs containing a branched chain fatty acid display higher fluidity than membranes with unsaturated lipids. While preliminary results have been obtained for the GUVs, further studies incorporating additional bacterial membrane specific components are still needed to obtain a more cohesive picture of bacterial membrane dynamics.

TABLE OF CONTENTS

CHAPTER ONE INTRODUCTION 1

1.1 Motivation 1

1.2 Complex Fluid Systems Under Investigation 3

1.2.1 Microemulsions 3

1.2.2 Giant Unilamellar Vesicles 6

CHAPTER TWO INSTRUMENTATION AND TECHNIQUE 10

2.1 One-Photon and Two-Photon Fluorescence 10

2.1.1 Two-Photon Fluorescence 11

2.1.2 Requirements for 2PE 13

2.2 Diffusion 15

2.3 Fluorescence Correlation Spectroscopy 17

2.3.1 Mathematical Basis and Correlation 18

2.4 Constructed Instrument 22

2.4.1 Calibration 25

CHAPTER THREE BICONTINUOUS MICROEMULSION STUDIES 29

3.1 Motivation 29

3.2 Sample Preparation 31

3.3 FCS Results 33

3.3.1 FCS Results in Nonionic Surfactant Bicontinuous Microemulsions 33

3.3.2 FCS Results in Ionic Surfactant Bicontinuous Microemulsions 44

3.4 Further Investigation of Interfacial Dynamics and Probe Rotational Diffusion 51

3.4.1 Microviscosity Calculations and Discussion 51
3.4.2 Generalized Polarization of Laurdan 54
3.4.3 Steady State Anisotropy 57
3.5 Conclusion 59
CHAPTER FOUR GUV STUDIES 61
4.1 Motivation 61
4.2 Sample Preparation 64
4.3 Study of GUVs Containing BCFAs 68
4.3.1 Adhesion Method Tests 68
4.3.2 Further Focal Volume Characterization and Positioning for FCS Studies 69
4.3.3 FCS Experiments on a GUV Containing a Branched Chain Lipid 72
4.4 Conclusion 76
CHAPTER FIVE CONCLUSIONS AND FUTURE DIRECTIONS 78
BIBLIOGRAPHY 81
VITA 109

LIST OF TABLES

Table 1. Calculated microviscosity values for A546 in each microemulsion. 53

Table 2. Calculated microviscosities in each BμE based on diffusion coefficients from Rhodamine 53

Table 3. GP values of Laurdan in each bicontinuous microemulsion. The smaller surfactant structures allow for increased water penetration into the interfacial layer. 56

Table 4. Measured anisotropy values and standard deviations in each microemulsion using steady state fluorescence. 59

LIST OF FIGURES

Figure 1. Example of different microemulsion nanostructures. A) Oil in water microemulsion B) Water in oil microemulsion C) Bicontinuous microemulsion. 5

Figure 2. Schematic model of a GUV. The light blue ovals represent the polar head groups of the lipids, and the thin yellow lines represent the hydrophobic lipid tails. 8

Figure 3. Jablonski diagram of one vs two photon excitation. This figure is taken from Reference 58.[71] 12

Figure 4. Illustration describing Fickian diffusion. Molecules diffuse from areas of higher concentration to areas of lower concentration when following Fickian diffusion law. 16

Figure 5. Flow chart depicting the analysis pathway for FCS experiments. 19

Figure 6. Schematic of the TPE-FCS instrument. λ/2 WP = one half waveplate. PBC = polarizing beam splitting cube. PO = pickoff mirror. L1 = first telescope lens. L2 = second telescope lens. DCM = dichroic mirror. NA = numerical aperture. OBJ = objective. nM = nanomolar concentration. EF = emission filters. TL = tube lens. CL= collimating lens. L3, L4 = focusing lenses. APD = avalanche photodiodes. TCSPC = time correlated single photon counting module. 23

Figure 7. Structure of Alexa 546 NHS ester. 27

Figure 8. Representative calibration FCS curve of Alexa 546 NHS ester in MilliQ water. 28

Figure 9. Nonionic surfactant structures. Brij O10 and Triton X-100 possess a large PEO chain head group, which is suspected to penetrate deep into the aqueous layer of the microemulsion. 34

Figure 10: Molecular structures of Rhodamine 6G (Top) and Alexa 546 NHS ester (bottom). . 35

Figure 11. Representative FCS Curves of Rhodamine 6G (Top) and Alexa 546 NHS ester (bottom) in a 25% water BWBI BE. 38

Figure 12. Diffusion coefficients of each probe in all bicontinuous microemulsions. Surfactants with a larger head group restrict the translational diffusion of fluorophores more than smaller head group surfactants. 39

Figure 13. Representative curve of Alexa 546 in a BWBI BμE with 50% water. The diffusion coefficient obtained here is slightly larger than the diffusion coefficient in a 25% water BWBI BμE shown in **Figure 11**. 40

Figure 14. Representative FCS curves of Rhodamine 6G (top) and Alexa 546 NHS (bottom) in a TxBWC BE. 42

Figure 15. Molecular Structure of CTAB (top) and SDS) bottom. CTAB has a positively charged head group, while SDS has a negatively charged head group. 45

Figure 16. FCS correlation curves of Alexa 546 in CBWC (top) and Rhodamine 6G in CBWC (bottom) 46

Figure 17. Representative FCS curves of Rhodamine 6G (top) and Alexa 546 (bottom) in SBWC. 48

Figure 18. Structure of components for GUV Formation. a15:0-i15:0 PC is the BCFA used in this GUV, DPPC is the saturated lipid, and cholesterol is the sterol molecule. 65

Figure 19. Confocal microscopy images of the a15:0-i15:0 PC, DPPC, and cholesterol GUV. The GUV exhibited no phase separation and a homogenous distribution of dye around the entirety of the lipid bilayer. 66

Figure 20. Axial (top) and lateral (bottom) intensity vs. position results obtained from stage scanning through a fluorescently labeled GUV. The results matched the dimensions calculated form FCS calibration methods. 71

Figure 21. FCS result from FM1-43 in a GUV containing a BCFA. The diffusion rate extracted here is faster than those witnessed in unsaturated lipid systems. 74

CHAPTER ONE

INTRODUCTION

1.1 Motivation

In both biology and industry, investigating the inherent physical and chemical properties of small, complicated solutions has been an essential step in medicinal, material, and technological advancement. Oftentimes, while solutions under examination in these fields seem homogeneous to the naked eye, their macroscopic behavior deviates from that of a simple, homogeneous solution because of intricate heterogeneous structures at the microscopic level, which can be manipulated to serve specific purposes. These include, but are not limited to, complex fluids being used in food and beverage products as thickeners and stabilizers,[1] bodily products for cosmetics,[2] paints and coatings,[3] electrochemical applications,[4,5] and oil recovery and drilling fluids in the oil and gas industry.[6] Additionally, naturally occurring biological systems can also fall under the category of complex fluids.[7] Furthermore, cellular membranes, the first line of defense for cells against targeted drug delivery, exhibit complex fluid characteristics due to their multi-component composition of lipids and proteins, which can impact a drug's ability to adsorb to and enter the cell.[8] As such, examining these systems will offer new capabilities to tune these microenvironments for specific biological and industrial applications.

The most studied areas in complex liquids involve examining their rheological properties, phase behavior, and structure. Rheological studies on complex liquids have provided new insight into properties such as viscosity, elasticity, and other flow parameters in complex liquids, [9,10] while structural characterization studies have provided detailed analysis of the mesoscopic

heterogeneity of complex liquids through various scattering techniques like small angle neutron and x-ray scattering[11] and dynamic light scattering.[12,13] However, the diffusion behavior, or the translational and rotational movement, of small molecules placed within these systems, has been less explored in complex fluids. These processes heavily determine the rate of reactions and efficiency of the performance in many of the abovementioned applications. For example, in energy storage applications such as redox flow batteries, the ability of a redox active molecule to transfer from the bulk solution to the electrode surface quickly is vital to these devices' performances.[14–17] In another instance, molecular diffusion processes heavily govern the release mechanisms for drug delivery devices.[18–22] Thus, being able to understand and control the motion of small molecules within complex fluids will assist in new product development for both biological and industrial fields.

Critical to this understanding is an investigation of the microenvironment where diffusion occurs. Oftentimes, the interfacial boundary between the phases of a complex fluid serves as a the primary microenvironment for these reactions to occur by providing a confined region of high affinity for dissolved species, hence increasing the number of actions or reactions towards a desired pathway.[23–25] While researchers have published studies examining diffusion in the interfacial region of complex fluids,[26–31] many open questions remain in certain systems like bicontinuous microemulsions (BμE) and mimetic giant unilamellar vesicles (GUVs). In this thesis, fluorescence correlation spectroscopy (FCS), a technique which measures the translational diffusion rates of molecules through a defined volume of light, is applied to examine the molecular motion within BμE and GUVs. FCS is advantageous due to its high sensitivity, small sample volume, and ability to analyze real-time molecular dynamics non-invasively.[32] The

principles and mathematical basis of FCS, as well as the construction of the FCS instrument, are described in Chapter 2. Next, the investigation of a series of fluorescent probes placed within various microemulsions using FCS and steady state fluorescence spectroscopy resides in Chapter 3. Then, investigation of probe translational diffusion in GUVs with FCS lies in Chapter 4. Finally, conclusions and future directions are detailed in Chapter 5.

Complex Fluid Systems Under Investigation

1.2.1 Microemulsions

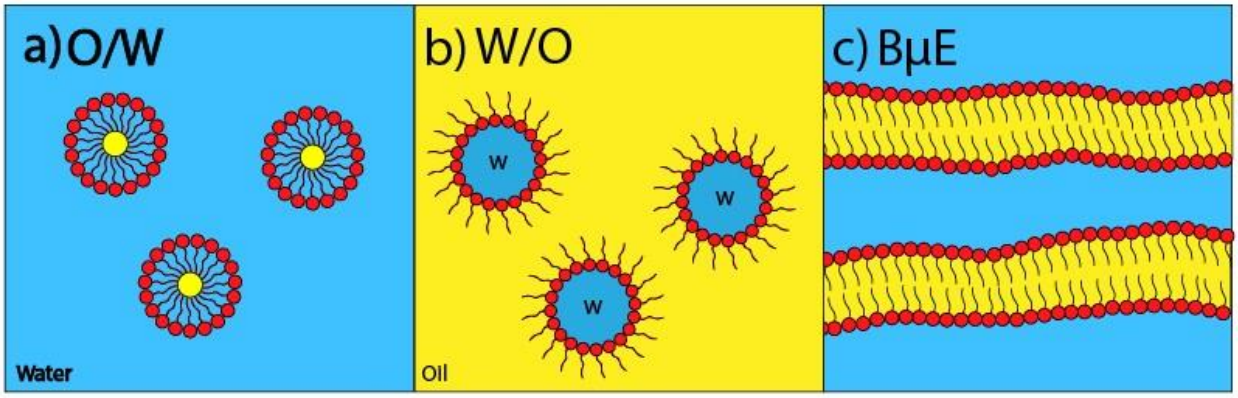
Microemulsions are solutions of an aqueous medium, usually water, hydrocarbons, and stabilizing amphiphilic molecules termed surfactants and/or cosurfactants.[33] While normal emulsions employ two immiscible solutions that form a kinetically stable solution with a low interfacial tension due to the presence of surfactants, they are thermodynamically unstable, leading to phase separation and an opaque appearance. In comparison, by increasing the surfactant concentration and adding a cosurfactant to further reduce the interfacial tension between the immiscible phases, microemulsions are thermodynamically stable solutions with a transparent appearance.[33] This allows microemulsions to form structures that are approximately 500 times smaller than normal emulsions, and the nature of the emulsifying agent dictates the type of microemulsion formed.[34] Specifically, the hydrophilic-lipophilic balance (HLB) and critical packing parameter (CPP) of the surfactant, with a smaller contribution stemming from the ratio of the oil, water, and surfactant phases, drives the formation of the type of microstructure formed.[35] The HLB is a measure of the affinity of a surfactant for the aqueous or nonaqueous phase, while the CPP determines what type of nanostructures will be formed by the

surfactant. The three major phases of microemulsions include oil in water microemulsions (O/W), water in oil microemulsions

(W/O), and bicontinuous microemulsions (BμE). Figure 1 displays the nanoscopic structures of each classification. In an O/W, the HLB of the surfactant favors the aqueous phase, and a water continuous solution with suspended micelles is formed (Fig 1a). Alternatively, when the HLB is shifted to the non-aqueous phase, a W/O system (Fig 1b) of inverse micelles suspended in an oil continuous solution is formed. Finally, when the HLB is balanced, a BμE is formed that produces interconnected channels of the two phases separated by the surfactants (Fig 1c).

As mentioned previously, a central theme to reactions in complex liquids is the reactive species' proximity to the interfacial environment and their translational diffusion capabilities in this region. Some applications, such as electrochemistry,[14] require fast diffusion rates at the interface, while others require slower rates, such as in controlled drug release.[19,36,37] Among these three classifications shown in **Figure 1**, BμEs are of particular interest for examination due to them having the lowest tension interfaces, which is advantageous for mass transfer processes, enhanced mixing of phases, and solubilization of molecules in both phases.[38–41] Because of these advantages, BμEs have been examined for applications in several fields, including use as porous hybrids for polymer materials,[42] electrochemical solutions for redox flow batteries,[4,5,16] biomembrane mimetic systems,[43] environmental decontamination,[44] and controlled drug delivery systems.[45] Despite this significant work, specific factors that can impact the diffusion behavior within BμE, such as the size, structure, and charge of the surfactants, have not been systematically explored. Two specific classes of surfactants that are interesting are nonionic and ionic surfactants. Nonionic surfactants contain a neutral hydrophilic head group, while ionic

Figure 1. Example of different microemulsion nanostructures. A) Oil in water microemulsion B) Water in oil microemulsion C) Bicontinuous microemulsion.



surfactants possess a positively or negatively charged head group. Nonionic surfactants are often more biocompatible and less toxic than their ionic counterparts,[46,47] allowing them to be implemented in agriculture as wetting agents for herbicides and pesticides,[48] in pharmaceuticals as drug solubility improvers,[49] and in cosmetics as emulsifiers and thickeners.[50,51] The majority of nonionic surfactants in industrial use today have polyethoxylated head groups (PEO) with various bulky or linear hydrocarbon tail groups.[46,52] These characteristics provide an interesting opportunity to examine the translational diffusion of small molecules dissolved in BµEs using nonionic surfactants. Cationic and anionic surfactants have also seen tremendous use in household cleaning products, pharmaceutical formulations, road surface coatings, flow battery solutions, etc., with new applications in drug delivery and electrochemistry being investigated.[53–55] These surfactants typically possess smaller, charged head groups compared to their nonionic counterparts. The selection of the correct type of surfactant and active molecule is essential for the successful implementation of this technology in all systems mentioned above. Chapter 3 describes a series of experiments that explore the diffusion of two differently sized and structured fluorescent molecules and four BµEs of differing surfactants and component composition, with attention to the role of the surfactant head group being a primary focus. Furthermore, investigations of the microemulsion structure through microviscosity and generalized polarization are also performed.

1.2.2 Giant Unilamellar Vesicles

Antibiotic resistance has emerged as a significant health concern in the 21st century. In 2019, an estimated 1.27 million deaths were directly caused by antibiotic resistance.[56] In response to this issue, new efforts to combat antibiotic resistance through targeted drug delivery

must be developed. Bacterial cellular membranes are the first line of defense against antibiotic attack, comprised of various lipid molecules that form a bilayer surrounding the internal components of the cell. Lipids, like surfactants, are amphiphilic molecules that possess a hydrophilic head group attached to two hydrophobic tails. In bacterial cells, some lipids can contain hydrophobic tails that possess a small side chain, which are labeled as branched chain fatty acids (BCFAs). These BCFAs are responsible for the fluidity of the bacterial membrane,[57] which in turn affects adsorption of drug molecules and lateral diffusion across the membrane surface. So, understanding the effect on translational diffusion of small, adsorbed molecules within any region of the bilayer by alteration of the tail region of a specific lipid is an essential component for successful drug delivery studies.

An effective way of probing this question is to simplify the interface by forming model membranes with a singular lipid found in bacterial membranes. Giant Unilamellar Vesicles (GUVs) are spherical vessels that contain a hydrophilic core that is surrounded by a bilayer of amphiphilic molecules.[58] These amphiphiles are commonly in the form of low molecular mass phospholipids, block copolymers, or synthetic surfactants. An example of a GUV is shown in **Figure 2**, with a two-dimensional cross section of the vesicle shown on the left and a three-dimensional view shown on the right. The constructed bilayer membrane orients the hydrophilic head groups towards the aqueous medium and the hydrophobic tails oriented towards the inner, hydrophobic region of the bilayer. The bilayer that is formed serves as a biomimetic system mimicking natural cellular membranes, and by selecting a particular type of phospholipid to construct the GUV, these systems can be structured to characterize a particular cellular membrane domain or its interaction with a certain small molecule. While GUVs have been

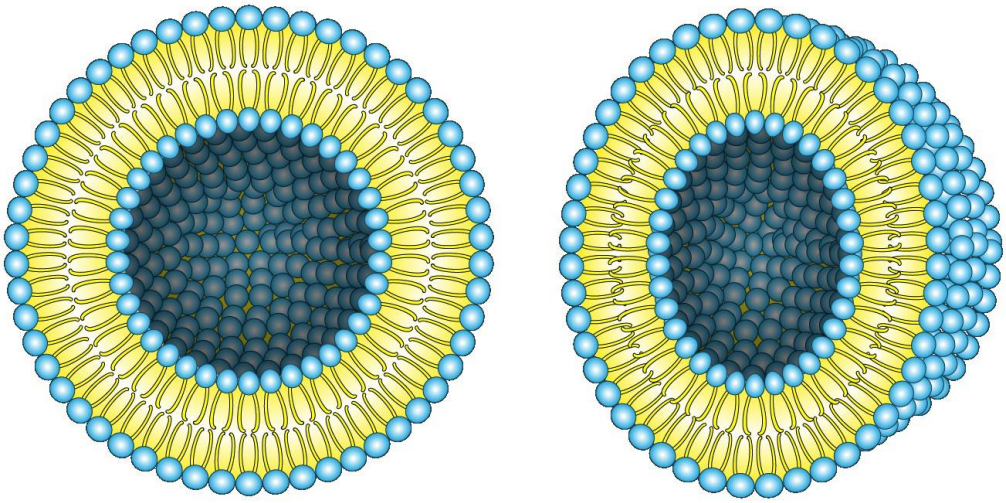


Figure 2. Schematic model of a GUV. The light blue ovals represent the polar head groups of the lipids, and the thin yellow lines represent the hydrophobic lipid tails.

examined for eukaryotic cell studies using FCS,[59–64] investigations of GUVs containing branched chain lipids that are more common in bacterial membranes have yet to be performed. In this thesis, the translational diffusion of small fluorescent molecules placed on the membranes of GUVs containing a branched chain lipid tail is examined with FCS in Chapter 4.

CHAPTER TWO

INSTRUMENTATION AND TECHNIQUE

2.1 One-Photon and Two-Photon Fluorescence

The history of fluorescence can be traced as far back as 1560, when the Aztecs detailed a wood that possessed medicinal properties while also inflicting a change of color on water that was placed on it or in a housing made from the wood.[65] Intrigued by this, a Spanish scientist named Nicholas Monardes authored a report of this medicinal wood in 1577, which went on to inspire numerous scientists to carry out experiments across Europe to understand these peculiar optical phenomena. A particularly interesting series of results came from experiments performed by Lucasian Professor at Cambridge University George Gabriel Stokes in 1852, who is regarded by some as the "Father of Fluorescence". In his work *On the Change of Refrangibility of Light*,[66] which examined the optical properties of quinine sulfate, Stokes proposed that the "epipolic dispersion" of the solution arose from the absorption of light and emission of a longer wavelength light. This principle became known as the Stokes shift, a term that has implanted itself in the foundation of fluorescence studies and terminology. Since then, the study and use of fluorescence to examine specific issues in biological and nonbiological systems has increased immensely.[67–69]

Fluorescence, as described briefly above, is the subsequent emission of electromagnetic radiation in the form of light following an absorbance of light.[65] Delving deeper into this definition, this process can be broken down into three main steps: absorption, nonradiative decay, and radiative decay. Furthermore, to aid in visualizing this behavior, a Jablonski diagram, named after Aleksander Jablonski who first proposed the diagram in 1933,[70] is commonly used. **Figure 3**

displays such a diagram. The horizontal black lines represent different energy levels, with S_0 representing the ground electronic singlet state, S_1 representing the first excited singlet state, and the thinner lines placed above the singlet state lines depicting the various vibrational levels within the electronic states. To begin, energy in the form of electromagnetic radiation, or light, is absorbed by the molecule and an electron is promoted from the ground to the first excited state (blue arrow). Next, the molecule begins to lose energy rapidly by nonradiative methods (NRD), such as vibrational conversion. Finally, the electron will return to the ground electronic state, and in doing so will release energy in the form of a photon (green arrow). Due to the loss in energy from the nonradiative decay processes, the released photon will possess lower energy than the absorbed photon, which demonstrates the Stokes shift principle.

2.1.1 Two-Photon Fluorescence

The mechanism described in the previous section details the base model of fluorescence by using a single photon (1PE) of enough energy to promote an electron to an excited state. However, an alternative method of excitation exists that employs two photons to produce the required energy for promotion (2PE). In 1PE, the energy of the excitation light must be high enough to match the required energy to promote an electron from the ground to state to the excited state[71]. In 2PE, excitation occurs through the near simultaneous absorption of two photons that each possess an energy of half that of the photon used for 1PE. The right side of **Figure 3** demonstrates the principle of 2PE. Photons of a shorter wavelength, or more towards the blue region of the visible light spectrum, have a much higher energy associated with them, requiring only a single photon to provide the needed energy for excitation, as detailed on the left

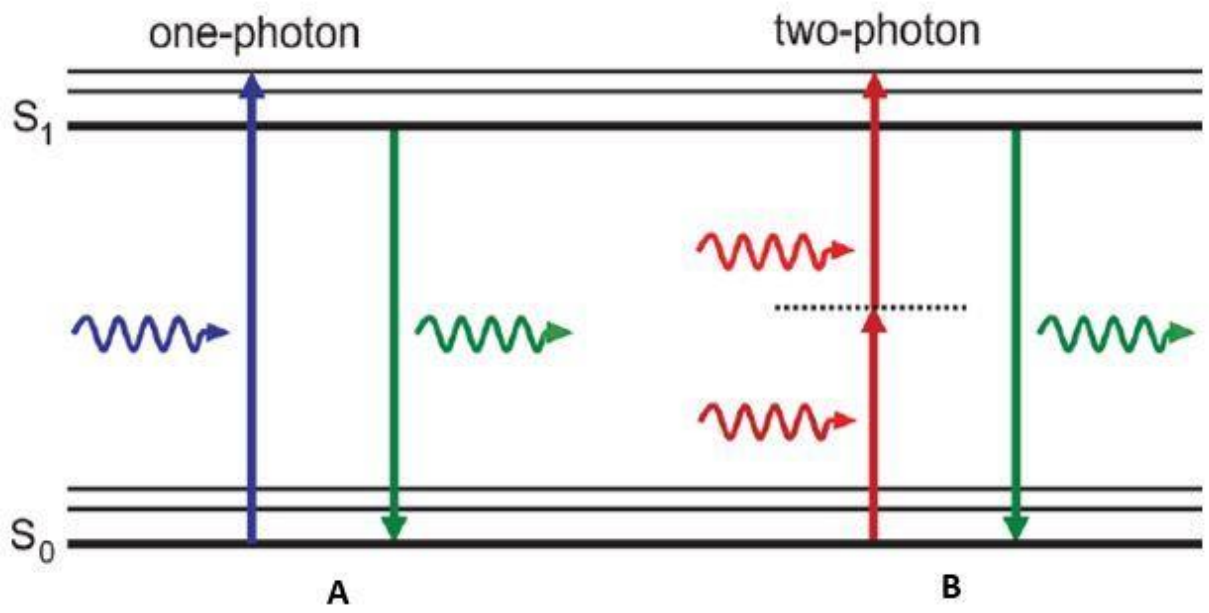


Figure 3. Jablonski diagram of one vs two photon excitation. This figure is taken from Reference 58.[71]

side of **Figure 3**. In contrast, photons with less energy reside on the red to infrared side of the light spectrum, which necessitates two photons to provide sufficient excitation energy, depicted by the right side of **Figure 3**. Compared to 1PE, 2PE offers a few distinct advantages towards this effort. Firstly, 2PE offers significantly reduced photobleaching of fluorescent molecules compared to 1PE due to the lower energy photons used, allowing for longer experiments to be performed with minimal sample or dye damage.[71,72] Secondly, the longer wavelength light used in 2PE offers reduced scattering when in contact with the sample, allowing for deeper penetrating measurements to be performed.[73] This is particularly advantageous for studies interested in behavior in the bulk solution or on surfaces far away from the coverslip-sample interface. Our system utilizes a 2PE excitation scheme, and the details of which will be described in the following sections.

2.1.2 Requirements for 2PE

For each excitation scheme, a light source with a sufficient intensity, selected wavelength, and emission mode are required to cause fluorescent events. Commonly, this is achieved with a laser beam, or a light source that is produced through stimulated emission of radiation. In 1PE, continuous wave lasers, which are pumped consistently by the pump source to produce a constant beam of light, are commonly used. However, the probability of a molecule absorbing two photons at the same time and place from a continuous wave laser is extremely low. Thus, 2PE incorporates an ultrashort pulsed excitation scheme. When light is amplified by a gain medium through stimulated emission, the emitted light waves are reflected inside a laser cavity containing two mirrors, one fully reflective and one partially reflective. These light waves contain many modes, and when these modes constructively interfere with one another through

their in-phase superposition, a pulse of energy is formed. As the waves travel back and forth within the cavity, so too does the generated pulse, and this entire process is known as mode locking. The partially reflective mirror allows the pulses to exit the laser cavity, and the time it takes for the pulse train to complete one round trip of the cavity sets the repetition rate of the laser. This modelocking process causes photons to be emitted with pulse lengths on the order of picoseconds (10^{-12}) to femtoseconds (10^{-15}) at a MHz (10^{6} s^{-1}) repetition rate.[74] This form of laser generation accounts for the time aspect of 2PE, but in order to have the photons arrive at the same location simultaneously, a focusing of the laser beam to an nanometer sized spot is required. This is achieved with a high numerical aperture (NA) objective housed within a microscope body. The NA of an objective describes the ability of the objective to resolve specimens and collect light emitted from the sample.[75] The higher the NA, the larger the collection cone and the tighter the focus inside the sample. Together, pulsed excitation and a high NA objective increase the probability of two photon absorption by a factor of 10^{12}. In addition, because of the near simultaneous absorption requirement in time and space, the only location that possesses a high enough photon density to satisfy this requirement is the focal spot of a converging pulsed laser beam. This then limits the fluorescence emitted from the sample to only the diffraction limited, eliminating the possibility of fluorescence generated outside of the focal volume. Our system uses a mode-locked Titanium:Sapphire (Ti:Sa) oscillator producing femtosecond pulse lengths with an 80 MHz repetition rate. FCS, which will be discussed in further detail later in this chapter, measures fluorescence intensity fluctuations from molecules diffusing through a small volume of light created by a high NA objective in a microscope body. Thus, the instrumentation used for 2PE fluorescence correlates well with the analysis of FCS.

2.2 Diffusion

Diffusion is described as the movement of small molecules due to thermal fluctuations.[76] It is an integral part of many biological and nonbiological functions, such as transport of important nutrients through cell membranes and modeling industrial processes such as corrosion of materials and reactions in complex fluids.[27] Diffusion can be broken down into two categories: translational and rotational. Translational diffusion refers to a molecule's rate of translocation in two-dimensional or three-dimensional space. On the microscopic level, molecules will randomly collide with one another as they move within a medium in a process termed Brownian motion. Typically, while Brownian motion is occurring, molecules will diffuse on a path following a concentration gradient from regions of high to low concentration. This diffusion pathway is labeled as Fickian diffusion, named after Adolf Fick, a German physiologist who is credited as the first to define the laws of mass transport and diffusion in his 1855 report.[77] A representation of Fickian diffusion is shown in **Figure 4**. In other special cases, such as in turbid environments, extreme temperature or viscosity conditions, and/or high concentrations of diffusing species, the diffusion behavior can deviate from normal Fickian diffusion and is labeled as anomalous diffusion. At first glance, the microscopic structural heterogeneity of complex fluid environments would lead us to assume anomalous diffusion is the major driving force in molecular motion. However, because our FCS studies utilize an extremely low concentration of small fluorescent molecules, the details of which are discussed in later chapters, normal Fickian diffusion serves as the basis of our translational diffusions. In support of this, previous FCS work investigating both BμE and GUVs have utilized Fickian diffusion models for fitting FCS correlation curves.[4,59,60,78] The second type of diffusion, rotational diffusion, refers to the rotation

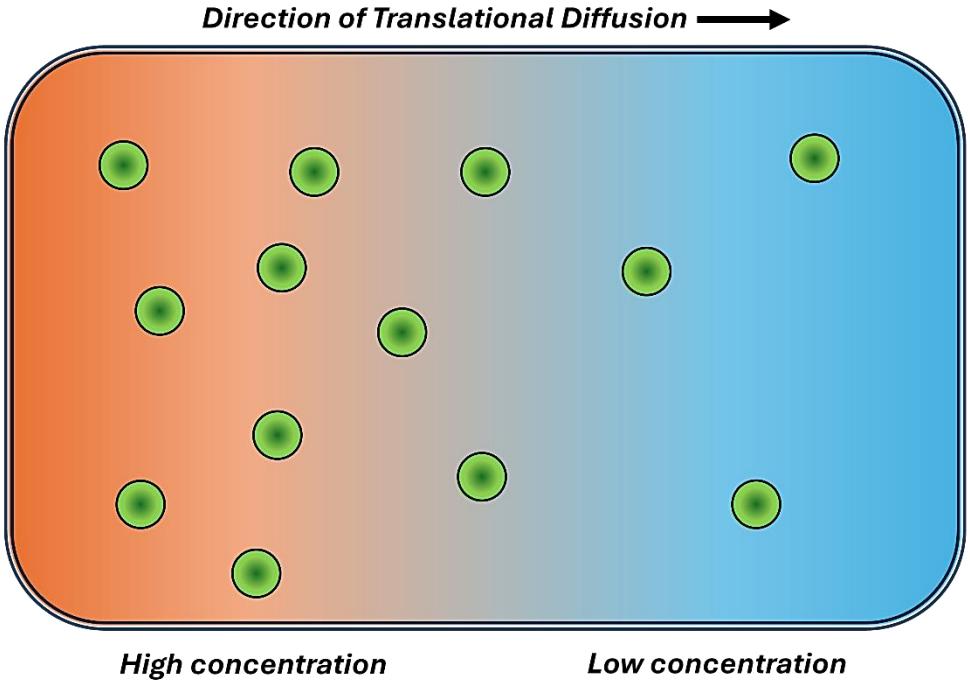


Figure 4. Illustration describing Fickian diffusion. Molecules diffuse from areas of higher concentration to areas of lower concentration when following Fickian diffusion law.

rate of a molecule about an axis. Rotational diffusion is impact by the size and shape of the molecule as well as the viscosity and crowdedness of the surrounding environment.[30] A popular method of measuring rotational diffusion rates a fluorescence-based technique known as a fluorescence anisotropy decay. This technique will bediscussed in further detail in Chapter 3. The scientific questions being asked seek to understand the impact of amphiphile size and structure, probe size and structure, and complex fluid composition on molecular translational and rotational diffusion rates.

2.3 Fluorescence Correlation Spectroscopy

Fluorescence Correlation Spectroscopy (FCS) is a single molecule detection technique that analyzes fluorescence intensity fluctuations that arise from fluorescently active molecules translationally diffusing within a defined volume over time.[32,79] The technique was first developed in 1972 by Magde *et al.* to examine the binding of fluorescent dye EtBr to DNA.[80] However, it was not until the early 1990s when the technique was combined with the components of a confocal microscope that the usage of FCS began to expand.[81] The high NA objective housed in the microscopy body coupled with a laser beam allowed for a significant reduction in the size of the defined focal volume. Since this breakthrough, FCS has become a powerful technique for the determination of translational diffusion coefficients corresponding to excited state reactions within a variety of systems.[80,81]

The most common probe molecules selected for FCS experiments are fluorescent organic dye molecules, or fluorophores, that possess a high quantum yield, extinction coefficient, and photostability. The quantum yield of a molecule is defined as the number of emitted photons relative to the number of absorbed photons,[79] and the extinction coefficient refers to the

probability that a molecule will absorb a photon of a certain wavelength.[82] Furthermore, molecules with a high photostability are much more resistant to photobleaching effects, thereby offering accurate dynamic information without the introduction of unwanted photophysical or photochemical reactions. The maximization of these characteristics is critical to the successful implementation of FCS. Because this technique measures the fluorescence intensity fluctuations over time, an extremely small concentration range from picomolar-nanomolar is required to detect a significant shift in intensity. Thus, the initial amplitude of the autocorrelation function is inversely proportional to the average number of fluorescent molecules within the observation volume of the laser beam. Hence, to maximize the signal-to-noise (S/N) ratio without using excessive incident power amounts, a high quantum yield, extinction coefficient, and photostability are highly sought after in the FCS probe selection process.

2.3.1 Mathematical Basis and Correlation

As mentioned, FCS is a statistical method that measures fluorescence intensity fluctuations due to molecules performing translational diffusion through a confocal volume.[32,79,83] The confocal volume refers to the tightly focused region within a sample generated by a laser beam directed through a high NA objective. Each step in the analysis process is governed by a mathematical function that is used to extract desired information, such as the sample concentration and translational diffusion coefficient. **Figure 5** demonstrates the analysis pathway of a normal FCS experiment. The first image displays a fluorophore translationally diffusing through the confocal volume generated by a high-NA objective. The high-NA objective is essential to FCS to create a volume on the order of 1 femtoliter, which restricts the region of interest and increases the collection cone to improve the sensitivity in fluorescence fluctuations due to diffusing

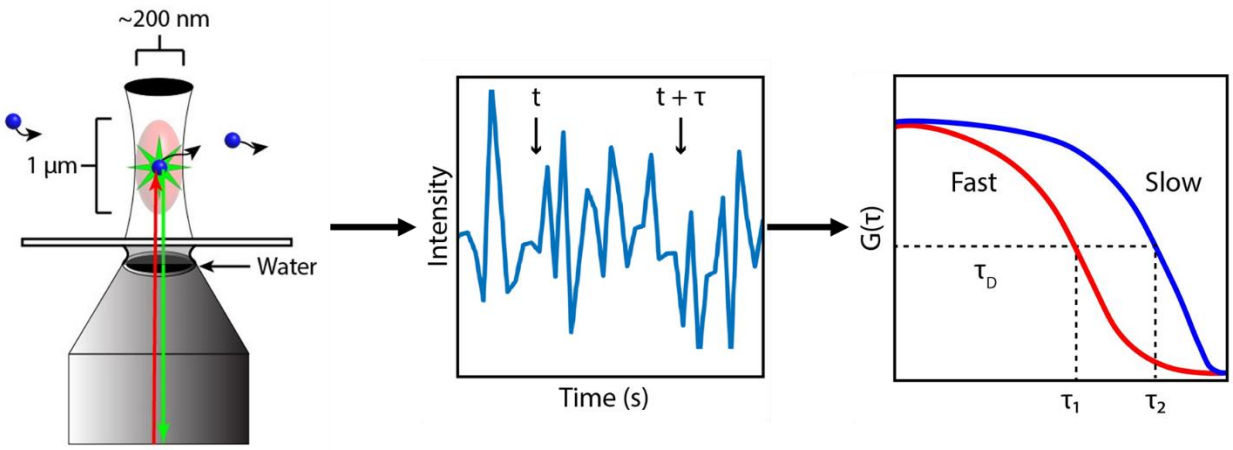


Figure 5. Flow chart depicting the analysis pathway for FCS experiments.

fluorophores.[81,84] Altering the NA of the objective and/or changing the excitation wavelength will result in slightly altered dimensions for the focal volume.

In a 2PE-FCS experiment, the dimensions of the focal volume, or intensity point spread function squared ($IPSF^2$) utilized for FCS analysis are slightly different from the 1PE dimensions (IPSF) due to the quadratic dependency of excitation intensity for 2PE as opposed to the linear dependence of 1PE. As such, measurements of the 2PE-FCS volume dimensions are calculated from the $1/e^2$ intensity value.[79,85] Theoretical calculations for the 1/e intensity lateral and axial dimensions of a 2PE volume utilizing a NA $\geq$ 0.7 are described in Equation 1 and 2, respectively.[86]

$$\omega_{xy} = \frac{0.320\lambda}{\sqrt{2}NA} \quad (1)$$

$$\omega_z = \frac{0.532\lambda}{\sqrt{2}}\left[\frac{1}{n - \sqrt{n^2 - NA^2}}\right] \quad (2)$$

Where λ is the excitation wavelength, *NA* is the objective numerical aperture, and *n* is the refractive index of the immersion liquid. Conversion to the $1/e^2$ dimensions is achieved by multiplying the

1/e value by $\sqrt{2}$. Our instrument operates an ultrafast, mode-locked laser beam centered at 800 nm directed through a 1.2 NA water-immersion objective. With these values and a water refractive index value of 1.333, the $1/e^2$ theoretical lateral, *s*, and axial, *u*, radius of the $IPSF^2$ is 0.220 μm and 0.566 μm, respectively. The testing of the experimental $1/e^2$ dimensions will be performed through instrument calibration later in this chapter.

When the FCS measurement is initiated, the fluorescence intensity fluctuations are monitored over the duration of the experiment, as depicted by the second image of **Figure 5**.

These fluctuations are tracked as a measure of the difference in intensity from the average value over the course of the experiment. Throughout the measurement, fluorescence intensity readings at a starting point *t* and varying time points after the start time, or lag times τ, are correlated using a simple autocorrelation function, *G'(τ)*, denoted by Equation 3 and the third image in **Figure 5**.

Essentially, the fluorescence intensity at different time points is being compared to the intensity at the initial time point for similarity. The more similar they are, the higher the amplitude of the correlation curve. For examining translational diffusion, a three-dimensional (3D) normal diffusion model assuming a Gaussian excitation profile fits over the data, which is described in Equation 4.

$$G(\tau) = \frac{1}{N}\left(1 + \frac{\tau}{\tau_D}\right)^{-1}\left(1 + \frac{\tau}{\tau_D} * \frac{s^2}{u^2}\right)^{-1/2} \quad (4)$$

$$G'(\tau) = \frac{\langle F(t)F(t+\tau)\rangle}{\langle F\rangle^2} \quad (3)$$

where *G(τ)* is the autocorrelation function amplitude, *N* is the number of molecules in the observation, *τ* is the lag time, τ_D is the diffusion time of the molecule through the observation volume, and *s* and *u* represent the $1/e^2$ lateral and axial waists of the observation volume, respectively. *G(τ)* deviates from *G'(τ)* in that *G(τ)* represents the autocorrelation function in terms of translational diffusion, while *G'(τ)* denotes the autocorrelation function in terms of fluorescence intensity. For complex fluids, despite the presence of only one active fluorophore diffusing in the solution, trace amounts of fluorescence intensity from other sources could contribute slightly to the overall correlation curve.[64,87] To account for this a simple modification was applied to Equation 4 to produce a two-component 3D diffusion model, as shown in Equation 5.

$$G(\tau) = \frac{1}{N}[F_1\left(1+\frac{\tau}{\tau_{D1}}\right)^{-1}\left(1+\frac{\tau}{\tau_{D1}}*\frac{s^2}{u^2}\right)^{-\frac{1}{2}} + (1-F_1)\left(1+\frac{\tau}{\tau_{D2}}\right)^{-1}(1+\frac{\tau}{\tau_{D2}}*\frac{s^2}{u^2})^{-1/2}] \quad (5)$$

As stated previously, the amplitude of the correlation function at time zero, *G(0)*, is inversely proportional to the average number of fluorophores in the observation volume, shown in Equation 6. From **Figure 5**, the time taken for the amplitude of the correlation curve to reach its half-maximum value corresponds to τ_D. Longer diffusion times are represented by a correlation curve

$$G(0) \sim \frac{1}{\langle N \rangle} \quad (6)$$

pushed to higher orders of magnitude on the lag time axis (blue curve), while shorter diffusion times display a curve that begins to fall at lower orders of magnitude (red curve). Combining the extracted τ_D with the lateral beam waist *s*, the determination of a diffusion coefficient using 2PE-FCS is done using Equation 7.

$$D = \frac{s^2}{8\tau_D} \quad (7)$$

It is worth noting that in the denominator of Equation 5, the constant 8 differs from the 1PE constant of 4, and this difference is attributed to the squared intensity dependence of 2PE compared to the linear intensity dependence of 1PE.[79,88]

2.4 Constructed Instrument

A schematic of the home-built FCS instrument is shown in **Figure 6**. Our setup utilizes an ultrafast Ti:sapphire laser that is centered at 800 nm with a repetition rate of 80 MHz. The emitted beam first travels through a λ/2 waveplate and a polarizing beam splitting cube (PBC),

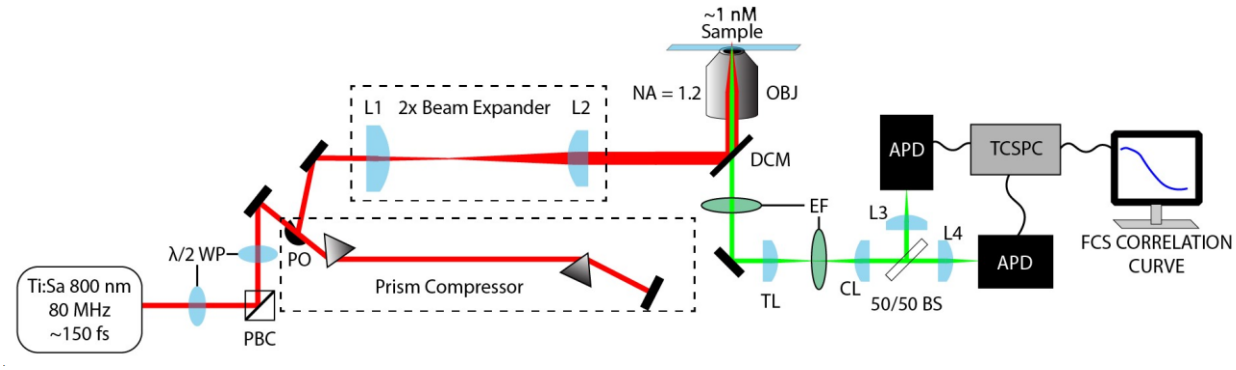


Figure 6. Schematic of the TPE-FCS instrument. λ/2 WP = one half waveplate. PBC = polarizing beam splitting cube. PO = pickoff mirror. L1 = first telescope lens. L2 = second telescope lens. DCM = dichroic mirror. NA = numerical aperture. OBJ = objective. nM = nanomolar concentration. EF = emission filters. TL = tube lens. CL= collimating lens. L3, L4 = focusing lenses. APD = avalanche photodiodes. TCSPC = time correlated single photon counting module.

which together serve as a power attenuator for the instrument. The λ/2 waveplate rotates the linear polarization of the beam striking the PBC, and depending on the angle of polarization, a certain percentage of light will be reflected off the cube or transmitted through, allowing the intensity of the beam to be controlled. In nonlinear spectroscopy, a shorter pulse length on the order of femtoseconds is desired to increase the peak power, which is essential for successful and accurate TPE-FCS measurements. Due to the nature of ultrafast laser operation, the femtosecond pulses of light possess a large spectral bandwidth. Because of this, the different wavelengths within this bandwidth will pass through materials and air differently as the beam traverses the optical table, with longer wavelength light traveling faster than shorter wavelength light. The result is a lengthening of the pulse width, or a process called positive group delay dispersion (GDD), and it must be controlled to fully take advantage of ultrafast pulsed laser sources for nonlinear spectroscopy[89]. To counteract positive GDD, the beam is sent through a linear prism compression line that introduces negative GDD.

Our pulse length has been measured to ~150 fs at the sample position, which is acceptable for our experiments. After the compression line, the beam is expanded with a telescope comprised of two plano convex lenses with focal lengths of 150 mm and 75 mm. This expands the beam diameter to ~20 mm to overfill the 10 mm back aperture of the microscope objective to achieve the smallest diffraction limited spot. The beam is directed into the back aperture of the objective by a 650 nm shortpass rectangular dichroic mirror housed within a filter cube. The 1.2 NA water-immersion objective focuses the beam to ~1 fl sized volume within the sample ≥ 50 μm away from the coverslip-sample interface. The emitted fluorescence from diffusing fluorophores is collected by the objective and filtered by the dichroic mirror and two bandpass filters to reject

any incident 800 nm light. The fluorescence is split by a 50/50 beamsplitter before being focused onto the 100 μm diameter active areas of two avalanche photodiodes (APDs), which are operating in single photon counting mode. The photon counts are cross-correlated by a time correlated single photon counting module (TCSPC) operating in Time Tagged-Time Resolved (TTTR) mode. TTTR mode records the timing of events with respect to the beginning of the measurement, making it ideal for FCS data collection. Furthermore, APDs have a low chance of producing a second electronic pulse when a single photon strikes the detector. This second pulse is highly correlated with the first, and thus a large spike in the amplitude of the correlation is witnessed at lag times lower than 1 μs.[90] To counteract this occurrence, a cross-correlation scheme is implemented to eliminate the effects of afterpulsing present in autocorrelation detection schemes. Although the translational diffusion information desired from fluorophore diffusion in complex liquids is on a timescale much longer than the time region of afterpulsing effects, the cross-correlation curve provides a more accurate reading of initial cross-correlation curve amplitude, thereby assisting in diffusion model fitting. The raw correlation curve data is migrated to a custom MATLAB script which contains all the equations for correlation and data extraction described in the previous section.

2.4.1 Calibration

To complete the construction of the FCS instrument, the focal volume created by the laser beam and the objective must be precisely determined to ensure confident results and diffusion coefficient analysis. One of the most common processes for calibration is to obtain a correlation curve generated from a molecule with a known diffusion coefficient in a certain solvent. For this purpose, an aqueous solution of 1 nM Alexa 546 NHS ester was chosen due to this molecule's

high two-photon absorption coefficient at 800 nm.[91] A figure of Alexa 546 NHS ester is shown in **Figure 7**. This molecule has a reported diffusion coefficient in water of 341 $\mu m^2/s$.[92] A representative calibration curve from this sample is displayed in **Figure 8**. By fitting the curve with the 3D normal diffusion model and locking the diffusion coefficient value, a characteristic diffusion time, τ_D, of the probe through the focal volume is extracted, and by utilizing the relationship of parameters discussed in Equation 8, the lateral waist radius *s* can be obtained. For statistical analysis, three measurements of $\geq$ 15 minutes measurement time were performed, and the standard deviation and error were determined. From the three measurements, a focal volume with a $1/e^2$ radius of 530.4 ± 17.4 nm was calculated. While the experimental lateral radius is ~2.4 times larger than the theoretical lateral radius, a report using a similar setup for TPE-FCS produced a similarly sized beam waist.[93] Furthermore, the calibration measurements were very reproducible with minimal error at power levels between 40-60 mW measured directly outside the microscope body. Therefore, complex fluid measurements were taken as close to these conditions as possible for each FCS experiment.

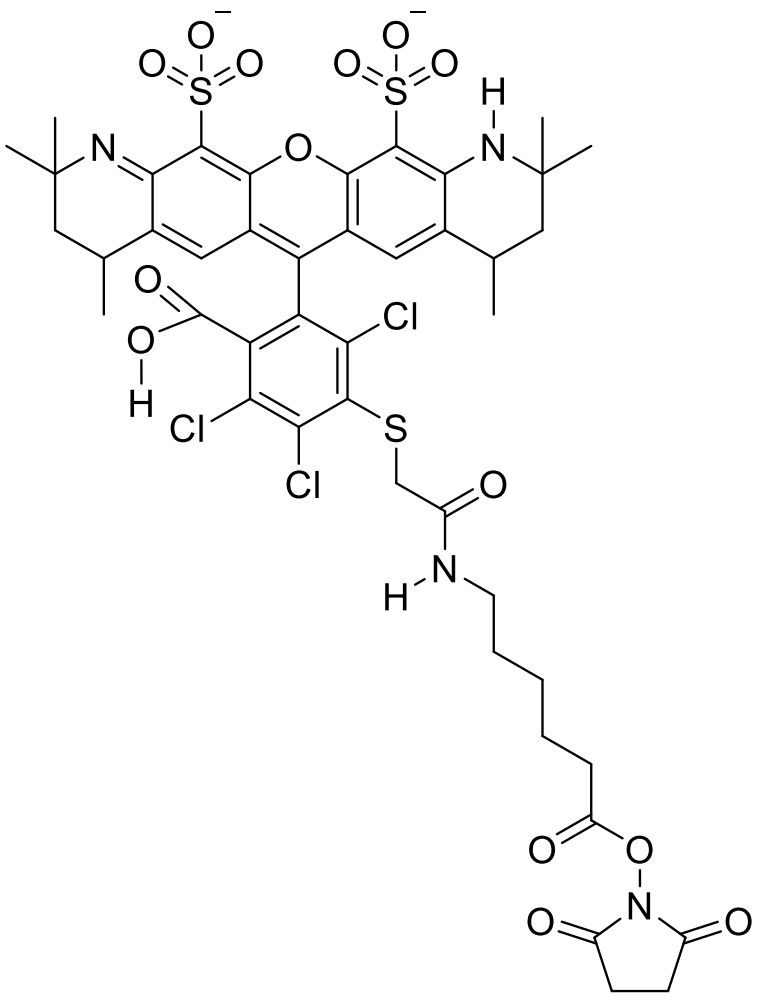


Figure 7. Structure of Alexa 546 NHS ester.

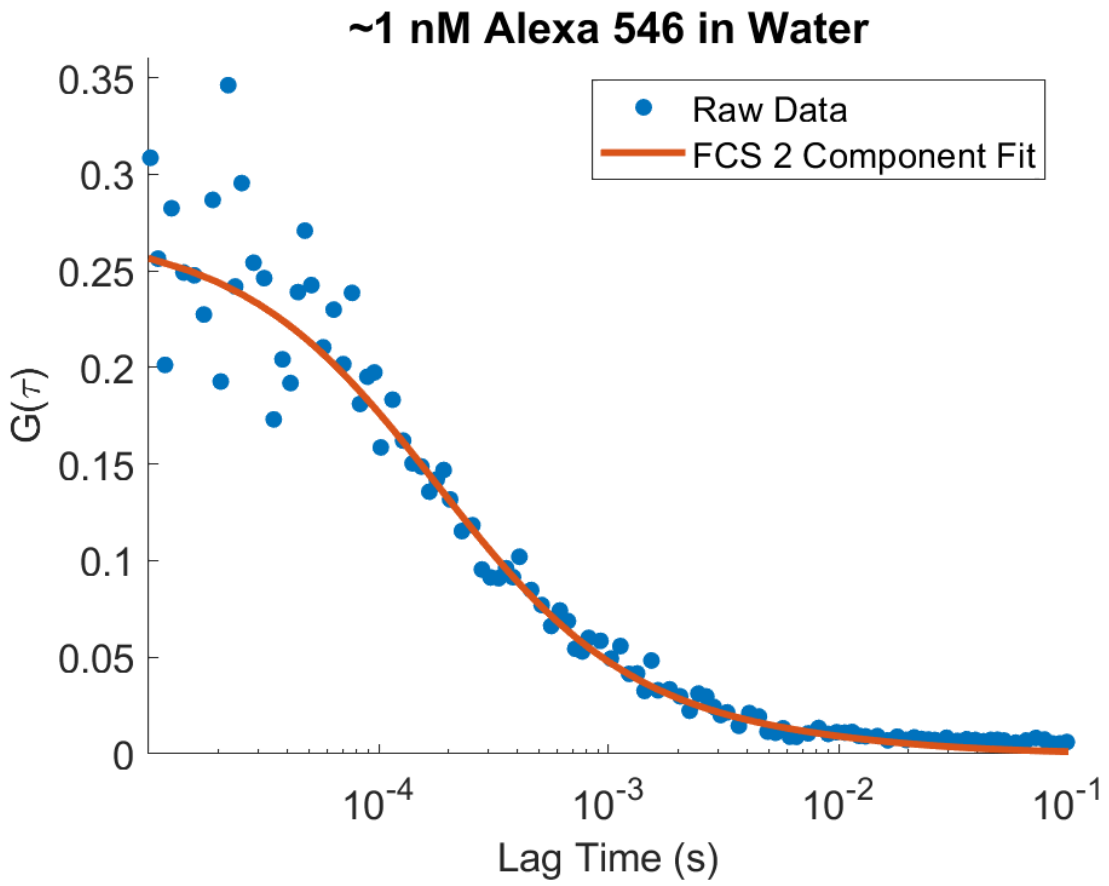


Figure 8. Representative calibration FCS curve of Alexa 546 NHS ester in MilliQ water.

CHAPTER THREE

BICONTINUOUS MICROEMULSION STUDIES

3.1 Motivation

As mentioned previously, BμE are thermodynamically stable, optically clear solutions of oil, water, and surfactants. From the earliest days to more recent studies, the characterization and phase equilibrium of the bicontinuous structure has been the primary focus of research towards development of new products.[38,94–98] Through these works, it has been accepted that the general structure of a bicontinuous microemulsion is a series of disordered water and oil channels that are separated by the surfactant layer, and the self-diffusion of the water and oil channels away from the surfactant monolayer should remain unrestricted.[95] Their low interfacial tension, low viscosity, and ability to solubilize species in both water and oil phases has seen their incorporation in several fields in both biology and industry.[4,5,16,42–45] One particular aspect of the applications of BμEs is the ability for small molecules to diffuse at the interface between bulk microemulsion phases. In some situations, a faster diffusion of active materials in BμEs is desired, such as for performing facile electron transfer in electrochemistry[14] or immediate treatment of illnesses in drug delivery.[99,100] In other instances, a slower diffusion of molecules is preferable, such as the controlled release of substances over longer periods of time for drug delivery.[101,102] Therefore, examining the factors that influence these diffusion capabilities is essential towards new product development. In our lab, work by Hassan *et al.* examined the rotational diffusion dynamics of a small nonpolar, polar, and ionic fluorophore in both droplet and bicontinuous microemulsions containing the nonionic surfactant Tween 20, water, 1-butanol, and toluene.[103] The objective was to understand the rotational freedom of these small molecules

in microemulsions and determine where the molecules tended to reside. The results from this work revealed that all probes interacted with the surfactant region of the microemulsions, with the degree of surfactant layer penetration postulated from the partitioning coefficient values and Forster Resonance Energy Transfer (FRET) results. In particular, the ionic and polar molecules demonstrated the largest rotational freedom in the bicontinuous phase of the microemulsion, indicating the enhanced fluidity of the surfactant layer in this composition. Still, two of the main questions that arose from this study asked how the Tween 20 molecule itself, specifically the large, bulky head group, was impacting the freedom of the diffusing species, and what is the translational diffusion behavior in this and other BμEs. Tween 20 possesses a large, three-pronged head group with approximately five polyethylene oxide (PEO) repeating units on each arm connected to a $C_{11}H_{23}$ hydrocarbon tail. This bulky hydrophilic head group compared to the smaller hydrocarbon tail was suspected to heavily influence the diffusion rates of the fluorophores in the microemulsions tested. As mentioned before, the HLB and CPP are two popular metrics for the determination of where the surfactant will lie and what nanostructures will be formed from an aggregation of surfactants.[33–35] Tween 20 has a HLB value of 16.7,[104] indicating much more solubility in the aqueous phase of the microemulsion compared to the nonaqueous phase, thus creating a more fluid interface. While a specific CPP is not reported for Tween 20, the large, bulky head group in comparison to the small hydrocarbon tail is suspected to decrease the packing parameter, leading to a tendency to form more cylindrical or worm-like channels.[105] In addition, while there have been a few published studies examining translational diffusion in BμE with FCS,[53,78,87,106,107] these studies have focused on the translational diffusion of nonaqueous probes in ionic surfactant systems and diffusion of aqueous probes in smaller,

nonionic surfactant systems. Therefore, the translational diffusion of aqueous probes in both ionic and medium sized, nonionic surfactant systems has yet to be explored. The HLB was designed to primarily characterize nonionic surfactants,[108] and the larger size of the PEO headgroup will typically lead to a more hydrophobically soluble interface, which could lead to more restricted hydrophilic head group. Furthermore, surfactants with higher CPP values tend to form less restricted microstructures.[105] As such, examining the impact on diffusion from surfactants with different HLB and CPP values would be beneficial. To examine this, a series of FCS and steady state fluorescence anisotropy measurements were conducted to examine the translational and rotational diffusion of two differently sized hydrophilic dyes, Alexa 546 NHS ester and Rhodamine 6G, in BμEs containing the surfactants sodium dodecyl sulfate (SDS), cetyltrimethylammonium bromide (CTAB), Brij O10, and Triton X-100. To provide further support, microviscosity measurements and generalized polarization measurements of Laurdan were performed to offer insight into the microenvironment of the diffusing fluorophores.

3.2 Sample Preparation

Four different surfactants were used in preparation of the BμEs: SDS, CTAB, Brij O10, and Triton X-100. CTAB and Brij O10 were purchased from Sigma-Aldrich, while SDS and Triton X-100 were purchased from Fischer Scientific. The cosurfactant 1-butanol, the fluorophores Alexa 546 NHS Este, Rhodamine 6G, Laurdan, and the oil phase cyclohexane were purchased from Fischer Scientific. The oil phase isopropyl palmitate and the fluorophore 1,6-Diphenyl-1,3,5-hexatriene (DPH) were purchased from Sigma-Aldrich. All surfactants, solvents, and probe molecules were used as received. MilliQ water was used as the aqueous phase of each microemulsion. Formulation of each BμE followed procedures outlined in the literature. For the

SDS BμE, the component weight percentages were 52% MilliQ water, 26.7% 1-butanol, 13.3% cyclohexane, and 8% SDS (SBWC).[109] The CTAB BμE contained 35% MilliQ water, 35% 1-butanol, 12.5% cyclohexane, and 17.5% CTAB (CBWC),[109] while the Triton X-100 system contained 60% MilliQ water, 30% 1-butanol:Triton X-100 surfactant mix at a 0.25:0.75 ratio, and 10% cyclohexane (TxBWC).[110] Finally, we examined two different Brij O10 compositions that form BμEs. The first contained 25% MilliQ water, 40% Brij O10:1-butanol mix at a ratio of 1.5:1, and 35% isopropyl palmitate (IPP), and the second contained 50% water, 40% surfactant mix, and 10% IPP (BWBI).[111] The fluorescent probes Alexa 546 NHS Ester and Rhodamine 6G were chosen for FCS and steady state anisotropy measurements due to their high photostability, quantum yield, and two photon cross section at 800 nm excitation.[91] These fluorophores were initially dissolved in MilliQ water to stock solutions of approximately 10 μM and 1 mM, respectively. The stock solutions were serially diluted to a final concentration ranging between 1-5 nM for FCS experiments. The stock fluorophore solutions were weighed to the desired amount for each BμE in a 10 mL falcon tube, followed by the required amounts of surfactant, oil phase, and cosurfactant. Once all components were added, the tube was capped and vortexed for 30 seconds and left to settle for 1 hour. Finally, 1 mL of BμE solution was pipetted into a glass chamber with a 1.5 cover glass bottom on a translational xyz stage for analysis.

Solutions for steady state anisotropy measurements of DPH were prepared in the same fashion by dissolving DPH in the surfactant mix and mixing the microemulsion components to make solutions with a final DPH concentration of 10 μM. The microemulsions were placed directly in cuvettes in a Horiba FluoroLog 3. Excitation was set to 353 nm and emission was set to 425 nm. Steady state fluorescence measurements of Laurdan for generalized polarization were

performed at room temperature on an Agilent fluorescence spectrophotometer. Laurdan was dissolved in 1-butanol and diluted to a final concentration of 5 µM in each microemulsion. All experiments were performed at room temperature.

3.3 FCS Results

3.3.1 FCS Results in Nonionic Surfactant Bicontinuous Microemulsions

In the beginning, the 60% water Tween 20 BµE from Hassan *et al.*'s[103] work was tested using the constructed FCS instrument described in Chapter 2. During testing, regardless of the small molecule placed in the microemulsion, there was too much background signal from the microemulsion itself to obtain any definable FCS curve. This was attributed to the large difference in fluorophore concentration between Hassan *et al.*'s work and the FCS experiments performed here. The nanomolar concentration of fluorophores required for FCS were unable to overcome the background signal, which was not an issue for Hassan *et al.* as they used concentrations in the micromolar range. Therefore, the diffusion behavior of Alexa 546 and Rhodamine 6G was examined in two new BµEs that contained the nonionic surfactants Brij O10 and Triton X-100. The structures of both surfactants, as well as Tween 20, are shown in **Figure 9**. **Figure 10** displays the fluorophore structures. Brij O10 has an 18-carbon hydrocarbon chain with a large polyethylene oxide (PEO) headgroup with approximately 10 repeating units. Triton X-100 has the same head group as Brij O10 with a smaller, aromatic tail. Compared to Tween 20, these two surfactants possess straight chained head groups as opposed to Tween 20's large, three-pronged branching head group. Furthermore, these surfactants have documented microemulsion phase diagrams in the literature, [110,111] and Triton X-100 is the most studied nonionic surfactant in the literature.[110,112–116] Also, the differing tail regions between Triton X-

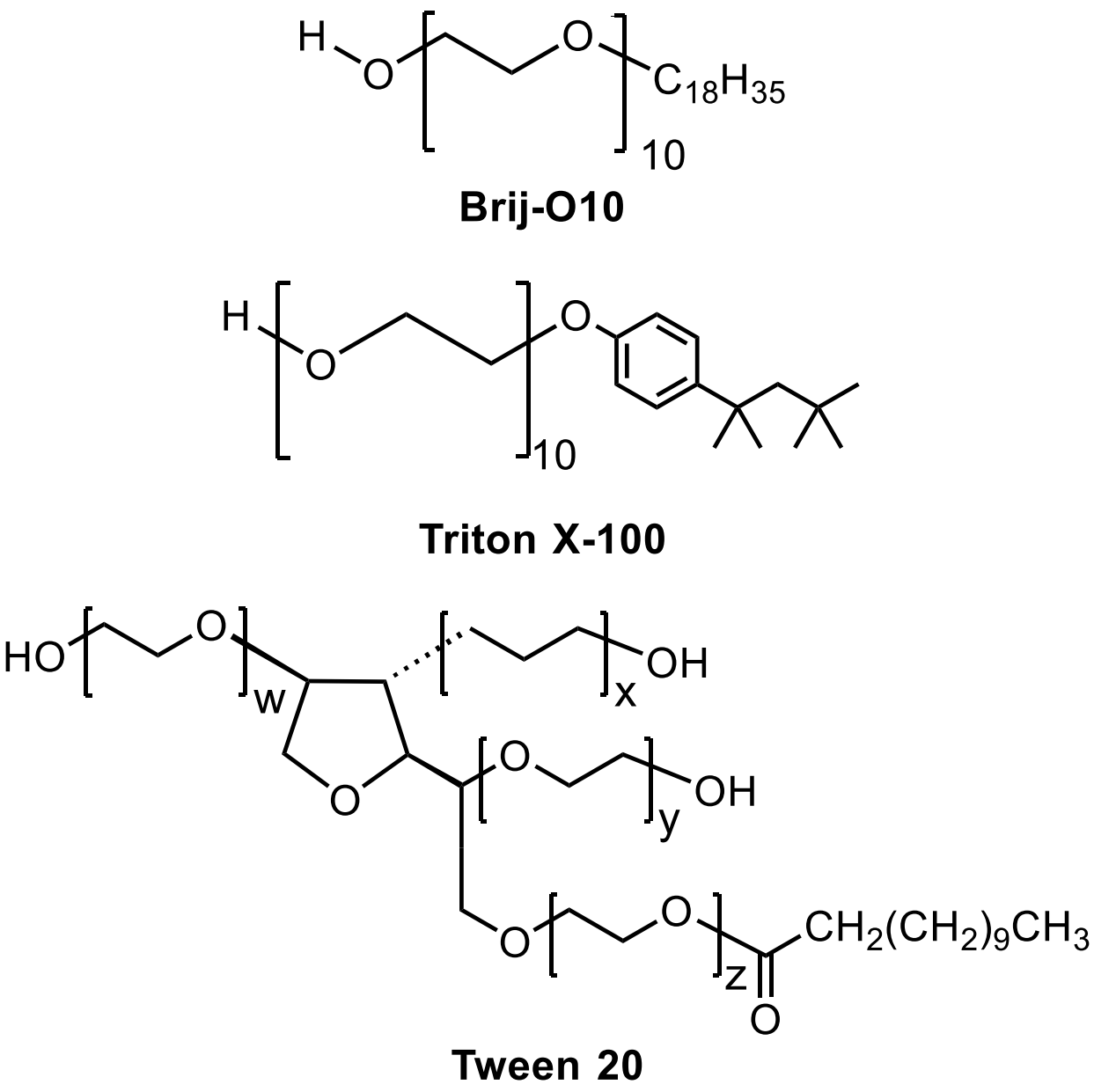


Figure 9. Nonionic surfactant structures. Brij O10 and Triton X-100 possess a large PEO chain head group, which is suspected to penetrate deep into the aqueous layer of the microemulsion.

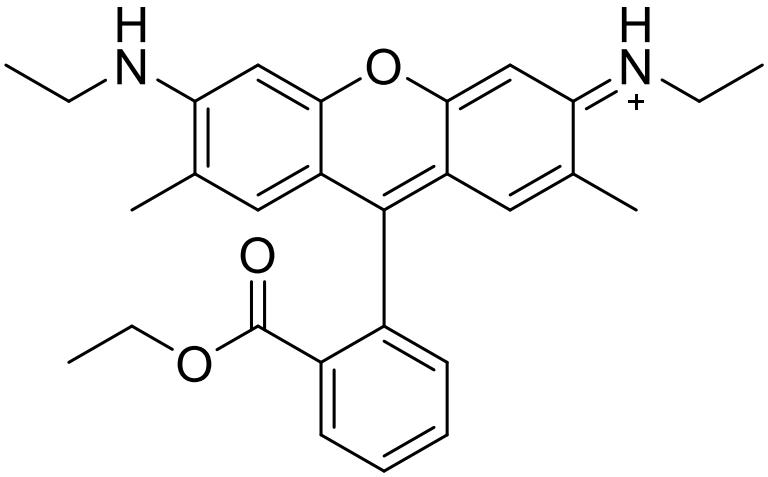


Figure 10: Molecular structures of Rhodamine 6G (Top) and Alexa 546 NHS ester (bottom).

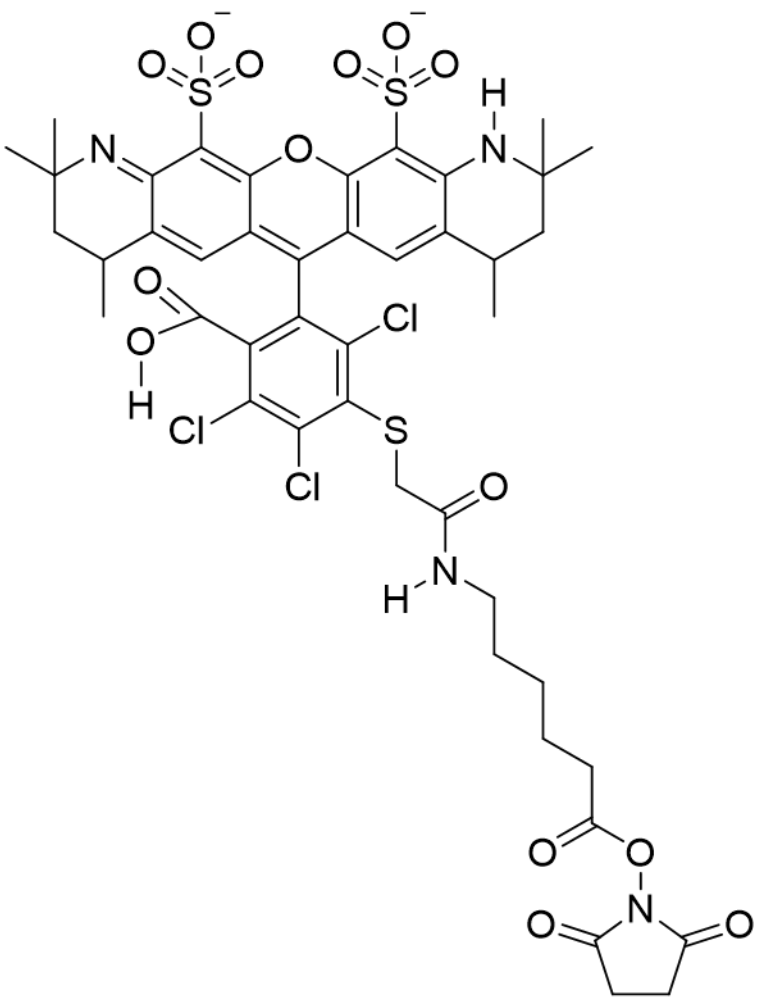


Figure 10: Continued

100 and Brij O10 which can provide an additional point of comparison in our results and discussion. Firstly, representative FCS correlation curves of Rhodamine 6G and Alexa 546 in a 25% water BWBI BμE are shown in **Figure 11**. Rhodamine 6G was calculated to have a diffusion coefficient of 28.14 ± 4.15 $\mu m^2/s$ and Alexa 546's diffusion coefficient was calculated to be 14.77 ± 0.73 $\mu m^2/s$. These diffusion coefficients can also be found in the bar graph in **Figure 12**. Rhodamine 6G possesses the same core structure as Alexa 546, but the former is smaller than the latter with a hydrodynamic radius of 0.527 nm compared to 0.635 nm for Alexa 546. In addition, the molecular weight of Rhodamine 6G is 479.02 g/mol, while the molecular weight for Alexa 546 is 1159.6 g/mol. Typically, in diffusion experiments, the lighter weight molecule will diffuse faster than the heavier molecule, and this behavior is also witnessed here. What is more eye-catching is the significant decrease in diffusion speed compared to these molecules reported diffusion rates in water alone (341 $\mu m^2/s$ for Alexa 546 and 420 $\mu m^2/s$ for Rhodamine 6G).[92,117] In BμEs, the water and oil are said to have unrestricted diffusion in their respective channels,[95,118] and the diffusion coefficients calculated here signify that both molecules are interacting with the surfactant head group. However, one of the characteristics of this microemulsion composition lies in the much smaller percentage of water (25%) compared to the surfactant mix (40%) and IPP (35%). Since Alexa 546 is soluble in water, this probe can help to understand if the amount of water in the BμE is impacting the diffusion coefficient results. Thus, an FCS experiment was performed on a second BWBI BμE that contained 50% water, 40% surfactant mix, and 10% IPP. The representative FCS curve of Alexa 546 in the 50% water BWBI BμE is shown in **Figure 13**, and the diffusion coefficient is found to be 19.0901 $\mu m^2/s$. This result is slightly faster than the result of the diffusion coefficient of Alexa 546 in the 25%

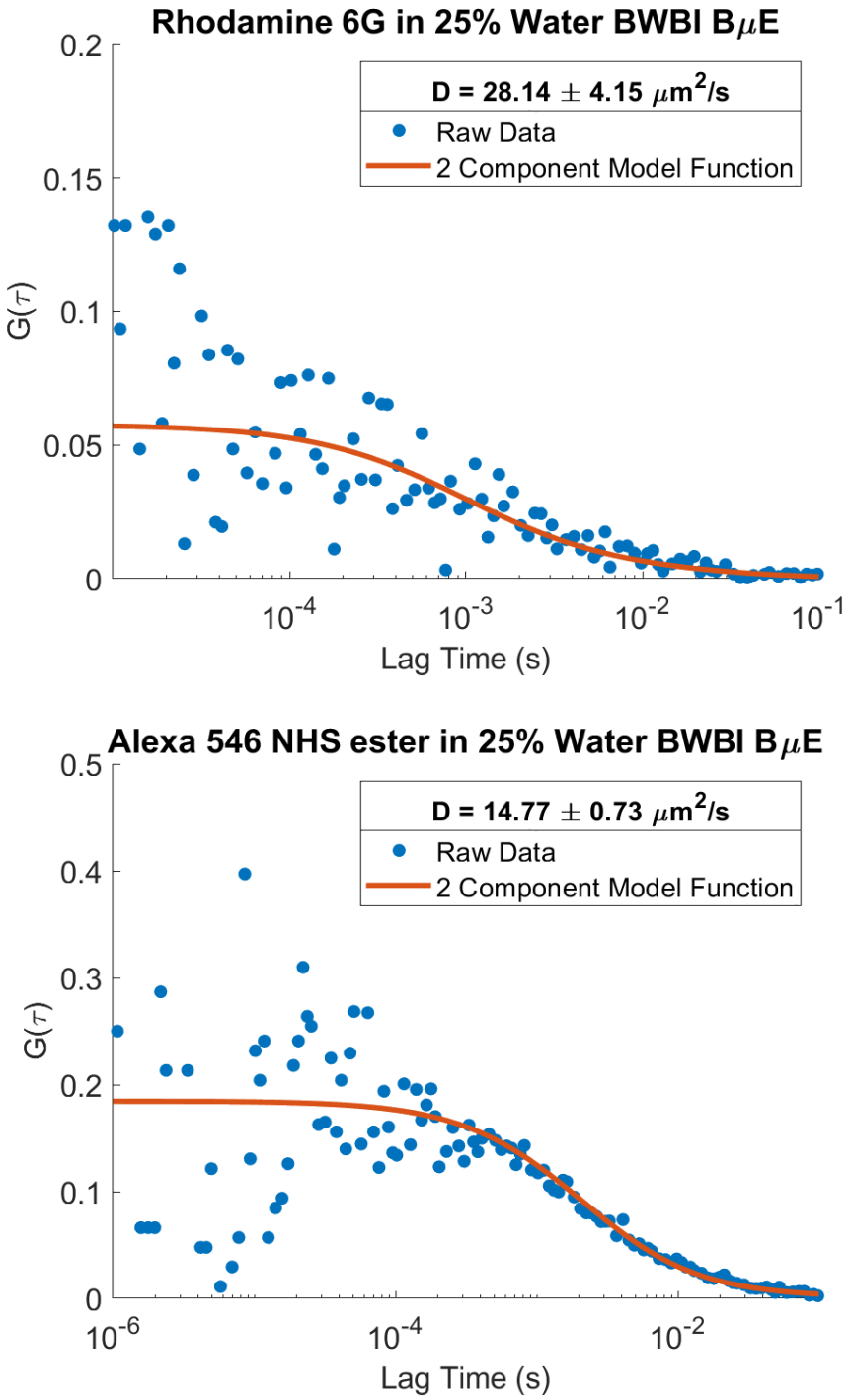


Figure 11. Representative FCS Curves of Rhodamine 6G (Top) and Alexa 546 NHS ester (bottom) in a 25% water BWBI BE.

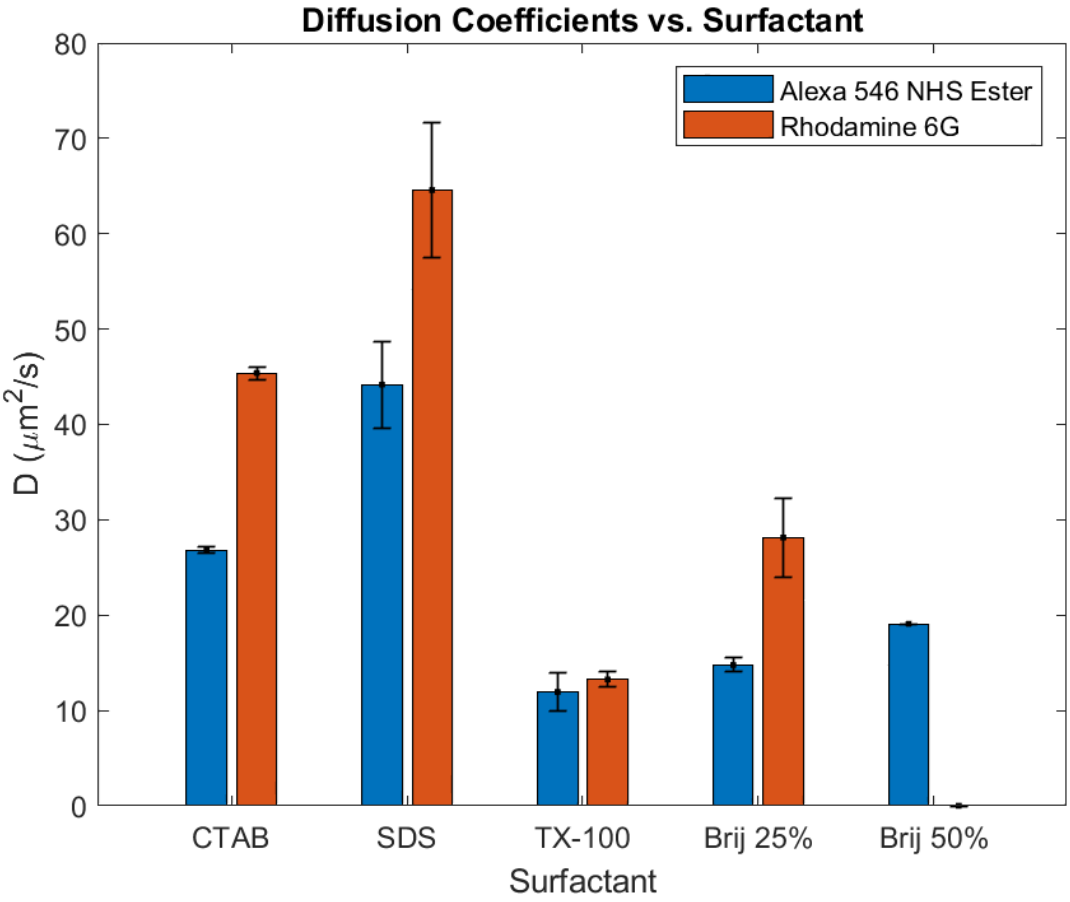


Figure 12. Diffusion coefficients of each probe in all bicontinuous microemulsions. Surfactants with a larger head group restrict the translational diffusion of fluorophores more than smaller head group surfactants.

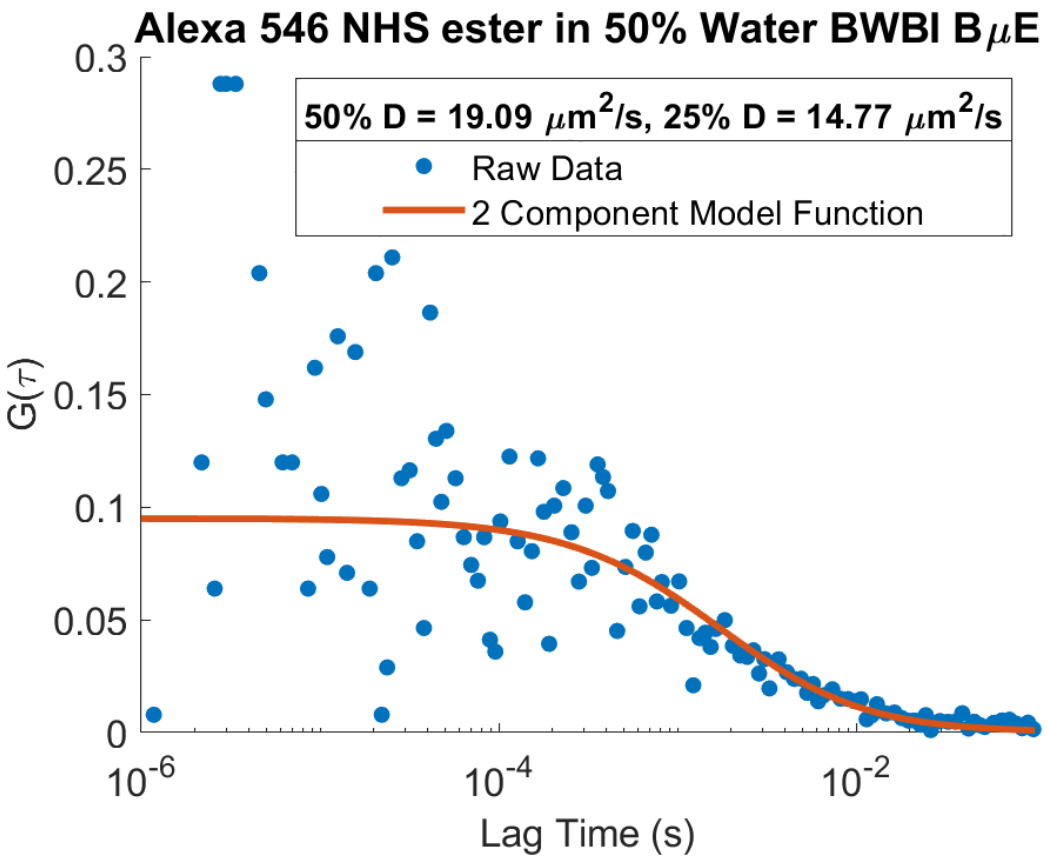


Figure 13. Representative curve of Alexa 546 in a BWBI BμE with 50% water. The diffusion coefficient obtained here is slightly larger than the diffusion coefficient in a 25% water BWBI BμE shown in **Figure 11**.

water solution, which indicates that more water could be penetrating the interface and creating a more fluid diffusing region. Laurdan measurements investigating this effect will be examined later in this chapter. However, in a previous FCS study on a nonionic surfactant BμE, the diffusion of molecules within a major domain will only be hindered by the domain itself if the size of the domain shrinks to or below the size of the diffusing molecule.[78] The molecules tested here have a sub 1 nm radii, and based on domain size characterization of this BWBI system,[111] none of the compositions tested reached a domain size close to this, leading us to conclude that the size of the water channel is not altering the diffusion behavior. As such, the measured diffusion coefficients are attributed to interactions of the fluorophores with the surfactant head groups.

As a comparison to the translational diffusion results obtained in the BWBI BμEs, it has been suggested that the structure of the tail region in nonionic surfactants can impact the packing of the surfactants and the fluidity of the created nanostructures.[105,119] These tail structure alterations are also suspected to impact the alignment of the surfactants at the interface, which could induce changes to the diffusion behavior. To examine this, another nonionic surfactant BμE containing Triton X-100 was formed. Triton X-100 possesses the same 10 repeating units of the PEO hydrophilic head group, but its tail structure is much bulkier than the long, linear hydrocarbon tail of Brij O10. Representative FCS correlation curves of Alexa 546 and Rhodamine 6G in this system are shown in **Figure 14**. The calculated diffusion coefficient for Rhodamine 6G is 13.25 ± 0.79 $\mu m^2/s$ and for Alexa 546 is 11.94 ± 2.00 $\mu m^2/s$, and these values are also displayed in **Figure 12**. To begin, the trend of the lighter Rhodamine 6G moving faster than the heavier Alexa 546 is once again seen here, though the extent of this difference is much

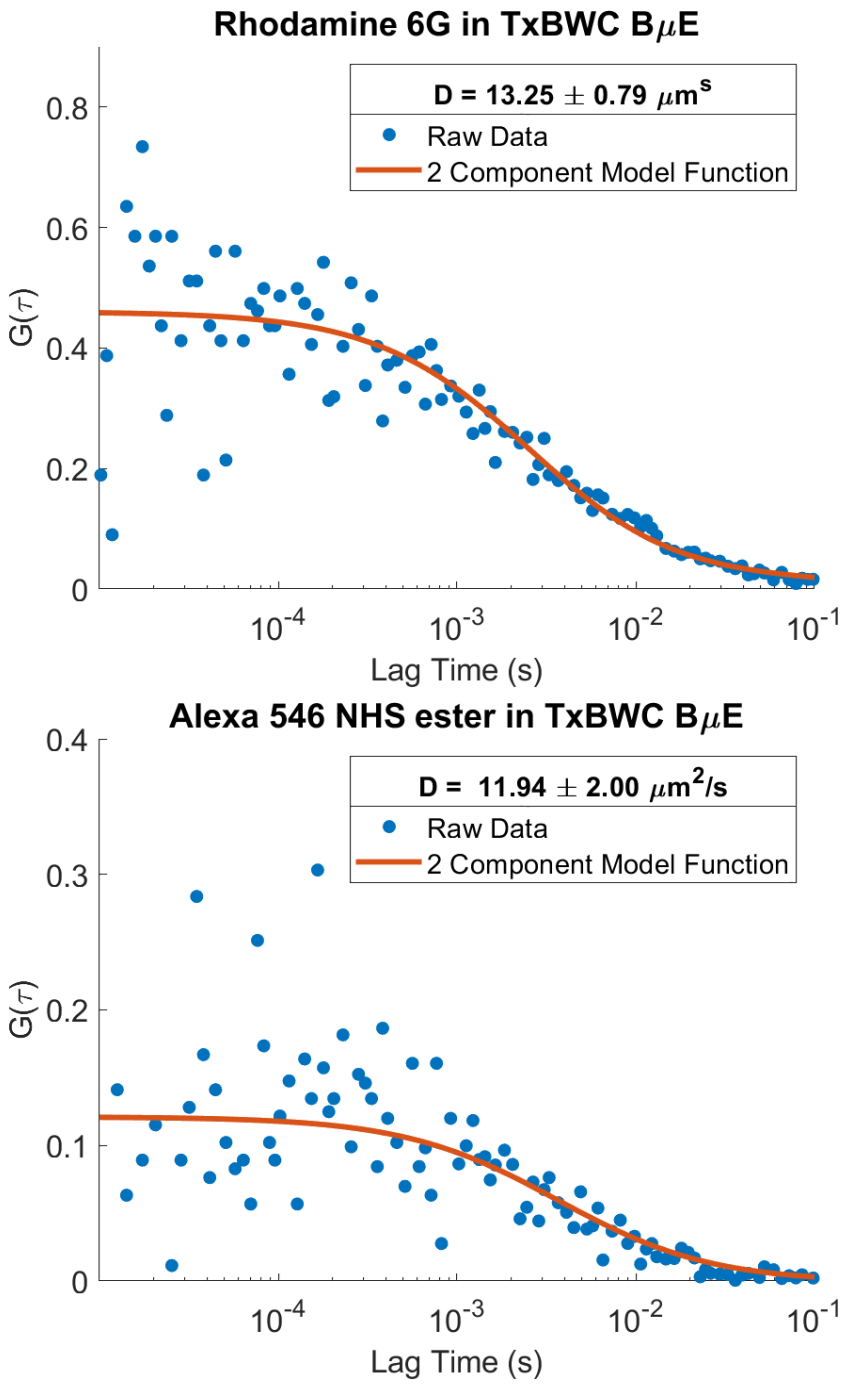


Figure 14. Representative FCS curves of Rhodamine 6G (top) and Alexa 546 NHS (bottom) in a TxBWC BE.

more subdued compared to the results in the BWBI experiments. More apparent is the further decrease in diffusion rate of the fluorophores in the TxBWC system. Specific work on Triton X-100 BμEs and complex systems has stated that a network of continuous water channels in an oil continuous solution comprisesthe bicontinuous structure.[120,121,110] This again indicates that if the fluorophores were diffusing through the middle of the aqueous channel, they would be producing much higher diffusion coefficients. This supports the notion that the microenvironment of the diffusing species includes the surfactant interface. A study published by Frank *et al.* investigated the impact of tail structure for nonionic alcohol ethoxylates on the fluidity of the interfacial film.[119] Their results indicated that a bulkier tail group would lead to a higher curvature of the interface towards the water domain and less perfect alignment of the interface. Based on these conclusions, as the fluorophores are diffusing near the surfactant head groups, they could be experiencing various pathways around the surfactant heads due to the bulker tail region of Triton X-100 compared to Brij O10. Also, Triton X-100 has a HLB value of 13.5, which is slightly more hydrophilic than Brij O10, potentially allowing for more water penetration and further trapping of the fluorophores. Later studies examining the water penetration of the interface and the rotational dynamics of a fluorophore in this region hope to tease apart the underlying causes of the translational diffusion behavior.

The results of these initial FCS experiments have revealed that the structures of the surfactant used in the formation of a BμE will heavily impact the translational diffusion behavior of small molecules within these complex fluids. While the size of the diffusing molecule dissolved in the aqueous phase does impact diffusion rate, the impact of the extension of the surfactant head into the aqueous phase and the allowed water penetration into this layer still

requires more evidence before a conclusion can be drawn. Furthermore, the structure of the tail region of nonionic surfactants could further decrease fluorophore translational diffusion rates. To probe the impact of surfactant structure on translational diffusion further, we shifted focus to examine ionic surfactants with much smaller hydrophilic head groups.

3.3.2 FCS Results in Ionic Surfactant Bicontinuous Microemulsions

Continuing the efforts of examining the impact of surfactant structure on aqueous probe molecule translational diffusion, BμEs containing the cationic surfactant CTAB and the anionic surfactant SDS were formed. Cationic and anionic surfactants have seen tremendous use in household cleaning products, pharmaceutical formulations, road surface coatings, flow battery solutions, etc., with new applications in drug delivery and electrochemistry being investigated.[53–55] The two selected surfactants are shown in **Figure 15**. CTAB possesses a small, positively charged quaternary ammonium head group followed by a 16-carbon hydrocarbon tail. On the other hand, SDS contains a negatively charged sulfate head group connected to a 12-carbon hydrocarbon tail. The small size of these head groups is expected to decrease the steric hindrance of the fluorophores, thereby increasing diffusion rate. Moreover, slower diffusion rates are still expected for heavier molecules. However, the interaction between the charged moieties offers an additional piece to consider. To begin, **Figure 16** displays the representative correlation curves for Rhodamine 6G and Alexa 546 in a CBWC BμE. Using the relationship of parameters outlined in Equation 7, the diffusion coefficient of Rhodamine 6G was calculated to be 45.40 ± 0.66 $\mu m^2/s$, while the diffusion coefficient of Alexa 546 in the CBWC BμE was found to be 26.81± 0.30 $\mu m^2/s$.

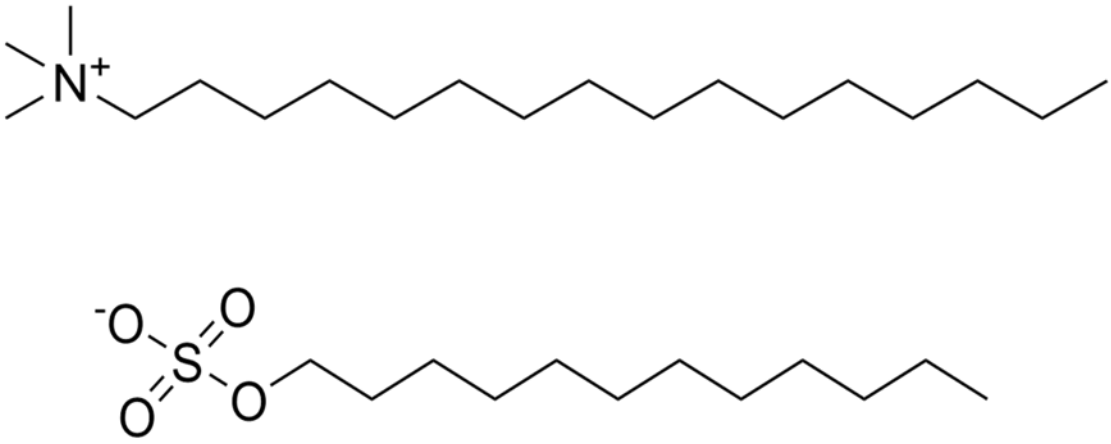


Figure 15. Molecular Structure of CTAB (top) and SDS) bottom. CTAB has a positively charged head group, while SDS has a negatively charged head group.

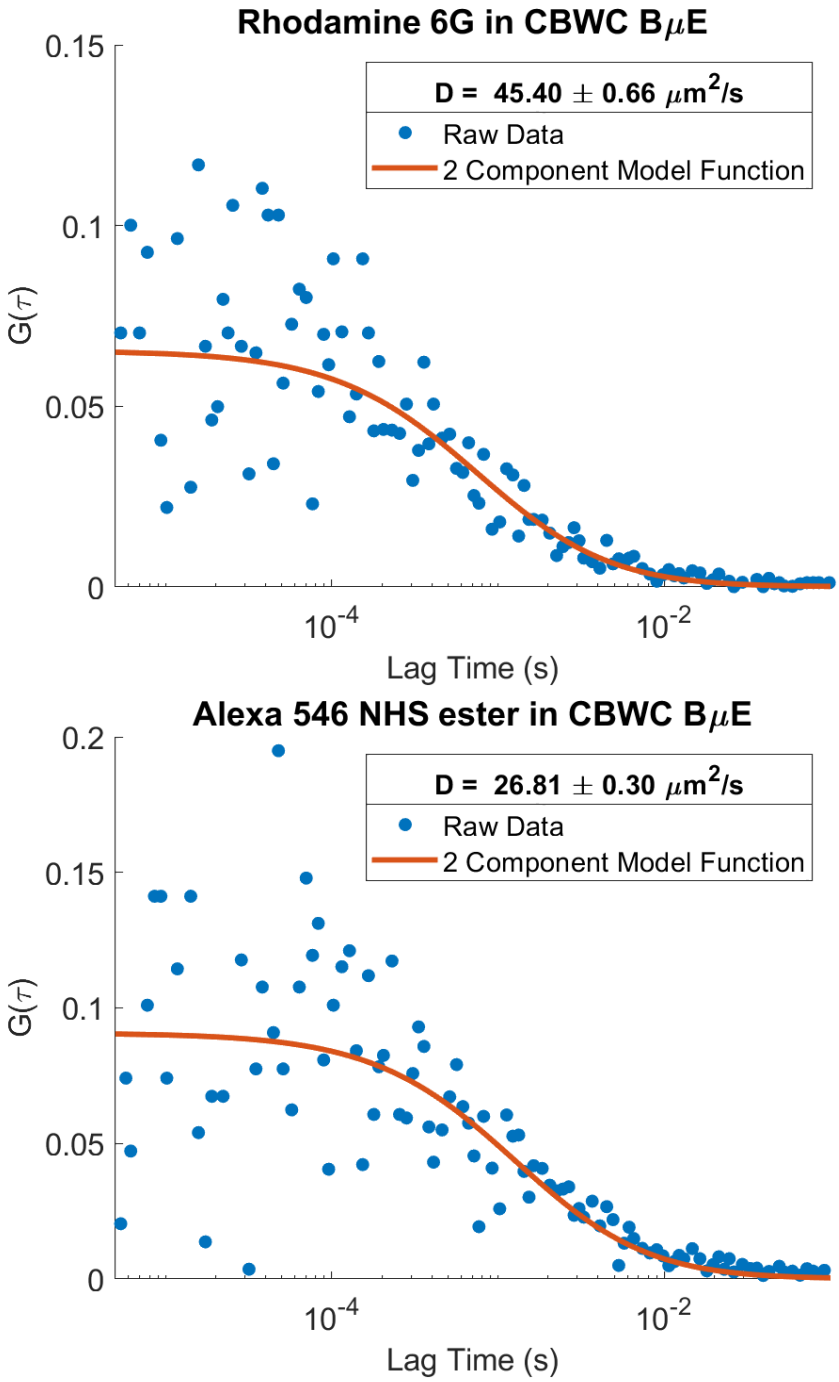


Figure 16. FCS correlation curves of Alexa 546 in CBWC (top) and Rhodamine 6G in CBWC (bottom).

These diffusion coefficients are also shown in **Figure 12.** As seen in our previous systems, the translational diffusion rate of the lighter Rhodamine 6G is faster than the diffusion rate of the heavier Alexa 546. Also, both diffusion coefficients are well outside of the error ranges of the diffusion coefficients calculated for the nonionic surfactant systems. This could be an indication of how a smaller head group surfactant is influencing the translational diffusion of the fluorophores. Looking at the role of electrostatic interactions, Rhodamine 6G and Alexa 546 possess cationic and anionic charged functional groups, respectively. Because of this, it is anticipated that the oppositely charged Alexa 546 will be attracted to the quaternary ammonium compound, resulting in a slower diffusion speed of the fluorophore. In contrast, the repulsion of like charged species should result in faster diffusion of the like charged fluorophore. Examining the translational diffusion results, the fluorophores are behaving as expected, with the like charged Rhodamine 6G moving faster than the oppositely charged Alexa 546. However, this may also be attributed to the larger size of Alexa 546. To determine which factor may be more dominating, FCS experiments were performed in a BμE containing the anionic surfactant SDS. The obtained representative FCS correlation curves for SBWC BμE are displayed in **Figure 17**. From the fit, the diffusion coefficient of Rhodamine 6G in SBWC was calculated to be 64.59 ± 7.10 $\mu m^2/s$, while Alexa 546 had a diffusion coefficient of 44.18 ± 4.52 $\mu m^2/s$, and these are both displayed in the diffusion coefficient bar graph in **Figure 12**. Examining Alexa 546, the diffusion coefficient is faster in the SBWC system than in the CBWC system, which could be due to the electrostatic repulsion between the fluorophore and the negatively charged sulfate head group. However, a surprising result occurs when examining the diffusion behavior of Rhodamine 6G. Compared to the diffusion in the CBWC BμE, the diffusion in SBWC is even faster, which was

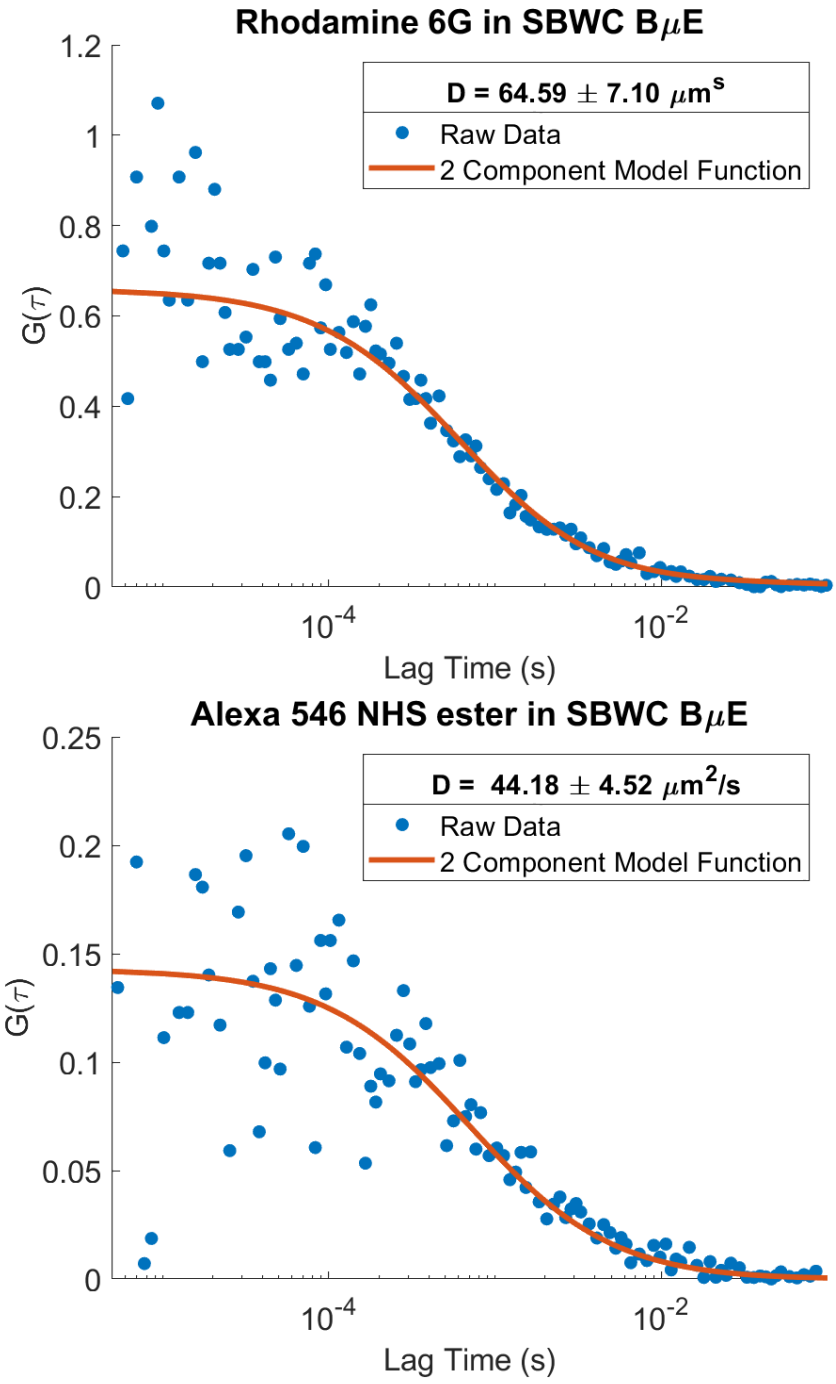


Figure 17. Representative FCS curves of Rhodamine 6G (top) and Alexa 546 (bottom) in SBWC.

not expected considering the opposite charges of the molecules. Because of this, we questioned how the surfactant packing and organization itself could influence the probe diffusion. Comparing the two microemulsion compositions, it was noted that the CBWC system contained a higher weight percent of surfactant relative to the other constituents. In BμE compositions, different concentrations of surfactant alter the molecular level dynamics of the interface itself, which could influence the translational diffusion of molecules in this region. For instance, in a study examining anionic surfactant interfaces, Ma *et al.* has reported through molecular dynamic simulations that an increase in the number of surfactant molecules in the surfactant layer would induce more interfacial curvature.[122] In addition, CTAB has a bulkier head group than SDS, which may increase the steric hindrance of the interface and impose a more tortuous diffusion path for the fluorophores. An often-used parameter for determining the type of nanostructures formed by surfactants is the CPP. In short, the CPP geometrically compares the volume created by a surfactant molecule to the base of a cylinder, expressed mathematically as $CPP = v/a_0 l$,[123] where v is the volume of the hydrophobic tail, a_0 is the effective head group area, and l is the length of the extended hydrophobic tail.[124] SDS has a reported CPP value between 0.27 and 0.34,[125] while CTAB is reported to have a much smaller CPP value of 0.07.[126] Typically, CPP values less than 1/3 will form more globular like structures in solution,[127] and this behavior has also been verified through electron microscopy images of cationic and anionic surfactant BμEs.[128] Furthermore, the dynamics of the components in BμEs, including diffusion coefficients, viscoelastic measurements, and conductivity studies, usually report faster dynamics in anionic BμEs compared to cationic systems.[109,128,129] Since FCS approximates how long molecules are diffusing in the observation volume, a more winding pathway inside the volume

may simulate slower diffusion rates as opposed to a more aligned interfacial layer, but it is difficult to isolate this behavior without proper structure characterization methods. Moreover, the role the electrostatic interactions is still unclear based on the faster diffusion of Rhodamine 6G in SBWC compared to CBWC. Also, the differing size of the oppositely charged Alexa 546 and Rhodamine 6G presents another factor to consider when analyzing data, making comparison of the diffusion results between these two dyes challenging. Future directions of this study could examine the translational diffusion of a negatively charged probe that has a similar size to one of these molecules, such as Fluorescein disodium salt compared to Rhodamine 6G. This dye could be placed in both microemulsions, and the obtained results compared to these two sets of data. Nevertheless, the FCS results clearly indicate that the SBWC BμE creates a more fluid environment for molecular translational diffusion compared to the CBWC BμE.

Thus far, FCS results have suggested that molecular size, surfactant head group size, and surfactant structure will impact the translational diffusion rate of small molecules in BμEs. Specifically, heavier molecules will diffuse slower than lighter ones, while larger surfactant head groups tend to inhibit diffusion capabilities even more. From this work, we sought to provide more context for the various factors that could be influencing the translational diffusion results. From this, more information regarding the dynamics of the interfacial film itself could also be inferred. To accomplish this, calculations of the microviscosity and water penetration of the interfacial layer, as well as rotational anisotropy measurements of a surfactant mix dissolved probe, were performed and are discussed in the following section.

3.4 Further Investigation of Interfacial Dynamics and Probe Rotational Diffusion

3.4.1 Microviscosity Calculations and Discussion

It has been established that the heterogenous nature of complex fluids affects the macroscopic mechanical properties of the mixture. Rheology, or the study of the flow of a solution, is a commonly studied mechanical property of complex fluids towards the development of new products.[1,2,9,24,130] Typically, rheological measurements of complex fluids examine the average bulk viscosity of the fluids using large sample sizes, making it difficult to examine the viscosity of small regions in heterogeneous environments.[131] Because of this, a different methodology, microrheology, is employed to study the viscoelastic properties of complex fluids at micrometer length scales and smaller sample volumes. FCS, due to its sub-micron sized detection volume, is one such microrheological technique that has been applied to complex fluids with a great degree of success.[121,132,133] In a more simplified method compared to these published works, the calculated diffusion coefficients from FCS curve fitting are related to the viscosity of the microenvironment through the Stokes-Einstein equation, as shown in Equation 9 below.

$$\eta = \frac{k_B T}{6\pi D r} \tag{9}$$

Where η is the microviscosity, k_B is the Boltzmann constant, T is the temperature of the surrounding environment, D is the diffusion coefficient of the molecule, and r is the hydrodynamic radius of the molecule. The temperature was set to 293.15 K, and the hydrodynamic radius of the Alexa 546 and Rhodamine 6G molecules were calculated to be 0.635 nm and 0.527 nm, respectively. It is important to note that the hydrodynamic radii of the two molecules were calculated using the known diffusion coefficient values in water at the reported

temperatures from the literature.[92,117] The calculated microviscosities, with error from the three runs for each system taken into account, are displayed in

Table 1 for Alexa 546 and **Error! Reference source not found.** for Rhodamine 6G. The table is arranged in ascending microviscosity value order. For comparison, the viscosity of the individual components at room temperature in centipoise (cP) is ~1 for water, 2.57 cP for 1-butanol, and 240 cP for Triton X-100. Since SDS and CTAB are solids, their viscosity values depend on the surrounding environment and materials, and to my knowledge, there is not a reported viscosity value for Brij O-10, but from qualitative observations in the lab, the material is extremely viscous, much like Triton X-100. The results indicate that, in each case, the fluorophore is diffusing through an environment that displays a viscosity that is set between the values of the water phase and the surfactant phase, which further supports the notion that the molecules are diffusing within the low-tension region created by the interfacial film of the BμE. It is also interesting to note that despite the differences in diffusion coefficients between the fluorophores, particularly in the values obtained in the ionic surfactants, the order of increasing microviscosity values is the same for both probes, demonstrating that both fluorophores are sensing a similar microenvironment within the BμE with minor regard for molecular size or charge. A comprehensive study on aqueous surfactant micelle microviscosities published by Zana has stated that the microviscosity of the interface is largely independent of surfactant concentration.[134] Other relevant information from this publication reported that, at headgroup size, and constant temperature, the microviscosity increased with the size of the surfactant chain length and the ionic surfactants typically displayed lower microviscosity values than nonionic surfactants. In addition, Zana postulated that deeper partitioning of the probe in the surfactant

layer would result in a higher recorded microviscosity value, which supports the claim that the molecule is penetrating the larger head groups of the nonionic surfactants. However, this paper

Table 1. Calculated microviscosity values for A546 in each microemulsion.

Surfactant	Average MV A546 (cP)	Calculated error
SDS	**8.305938484**	**0.31805165**
CTAB	**11.21952764**	**0.87380131**
Brij O10 (25% W)	**22.03478313**	**1.635813059**
Triton X-100	**31.49516671**	**6.295347259**

Table 2. Calculated microviscosities in each BμE based on diffusion coefficients from Rhodamine 6G in each system. Larger head group surfactants yielded the highest microviscosity values.

Surfactant	Average MV R6G (cP)	Calculated error
SDS	**5.414829693**	**0.119268523**
CTAB	**8.166016775**	**0.503343872**
Brij O10 (25% W)	**15.75306193**	**1.481580187**
Triton X-100	**26.94798176**	**2.494896968**

also suggested that an attractive electrostatic interaction between oppositely charged probes and surfactant head groups would result in higher microviscosity values, a trend not seen for Rhodamine 6G in SBWC in our results. Further tests are needed to fully understand the dynamics within this system. It is worth mentioning that while the information provided by the Stokes-Einstein equation provides a general approximation of the microviscosity of the diffusing environment, this equation assumes a spherical molecule diffusing through a majority homogenous environment. More involved measurements incorporating nonspherical molecule shape and degree of interfacial crowding in complex fluids may be required to more accurately determine the microviscosity of the diffusing environment using FCS.[121,132,134,135]

3.4.2 Generalized Polarization of Laurdan

Another point of interest for providing more context on the inner behavior of the BμEs studied here is how much water can penetrate the interfacial layer, which could be creating a more fluid microenvironment for the diffusing species. Laurdan is a polar molecule that has been a popular fluorophore in the study of interfacial dynamics due to its ability to shift its fluorescence spectrum based on the polarity of its environment.[136,137] Simply, if Laurdan is residing in a more polar environment, the fluorescence emission spectrum displays a red shift, while the opposite is true for a more nonpolar or neutral environment[138]. This characteristic is advantageous towards the measuring of the degree of water penetration in the interfacial layer of BμEs. To achieve this, a measurement of the generalized polarization (GP) value is performed in each microemulsion tested above. GP is a ratio of the emission of a bluer shifted or red shifted wavelength of Laurdan emission, and this relationship is denoted in Equation 10.

$$GP = \frac{(I_B - I_R)}{(I_B + I_R)} \quad (10)$$

Where I_B is the intensity of fluorescence emission at 440 nm and I_R is the fluorescence emission at 490 nm. The typical range of GP is between -1 and +1. A more negative GP value reveals increased water penetration and a more disordered interfacial layer, while a more positive GP value reveals a more ordered interface.[136,137] In BµEs, a more disordered interface is suspected to allow for increased water penetration and increased diffusion speed of the molecule in the interfacial layer. **Table 3** summarizes the results of the GP measurements of Laurdan in each microemulsion.

The water percentage of each microemulsion is also shown in parentheses to provide additional context. It is worth noting that, in addition to the microemulsions tested above for FCS, GP measurements on a second BWBI BµE with a 50% water composition was tested to better compare the water penetration level all systems. In all microemulsions, the negative Laurdan GP values indicate that the interfacial layer tends to form a more disordered film. However, the degree of this disorder does vary. Ionic surfactants yielded the highest water penetration, and thus the most disorganized interface, which is expected due to the high-water solubility of these head groups. Interestingly, the CBWC BµE demonstrated a higher level of water penetration than the SBWC system, even though the diffusion coefficients of the probes are slower in the former than the latter. From our FCS work and rotational dynamic studies by Hassan *et al.*[103], we have shown that an increase in water content does not necessarily indicate faster diffusion. This effect is also witnessed in the nonionic systems. The GP value for the TxBWC BµE signifies a disordered interface, and

Table 3. GP values of Laurdan in each bicontinuous microemulsion. The smaller surfactant structures allow for increased water penetration into the interfacial layer.

Surfactant (Water %)	GP Value
Brij O-10 (25%)	**-0.212761±0.0009**
Brij O-10 (50%)	**-0.47176±0.004**
Triton X-100 (60%)	**-0.480074±0.0003**
SDS (52%)	**-0.715014±0.002**
CTAB (35%)	**-0.775649±0.0005**

Yet this system produced the slowest diffusion coefficients out of all systems tested. Furthermore, 25% water BWBI BμE produced slightly higher diffusion coefficients compared to Triton X-100, even after increasing the water percentage to 50% and more than doubling the water penetration, very similar diffusion coefficients were obtained, as shown in the previous section. Therefore, we interpret these results as stating that while water penetration can induce more fluidity in the interfacial layer and allow for additional small molecule intercalation in the surfactant region, the larger contribution to translational probe dynamics stems from the structure of the surfactant itself. Specifically, bulkier surfactant head groups and larger total length surfactants inhibit diffusion capabilities through increased steric hindrance, while smaller head group surfactants allow for freer translational diffusion.

3.4.3 Steady State Anisotropy

The series of experiments presented thus far have revealed valuable insight into the molecular level dynamics of small molecules diffusing near an amphiphilic interface. In the final set of experiments examining BμEs, we sought to examine the rotational dynamics of a small molecule placed in the interfacial region to complement the translational diffusion information obtained. Fluorescence anisotropy is a measure of the rotational dynamics of a fluorophore through the collection of polarized emission.[79] If the fluorophore's transition moment is oriented along the electric vector of the excitation source, the molecule's fluorescence emission is also polarized along that axis. Through rotation of the transition moment of the molecule, fluorescence emission is said to be depolarized, and the polarization angle is changed. By measuring the intensity ratio between the parallel and perpendicular axes of polarized emission,

the anisotropy value can be calculated to estimate the rate of molecular rotation in an environment. This relationship is displayed in Equation 11.

$$\langle r \rangle = \frac{I_{vv} - I_{VH}G}{I_{VV} + 2I_{VH}G} \quad (11)$$

Where I_{VV} is the fluorescence intensity at vertical excitation and vertical emission, I_{VH} fluorescence intensity at vertical excitation and horizontal emission, and G is the is the correction factor to account for detector sensitivity, denoted as I_{HV}/I_{HH}. A commonly used fluorescence probe for this purpose in cellular membrane lipid bilayers and model membranes is the nonpolar probe 1,6-diphenyl-1,3,5-hexatriene (DPH).[139–142] Anisotropy results from DPH in each microemulsion are shown in **Table 4.** Measured anisotropy values and standard deviations in each microemulsion using steady state fluorescence.

. Because of the large standard deviations in these results, a definitive conclusion regarding the rotational freedom of DPH in each microemulsion could not be determined. When examining potential issues, it was found that DPH had difficulty dissolving in

Table 4. Measured anisotropy values and standard deviations in each microemulsion using steady state fluorescence.

Microemulsion	Anisotropy (% Standard Deviation)
SBWC	**0.07913 (14.3529 %)**
CBWC	**0.01713 (128.9185%)**
TxBWC	**0.01859 (48.8217 %)**
BWBI (25% water)	**0.01474 (273.6732 %)**

the oil phase of each microemulsion. The DPH molecule should partition in the hydrophobic portion of the surfactant, but low solubility in the bulk oil phase could be causing the low signal to noise ratio. Alternative methods of dissolving the DPH in either the surfactant mixture or all four components together were then attempted. Despite normal fluorescence emission measurements displaying a fluorescence peak in line with the emission peak of DPH at ~420-426 nm, no improvements to the standard deviation measurements were seen when anisotropy experiments were performed. In future experiments, sonication could be implemented to improve the solubility of DPH in either the oil phase or complete microemulsion. If these experiments were to be unsuccessful, alternative common dyes could be used, such as Nile Red[143] or fluoresceine-isothiocyante.[144]

3.5 Conclusion

The investigation of molecular level dynamics within a series of BμEs has been presented through FCS experiments, GP studies, and fluorescence anisotropy measurements. The obtained diffusion coefficients from FCS measurements demonstrate that the fluorophores are diffusing in the surfactant layer of the microemulsions, and that lighter molecules tend to diffuse faster than heavier ones. Microviscosity calculations also support this claim, and GP measurements of water penetration show that smaller surfactants will allow for more water penetration. Therefore, we

conclude that the primary factor dictating molecular translational diffusion stems from the length of the surfactant head group penetrating the aqueous phase of the microemulsion and the bulkiness of both the head and tail regions of the surfactant. Specifically, larger length head groups are suspected to trap diffusing fluorophores and interfere with their free diffusion pathway, while bulkier head and tail regions may increase the packing of the surfactant layer and rigidify the interface. The diffusion coefficients in ionic surfactants were shown to be higher than those in nonionic surfactants, and while the smaller size of the surfactants is suspected to increase the diffusion rate, the role of charge interactions between the surfactant head and the fluorophore is still uncertain. Future studies incorporating a negatively charged probe can provide further insight into the role of electrostatic interactions on translational diffusion. Additionally, some applications of BμEs depend on their organization at a solid-liquid interface, and examining the molecular level dynamics in this region using a TIR-FCS instrument can connect bulk to surface translational diffusion behaviors within these systems.

CHAPTER FOUR

GUV STUDIES

4.1 Motivation

As stated previously, antibiotic resistance has emerged as a significant health concern in the 21st century. In 2019, an estimated with 1.27 million deaths were directly caused by antibiotic resistance.[56] In response to this issue, new efforts to combat antibiotic resistance through targeted drug delivery must be developed. Cellular membranes, which serve as the first line of defense against potential threats to a cell's health, are composed of various phospholipids and proteins that form a bilayer surrounding the interior components of the cell.[145] Phospholipids are amphiphilic molecules that contain a hydrophilic head group and two hydrocarbon tails. They are highly mobile along the bilayer membrane, laterally diffusing along the monolayer in which they reside and exchanging positions with a neighboring lipid molecule approximately 10^7 times per second.[146] Furthermore, the composition of the bilayer and the structure of the lipids themselves influence the fluidity of the membrane.[123,146–148] For example, in mammalian cells, the lipids usually contain saturated and unsaturated hydrocarbon tails, or those without any double bonds and those with at least one double bond, respectively. The double bond in the unsaturated chain of the lipid causes a kink in the direction of the tail, thereby reducing the packing of the lipids and increasing the fluidity of the membrane. Different ratios of saturated and unsaturated lipids in the mammalian cell membrane result in different subregions, or rafts, being formed that each experience different biophysical properties and molecular motion.[147–149] In a similar fashion, bacterial cell membranes exhibit compartmentalization of cellular processes through the formation of functional membrane microdomains (FMMs).[147,150] While bacterial cell membranes

also contain saturated phospholipids in their bilayer, they significantly lack the same number of unsaturated lipids in their composition. Instead, bacterial membranes more commonly possess lipids that have a small methyl group at the end of the tail region, also known as branched fatty acyl chains (BFACs).[147,151] These BFACs are hypothesized to increase membrane fluidity similarly to how unsaturated lipids do so in mammalian cells.[152–155] A recent 2019 study by Mostofian *et al.* used molecular dynamic simulations to examine how BFACs impact the biophysical properties of lipid bilayers.[152] The authors found that an increase in BFAC composition led to an increase in leaflet overlap, a thinner hydrophobic region, and a decrease in lipid packing, all of which indicating the fluidity of the membrane will increase with the introduction of BFACs. Additionally, the leaflet overlap parameter was compared to a simulation that utilized a single, unsaturated lipid, and all simulations containing BFACs produced a higher leaflet overlap percentage than the unsaturated lipid result. Similarly, Kannenberg *et al.* reported that BFACs display higher energies and less degrees of order in both monolayers and bilayers compared to saturated hydrocarbons.[156] While these results are promising, the lateral diffusion behavior of small probe molecules in a lipid bilayer containing BFACs is still untested, and this parameter is an essential aspect of new drug development to combat antibiotic resistance.

As demonstrated, FCS is a useful technique designed to examine the lateral diffusion rates of small molecules in complex fluids. To provide a controlled environment to study this behavior, GUVs containing a BFAC will be inspected using FCS. As stated previously, GUVs are spherical, biomimetic models of a lipid bilayer, offering enhanced controllability and functionality for membrane studies.[58,157] Using FCS, an approximation of the membrane fluidity can be determined through calculation of diffusion coefficients of fluorophores laterally

diffusing along the membrane of a single GUV. There have been numerous instances of FCS being applied to the study of probe lateral diffusion in homogeneous and heterogenous GUVs,[59–62,158–160] but the GUVs under study in these studies have been binary or ternary mixtures of typical mammalian cell phospholipids, such as saturated Dipalmitoylphosphatidylcholine (DPPC) and 1,2-dilauroyl-sn-glycero-3-phosphocholine (DLPC), unsaturated 1,2-dioleoyl-sn-glycero-3-phosphocholine (DOPC), and cholesterol. Although bacterial membranes do not contain cholesterol, these previous FCS studies offer a good starting point to begin examining the role of BFACs on membrane fluidity. A particularly interesting study presented by Scherfeld *et al.* found that, in a GUV containing DOPC, DPPC, and cholesterol at an equal phospholipid ratio, the diffusion coefficient of the fluorescent probe decreased with increasing cholesterol content.[161] Similarly, Korlach *et al.* witnessed the same trend in reducing diffusion coefficients as a result of increasing cholesterol content in a GUV containing 0.5/0.5 DLPC/DPPC and cholesterol.[61] Kahya *et al.* reports that when the cholesterol content is increased in a vesicle containing a single, high phase transition temperature lipid, such as the saturated DPPC (T = 41.3°C), the fluidity of the bilayer will increase.[60] However, an opposite "condensing" effect is observed in GUVs containing a lipid with a lower phase transition temperature, such as the unsaturated DOPC (T = -20°C).[60,162] By examining the obtained diffusion coefficients at similar cholesterol contents, it is found that the probe laterally diffuses faster in the GUVs containing the unsaturated lipid than in the GUV containing only saturated lipids, which indicates that the decrease in lipid packing caused by the unsaturated lipid increases membrane fluidity. The ternary mixture of an unsaturated lipid, a saturated lipid, and cholesterol at a higher cholesterol content (≥ 30%) often produces a homogeneous distribution of lipids that could be showcasing a

mixture of the dynamic behavior between the two main phases. The homogenous environment offers a simple and effective system to begin FCS analysis as the curve should indicate one diffusing species, making model fitting less difficult. Furthermore, cholesterol is reported to react more readily with saturated PC lipids than unsaturated lipids,[163–167] which could enhance the "fluidizing" effect of cholesterol on higher phase transition temperature lipids if the unsaturated lipid is replaced by a BFAC. As mentioned earlier, BFACs are suspected to increase the bacterial membrane fluidity like how unsaturated lipids do so in mammalian cellular membranes. As FCS has not previously been applied to the study of BFACs in a GUV, the vesicles used here were comprised of the saturated lipid DPPC, cholesterol, and the BFAC a15:0-i15:0PC at a 1:1 lipid ratio and 40% cholesterol. Furthermore, these GUVs are used to assist in further characterization of the dimensions of the point spread function for FCS analysis. Based on the results of previous BFAC molecular dynamic simulations and FCS experiments on GUVs, we hypothesized that the diffusion coefficients of probes in the GUVs containing BFACs will be larger than those obtained in GUVs housing a mixture of unsaturated and saturated lipids.

4.2 Sample Preparation

The GUVs used in this study were prepared using an electroformation procedure.[168] The vesicles contained three main components: cholesterol, dipalmitoyl phosphatidylcholine (DPPC), and a15:0-i15:0PC. All lipids were purchased from Avanti Polar Lipids. The structure of each of these components is displayed in **Figure 18**. Chloroform stock solutions of each lipid are used to prepare the mixture with a a15:0-i15:0PC:DPPC ratio of 1:1. The final mole percentage of each component is as follows: 40% cholesterol, 30% DPPC, and 30% a15:0-i15:0PC. This

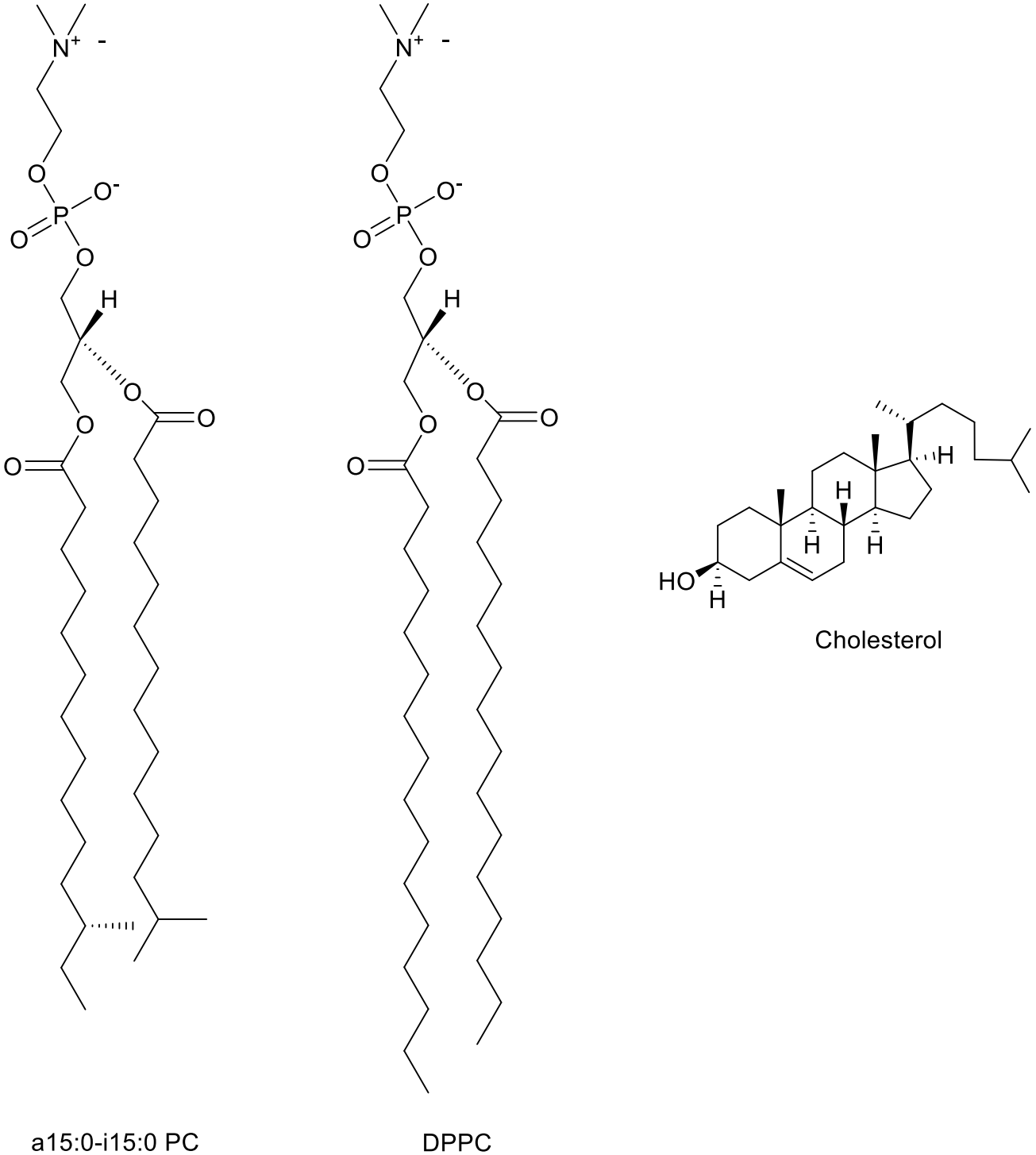


Figure 18. Structure of components for GUV Formation. a15:0-i15:0 PC is the BCFA used in this GUV, DPPC is the saturated lipid, and cholesterol is the sterol molecule.

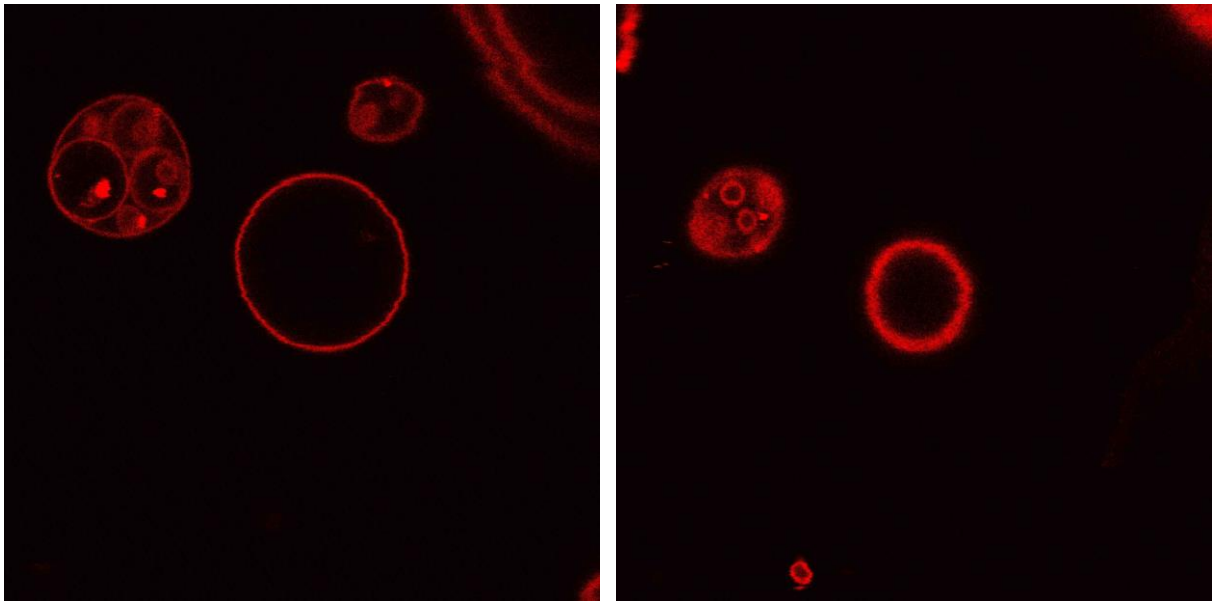


Figure 19. Confocal microscopy images of the a15:0-i15:0 PC, DPPC, and cholesterol GUV. The GUV exhibited no phase separation and a homogenous distribution of dye around the entirety of the lipid bilayer.

allowed to rest for at least 30 minutes to allow for GUV adhesion to the surface before placing the device on the microscope stage for experimentation.

4.3 Study of GUVs Containing BCFAs

4.3.1 Adhesion Method Tests

To isolate the translational diffusion of the fluorophores across the GUV membrane, the GUV itself must be locked down on the glass coverslip. Any motion originating from the motion of the sample as opposed to the motion of fluorophores within the sample will not provide an accurate measurement of the membrane fluidity. This can be problematic with untreated coverslips, as contaminants on the surface can cause GUVs to become unsettled from the glass substrate. In previous FCS measurements on GUVs, only a few mention procedures for coverslip cleaning and adhesion methods. Typical methods involve washing the coverslips in a KOH/ethanol solution,[62] plasma cleaning the coverslips,[64] or applying an albumin from bovine coating mixed with phosphate buffered saline solution.[169] Our lab has previous experience adhering live bacterial cells to coverslips, and one of these methods was attempted first. Firstly, the commercialized product CellTak was purchased from Corning and applied to the No. 1.5 coverslip. CellTak utilizes polyphenolic proteins secreted by Mytilus edulis, which exhibit adhesive properties to both surfaces and cellular membranes.[170] 20 μL of the CellTak solution was placed on a coverslip, and another coverslip was placed in a cross pattern to allow the solution to spread across both surfaces. After 30 minutes, the solution was rinsed with water thricely before a drop of GUV solution was placed over the coating. While this method seemed promising in the beginning, it was observed that over time, the GUVs adhered to the surface were still mobile. However, it was noticed that the GUV motion was largely reduced compared to a device where no adhesive coating was applied to the coverslip. For the next attempt, the coverslips were plasma cleaned to further reduce contaminants on the surface. In plasma

cleaning, ions, electrons, and radicals are generated, and when these particles interact with contaminants on a solid surface, they can dislodge them from the surface through processes including heating, ablation, sputtering, etching, or cross linking.[171] Our lab owns a Harrick Plasma High Power Expanded Plasma Cleaner that generates a plasma stream via a radio frequency (RF) electric field oscillating via magnetic induction through a gas region. The coverslips were subjected to plasma cleaning for approximately 12 minutes before a 40 µL aliquot of GUV solution was placed on the slide and covered with a perfusion well chamber. The GUVs were allowed to settle on the coverslip for 1 hour in the microscope stage. After this, a simple brightfield microscopy method was used to locate the adhered GUVs. The plasma cleaning method produced better results with multiple adhered vesicles displaying minimal to no translational movement. Because of these results, plasma cleaning was used as the standard coverslip cleaning procedure for the experiments moving forward.

4.3.2 Further Focal Volume Characterization and Positioning for FCS Studies

As stated before, the calibration of the focal volume is an essential component for performing accurate FCS measurements. Furthermore, FCS studies on GUVs require the focal volume to be placed at the topmost side of the GUV adhered to the coverslip. From the FCS calibration measurements, the lateral $1/e^2$ radius of the focal volume was calculated to be 530.4 ± 17.4 nm, which was slightly larger than expected. Before performing FCS experiments examining lateral diffusion in a GUV containing a BCFA, we sought to confirm the accuracy of the calculated focal volume. The thickness of the lipid bilayer in a GUV is only a few nanometers wide[172,173] and significantly smaller than the diffraction limited spot of the laser focus. By performing a lateral and axial scan of the widest and topmost part of the GUV and

plotting the fluorescence intensity as a function of position, an estimate of the focal volume can be calculated. The scan was performed by moving the stage through the focal spot with a Physik Instrumente (PI) Piezo XYZ stage controlled with a custom LabVIEW code. GUVs that possessed a high concentration of LR were adhered using plasma cleaned slides and coarsely positioned using brightfield microscopy. From there, lateral and axial scans of fluorescence intensity vs. position were performed at the highest and widest part of the GUV. As the membrane of the GUV passes through the focal spot of the laser, the fluorescence intensity increases and decreases, and the plot follows a Gaussian distribution. By fitting the plot to a single component Gaussian model produced from MATLAB's curve fitting app, the approximate $1/e^2$ width of the Gaussian profile is calculated. The Gaussian equation used for fitting is shown in Equation 12.

$$y = a_1 \exp\left(-\left(\frac{x-b_1}{c_1}\right)^2\right) \qquad (12)$$

In this model, a_1 represents the height of the curve peak, b_1 represents the position of the center of the peak, and c_1 is the standard deviation, which controls the width of the bell curve. A representative intensity vs. position profile of the axial and lateral scans of an adhered GUV are shown in **Figure 20**. Examining the axial scan, ten scans were obtained and fit individually. From there, the FHWM and $1/e^2$ radius values for each fit were determined, and the standard errors were calculated. The ten scans produced a FWHM average of 2.7010 ± 0.139 μm. Multiplying this number by 0.8495, which produces the approximate $1/e^2$ radius of the PSF, we obtain a $1/e^2$ axial radius of value of 2.294 ± 0.118 μm. For the lateral scan, six plots were obtained and fitted using the same Gaussian function as the axial scan. It is worth noting that the shoulder in both the lateral and the axial scan arose from the average intensity values at positions

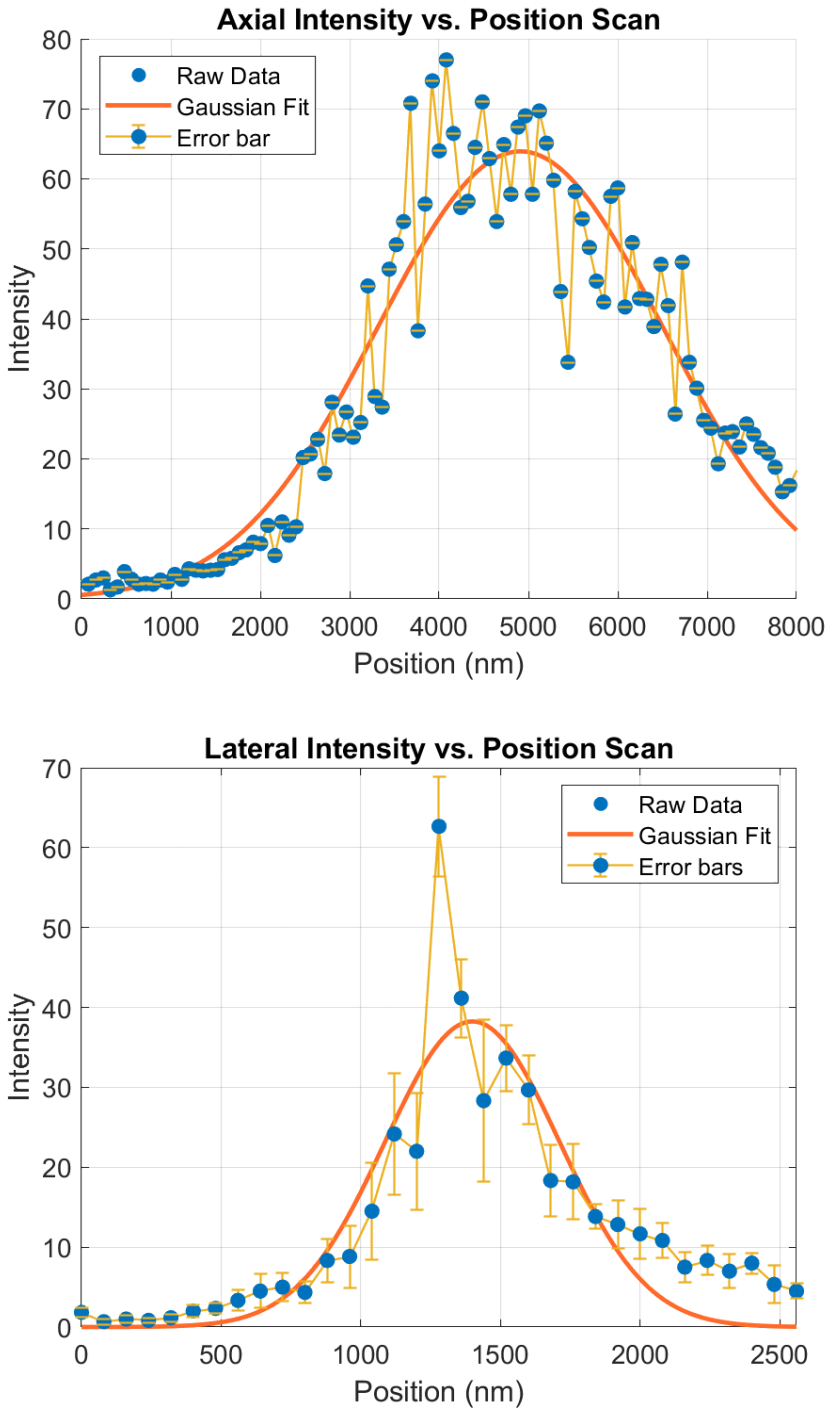


Figure 20. Axial (top) and lateral (bottom) intensity vs. position results obtained from stage scanning through a fluorescently labeled GUV. The results matched the dimensions calculated form FCS calibration methods.

calculated inside the GUV. Oftentimes, the fluorescence intensity in this region did not fully decay to zero, but the fits were not improved or worsened if more points were used in the FWHM calculations. From the six plots,an average FWHM of 706.4 ± 72.8 nm is obtained, and multiplying this number by 0.8495, we obtain a $1/e^2$ radius of 598.0 ± 61.8 nm, and three of the scans produced $1/e^2$ values within a few nanometers 530 nm. This value matches very well with the FCS calibrated value of 530.4 ± 17.4 nm. In addition, the ratio of the axial to lateral radius, or the structure parameter in FCS, is found to be 3.8:1, which is within the range of other published works.[174,175] Also, it has been noted that higher laser intensity values in TPE-FCS can enlarge the focal volume of the PSF.[86,93] Since FCS experiments were performed using average intensity values measured directly outside the microscopy body of 40-50 mW, it is possible that this higher power is the cause of the slightly enlarged dimensions calculated through both FCS and position scanning techniques. Nevertheless, the results of the stage scanning experiment worked to confirm the dimensions of the PSF calculated through FCS calibration methods. Furthermore, the stage scanning system allowed us to accurately position the stage at the top of the GUV for FCS measurements.

4.3.3 FCS Experiments on a GUV Containing a Branched Chain Lipid

With the dimensions of the focal volume confirmed and the positioning system in place, FCS trials on GUVs were ready to be performed. As mentioned, the GUV selected for study contained a composition of 40 mole percent cholesterol, 30 mole percent DPPC, and 30 mole percent 15:0-i15:0PC. We hypothesized that the BFAC will increase the fluidity of the membrane and cause the tracer fluorophore to diffuse faster through the membrane than in systems containing only saturated lipids or a combination of saturated and unsaturated

molecules. Furthermore, based on previous FCS measurements on GUVs, a membrane that displays no phase separation will produce a curve that can be satisfactorily fit with a single component 2D Gaussian model function.[59,61,176] This model function is shown in Equation 13.

$$G(\tau) = \frac{1}{N}\left(1 + \frac{\tau}{\tau_D}\right)^{-1} \quad (13)$$

The 2D diffusion model takes the same form as the 3D diffusion model shown in Equation 4 except for the third term that accounts for the axial axis contribution. To start, a preliminary FCS curve of FM1-43, a molecule that has a high affinity for lipid membranes[177] and a common probe used in our lab,[178,179] in a BFAC was obtained. The calculated diffusion coefficient of FM1-43 was 217.27 ± 37.02 $\mu m^2/s$. Lipids within cellular membranes and vesicles have a typical diffusion rate of 0.1-10 $\mu m^2/s$,[146,180,181] so while the faster diffusion rate compared to GUVs with unsaturated lipids supports our hypothesis, the significantly higher value compared to the normal range of diffusion rates in lipid bilayers led us to believe that this curve was obtained in the bulk region of the solution. Furthermore, when testing this solution, it was noticed that there was a steady count rate on the APDs of 1000-2000 counts per second in the bulk solution and within the interior of the membrane, making it difficult to determine the correct position needed for proper FCS measurements. To fix these issues, the FM1-43 solution was vortexed lightly to improve mixing and given more time for the dye to interact with the vesicle's bilayer. Both actions resulted in the background fluorescence in this solution significantly reducing, so this procedure was implemented moving forward. Before FCS attempts were made on new samples prepared with this method, GUVs were visualized on the camera to ensure the sample being measured did not contain any internal structures. A representative figure displaying an FCS result on this solution is shown in **Figure 21**. From the 2D model fits, a diffusion coefficient for

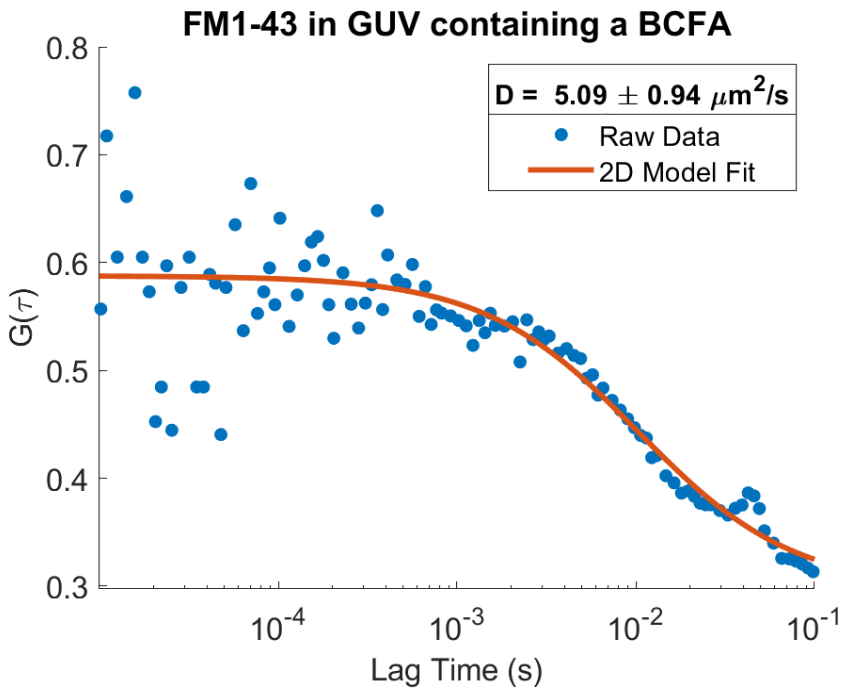


Figure 21. FCS result from FM1-43 in a GUV containing a BCFA. The diffusion rate extracted here is faster than those witnessed in unsaturated lipid systems.

FM1-43 of 5.09 ± 0.94 $\mu m^2/s$ was calculated. The standard error of this value is ±18.5%, which matches well with reported diffusion coefficients of dyes in GUVs from the literature, which are often reported with ±20% error. Furthermore, a previous FCS study on GUVs reported that diffusion coefficients of a dye placedin a homogenous GUV composed of DOPC/DPPC/cholesterol at cholesterol percentages of 33% and 50% reported diffusion coefficient values of 2.5 ± 0.2 $\mu m^2/s$ and 1.85 ± 0.13 $\mu m^2/s$, respectively.[161] Based on these results, the diffusion coefficient obtained in a GUV containing a BCFA is twice as fast as those obtained in a ternary mixture of a saturated lipid, an unsaturated lipid, and cholesterol at a similar composition. This result supports our hypothesis that branched chains housed on BCFAs would increase membrane fluidity more than unsaturated lipids. Probing this result deeper, the a15:0-i15:0PC lipid contains two branched methyl groups. Poger et al. have witnessed that lipid structures with more than one branched chain will increase the surface area per lipid and decrease the bilayer thickness, both effects producing a more fluid bilayer.[154] The presence of two branched chains on the a15:0-i15:0PC lipid tails could be increasing the surface area per lipid and reducing the Van der Waals forces between lipids, thereby enhancing the fluidity of the membrane even more compared to what molecular dynamic studies have shown for single branched chain molecules.[152,153] It is important to note, however, that for the raw data to be properly fitted with the model, the correlation offset needed to be adjusted from its normal position at zero. An FCS correlation curve may not decay to zero when either a large aggregate passes through the focal volume or a high number of background fluorophores are consistently present in the volume.[182] Given the high number of background counts in the sample before more

sufficient insertion of the dye into the membrane was achieved, it is possible that some residual background

fluorescence from FM-143 in the bulk solution was still present. Additionally, slight movements of the vesicle itself may introduce an additional diffusion component in the correlation curve and resist the curve decaying fully to zero. Ideally, the FCS curve would include information at lag times as far as one second, but no further information after 0.1 s was obtained due to limitation of our instrument. Future experiments should look to mitigate these issues by either incorporating the FM1-43 dye into the vesicles at an earlier time point in the vesicle preparation process or ensuring that the GUV being used for study is fully adhered to the glass coverslip. Nevertheless, initial FCS results suggest that BFACs will increase membrane fluidity more than saturated and unsaturated lipids.

4.4 Conclusion

The confirmation of the dimensions of the focal volume and the investigation of the impact BFACs have on membrane fluidity have been presented. The focal volume characterization results matched well with results obtained from FCS calibration methods, and the larger measurements compared to the theoretically calculated values are attributed to the higher power level utilized in our experiments. In the FCS experiments on GUVs, preliminary results indicated that the membrane fluidity was increased with the addition of a BFAC. This result, to the best of our knowledge, is the first instance of FCS being applied to a GUV containing a BFAC. Because of this, future directions will look to confirm the results seen with additional measurements while also incorporating other components specific to bacterial cell membranes. One such direction is to examine the impact of hopanoids, or sterol molecules

present in bacterial cells that are suspected to impact bacterial membrane fluidity much like cholesterol does in mammalian cells. Another direction will determine how lipids with the same head groups as those in bacterial cells impact membrane fluidity. These studies will allow for a more complete understanding of the behavior of bacterial membranes to combat antibiotic resistance mechanisms.

CHAPTER FIVE

CONCLUSIONS AND FUTURE DIRECTIONS

A fluorescence correlation spectroscopy instrument for detecting molecular translational diffusion in complex fluids was constructed. The FCS instrument incorporated a TPE scheme, which offered restricted fluorescence emission from a spot within the sample and eliminated out of focus fluorescence. From a detection standpoint, the fluorescence emission arising from fluorophore diffusion was collected with a cross-correlation detection setup to eliminate afterpulsing effects and offer more accurate correlation curve results. After calibration of the focal volume was performed using an aqueous solution of Alexa 546 NHS ester, the FCS instrument was successfully applied to study the impact of surfactant structure on small molecule translational diffusion in BμEs. Also, the instrument provided preliminary results on translational diffusion information in a GUV containing a BFAC.

The bicontinuous microemulsion experiments revealed interesting findings regarding the role of the surfactant monolayer on translational diffusion behavior. From FCS measurements, the fluorophores experienced the longest diffusion times in microemulsions containing large, nonionic surfactants. Furthermore, the heavier Alexa 546 molecule displayed a slower diffusion rate in all systems compared to the lighter Rhodamine 6G. Diffusion in ionic surfactants, which contained much smaller head groups and overall structures, displayed significantly faster diffusion rates for both fluorophores. Additionally, microviscosity calculations revealed that each fluorophore was experiencing similar diffusion microenvironments in each microemulsion, and generalized polarization measurements revealed that ionic surfactant BμE displayed the highest level of water penetration into the surfactant layer. This higher water penetration is suspected to

increase the fluidity of the interfacial layer and allow for faster fluorophores diffusion. However, the role of ionic charge on fluorophore diffusion is still unknown, as no definable trend between the charge on the fluorophores and the charge on the surfactant heads was found. Also, despite multiple attempts to understand the rotational freedom of molecules in the surfactant layer, unreliable results from DPH steady state anisotropy measurements persisted. Future experiments can look to observe the translational diffusion trends with a small, anionic probe that is a similar size to other tested fluorophores. For rotational anisotropy measurements, alternative solvation methods for DPH or an alternative probe can be attempted to provide more reliable results.

After examining BμEs with FCS, focus was shifted to determine the impact of BCFAs on membrane fluidity. These model systems were also utilized to confirm the dimensions of the focal volume used in FCS experiments. Firstly, by obtaining fluorescence intensity vs position scans from an adhered GUV, we were able to obtain axial and lateral dimensions that closely resembled the values obtained through FCS calibration. The result provided further support for the diffusion coefficient values calculated in the BμE study while also strengthening our confidence in the instrument's parameters as we moved into FCS studies of a new system. BCFAs are suspected to increase membrane fluidity much like unsaturated lipids do in mammalian cells, but the extent of how much the fluidity is increased is still unknown in the literature. We have obtained a preliminary FCS measurement of a styryl dye moving through a GUV containing a BCFA, and the resulting diffusion coefficient was twice as fast as those obtained in GUVs contained unsaturated lipids at a similar composition ratio. We concluded that the double branched chain lipid tails decreased the lipid packing of the bilayer to a larger extent than unsaturated lipids do. Despite this promising preliminary result, artifacts in the FCS curves

were still present, leading us to conclude that more tests are needed to confirm these results by mitigating potential causes to the artifacts. Future FCS studies on GUVs will examine the impact of hopanoids and bacterial lipid headgroups on membrane fluidity. Overall, we have constructed and calibrated a fluorescence correlation spectroscopy instrument and successfully applied it to study the small molecule dynamics within two- and three-dimensional complex fluids. The results presented here can provide valuable insight into the development of new industrial products and drugs designed to combat antibiotic resistance.

BIBLIOGRAPHY

(1) Himashree, P.; Sengar, A. S.; Sunil, C. K. Food Thickening Agents: Sources, Chemistry, Properties and Applications - A Review. *Int. J. Gastron. Food Sci.* **2022**, *27*, 100468. https://doi.org/10.1016/j.ijgfs.2022.100468.

(2) Davies, A.; Amin, S. Rheology of Cosmetic Products: Surfactant Mesophases, Foams and Emulsions. *J. Cosmet. Sci.* **2020**, *71* (6), 481–496.

(3) Lu, G.; Wang, X.-D.; Duan, Y.-Y. A Critical Review of Dynamic Wetting by Complex Fluids: From Newtonian Fluids to Non-Newtonian Fluids and Nanofluids. *Adv. Colloid Interface Sci.* **2016**, *236*, 43–62. https://doi.org/10.1016/j.cis.2016.07.004.

(4) Kunitake, M.; Kuraya, E.; Kato, D.; Niwa, O.; Nishimi, T. Electrochemistry in Bicontinuous Microemulsions Based on Control of Dynamic Solution Structures on Electrode Surfaces. *Curr. Opin. Colloid Interface Sci.* **2016**, *25*, 13–26. https://doi.org/10.1016/j.cocis.2016.05.004.

(5) Peng, J.; Cantillo, N. M.; Nelms, K. M.; Roberts, L. S.; Goenaga, G.; Imel, A.; Barth, B. A.; Dadmun, M.; Heroux, L.; Hayes, D. G.; Zawodzinski, T. Electron Transfer in Microemulsion-Based Electrolytes. *ACS Appl. Mater. Interfaces* **2020**, *12* (36), 40213–40219. https://doi.org/10.1021/acsami.0c07028.

(6) Arratia, P. E. Complex Fluids at Work. *Physics* **2011**, *4*, 9. https://doi.org/10.1103/PhysRevLett.106.058301.

(7) Morozov, A.; Spagnolie, S. E. Introduction to Complex Fluids. In *Complex Fluids in Biological Systems: Experiment, Theory, and Computation*; Spagnolie, S. E., Ed.; Biological

and Medical Physics, Biomedical Engineering; Springer: New York, NY, 2015; pp 3–52. https://doi.org/10.1007/978-1-4939-2065-5_1.

(8) McCarthy, N. L. C.; Brooks, N. J. Chapter Three - Using High Pressure to Modulate Lateral Structuring in Model Lipid Membranes. In *Advances in Biomembranes and Lipid Self-Assembly*; Iglič, A., Kulkarni, C. V., Rappolt, M., Eds.; Academic Press, 2016; Vol. 24, pp 75–89. https://doi.org/10.1016/bs.abl.2016.04.004.

(9) Haavisto, S.; Koponen, A. I.; Salmela, J. New Insight into Rheology and Flow Properties of Complex Fluids with Doppler Optical Coherence Tomography. *Front. Chem.* **2014**, *2*. https://doi.org/10.3389/fchem.2014.00027.

(10) Barrat, J.-L.; Hansen, J.-P. *Basic Concepts for Simple and Complex Liquids*; Cambridge University Press, 2003.

(11) Kiselev, M. A.; Lombardo, D. Structural Characterization in Mixed Lipid Membrane Systems by Neutron and X-Ray Scattering. *Biochim. Biophys. Acta BBA - Gen. Subj.* **2017**, *1861* (1, Part B), 3700–3717. https://doi.org/10.1016/j.bbagen.2016.04.022.

(12) Santos, N. C.; Sousa, A. M. A.; Betbeder, D.; Prieto, M.; Castanho, M. A. R. B. Structural Characterization of Organized Systems of Polysaccharides and Phospholipids by Light Scattering Spectroscopy and Electron Microscopy. *Carbohydr. Res.* **1997**, *300* (1), 31–40. https://doi.org/10.1016/S0008-6215(97)00025-6.

(13) *Structural characterization (shape and dimensions) and stability of polysaccharide/lipid nanoparticles - Santos - 1997 - Biopolymers - Wiley Online Library*. https://onlinelibrary-wiley-com.utk.idm.oclc.org/doi/abs/10.1002/(SICI)1097-0282(19970415)41:5%3C511::AID-BIP3%3E3.0.CO;2-P (accessed 2024-08-05).

(14) Wilson, R. E.; Youtz, M. A. The Importance of Diffusion In Organic Electrochemistry, 1923.

(15) Shen, X.; Sinclair, N.; Wainright, J.; Imel, A.; Barth, B.; Zawodzinski, T.; Savinell, R. F. A Study of Ferrocene Diffusion in Toluene/Tween 20/1-Butanol/Water Microemulsions for Redox Flow Battery Applications. *J. Electrochem. Soc.* **2021**, *168* (6), 060539. https://doi.org/10.1149/1945-7111/ac0b26.

(16) Barth, B. A.; Imel, A.; Nelms, K. M.; Goenaga, G. A.; Zawodzinski, T. Microemulsions: Breakthrough Electrolytes for Redox Flow Batteries. *Front. Chem.* **2022**, *10*, 831200. https://doi.org/10.3389/fchem.2022.831200.

(17) Lourenssen, K.; Williams, J.; Ahmadpour, F.; Clemmer, R.; Tasnim, S. Vanadium Redox Flow Batteries: A Comprehensive Review. *J. Energy Storage* **2019**, *25*, 100844. https://doi.org/10.1016/j.est.2019.100844.

(18) Lee, P. I. Modeling of Drug Release from Matrix Systems Involving Moving Boundaries: Approximate Analytical Solutions. *Int. J. Pharm.* **2011**, *418* (1), 18–27. https://doi.org/10.1016/j.ijpharm.2011.01.019.

(19) Siepmann, J.; Siepmann, F. Modeling of Diffusion Controlled Drug Delivery. *J. Controlled Release* **2012**, *161* (2), 351–362. https://doi.org/10.1016/j.jconrel.2011.10.006.

(20) *Drug release modeled by dissolution, diffusion, and immobilization - ScienceDirect*. https://www-sciencedirect-com.utk.idm.oclc.org/science/article/pii/S0378517302005392 (accessed 2024-08-19).

(21) Streubel, A.; Siepmann, J.; Peppas, N. A.; Bodmeier, R. Bimodal Drug Release Achieved with Multi-Layer Matrix Tablets: Transport Mechanisms and Device Design. *J. Controlled Release* **2000**, *69* (3), 455–468. https://doi.org/10.1016/S0168-3659(00)00334-5.

(22) Helbling, I. M.; Ibarra, J. C. D.; Luna, J. A.; Cabrera, M. I.; Grau, R. J. A. Modeling of Dispersed-Drug Delivery from Planar Polymeric Systems: Optimizing Analytical Solutions. *Int. J. Pharm.* **2010**, *400* (1), 131–137. https://doi.org/10.1016/j.ijpharm.2010.08.043.

(23) Piradashvili, K.; Alexandrino, E. M.; Wurm, F. R.; Landfester, K. Reactions and Polymerizations at the Liquid–Liquid Interface. *Chem. Rev.* **2016**, *116* (4), 2141–2169. https://doi.org/10.1021/acs.chemrev.5b00567.

(24) Fuller, G. G.; Vermant, J. Complex Fluid-Fluid Interfaces: Rheology and Structure. *Annu. Rev. Chem. Biomol. Eng.* **2012**, *3*, 519–543. https://doi.org/10.1146/annurev-chembioeng-061010-114202.

(25) Cheung, D. L. Complex Molecules at Liquid Interfaces: Insights from Molecular Simulation. *Adv. Chem.* **2014**, *2014* (1), 567180. https://doi.org/10.1155/2014/567180.

(26) Ngai, K. L. Alternative Explanation of the Difference between Translational Diffusion and Rotational Diffusion in Supercooled Liquids. *J. Phys. Chem. B* **1999**, *103* (48), 10684–10694. https://doi.org/10.1021/jp990554s.

(27) Cussler, E. L. *Diffusion: Mass Transfer in Fluid Systems*; Cambridge University Press, 2009.

(28) Unni, M.; Savliwala, S.; Partain, B. D.; Maldonado-Camargo, L.; Zhang, Q.; Narayanan, S.; Dufresne, E. M.; Ilavsky, J.; Grybos, P.; Koziol, A.; Maj, P.; Szczygiel, R.; Allen, K. D.; Rinaldi-Ramos, C. M. Fast Nanoparticle Rotational and Translational Diffusion in Synovial

Fluid and Hyaluronic Acid Solutions. *Sci. Adv.* **2021**, *7* (27), eabf8467. https://doi.org/10.1126/sciadv.abf8467.

(29) Parker, E. T.; Lollar, P. Measurement of the Translational Diffusion Coefficient and Hydrodynamic Radius of Proteins by Dynamic Light Scattering. *Bio-Protoc.* **2021**, *11* (20), e4195. https://doi.org/10.21769/BioProtoc.4195.

(30) Michalski, J.; Kalwarczyk, T.; Kwapiszewska, K.; Enderlein, J.; Poniewierski, A.; Karpińska, A.; Kucharska, K.; Hołyst, R. Rotational and Translational Diffusion of Biomolecules in Complex Liquids and HeLa Cells. *Soft Matter* **2024**, *20* (29), 5810–5821. https://doi.org/10.1039/D4SM00422A.

(31) Bashardanesh, Z.; Elf, J.; Zhang, H.; van der Spoel, D. Rotational and Translational Diffusion of Proteins as a Function of Concentration. *ACS Omega* **2019**, *4* (24), 20654–20664. https://doi.org/10.1021/acsomega.9b02835.

(32) Yu, L.; Lei, Y.; Ma, Y.; Liu, M.; Zheng, J.; Dan, D.; Gao, P. A Comprehensive Review of Fluorescence Correlation Spectroscopy. *Front. Phys.* **2021**, *9*.

(33) Burguera, J. L.; Burguera, M. Analytical Applications of Emulsions and Microemulsions. *Talanta* **2012**, *96*, 11–20. https://doi.org/10.1016/j.talanta.2012.01.030.

(34) Bancroft, W. D. The Theory of Emulsification, V. *J. Phys. Chem.* **1913**, *17* (6), 501–519. https://doi.org/10.1021/j150141a002.

(35) Beerbower, A.; Hill, M. W. *McCutcheon's Detergents and Emulsifiers*; McCutcheon's Division, Allured Pub., 1974.

(36) Behar-Cohen, F. Recent Advances in Slow and Sustained Drug Release for Retina Drug Delivery. *Expert Opin. Drug Deliv.* **2019**, *16* (7), 679–686. https://doi.org/10.1080/17425247.2019.1618829.

(37) Deshpande, A. A.; Rhodes, C. T.; Shah, N. H.; Malick, A. W. Controlled-Release Drug Delivery Systems for Prolonged Gastric Residence: An Overview. *Drug Dev. Ind. Pharm.* **1996**. https://doi.org/10.3109/03639049609108355.

(38) Salager, J.-L.; Marquez, R.; Rondón, M.; Bullón, J.; Graciaa, A. Review on Some Confusion Produced by the Bicontinuous Microemulsion Terminology and Its Domains Microcurvature: A Simple Spatiotemporal Model at Optimum Formulation of Surfactant-Oil-Water Systems. *ACS Omega* **2023**, *8* (10), 9040–9057. https://doi.org/10.1021/acsomega.3c00547.

(39) Wade, W. H.; Morgan, J. C.; Schechter, R. S.; Jacobson, J. K.; Salager, J. L. Interfacial Tension and Phase Behavior of Surfactant Systems. *Soc. Pet. Eng. J.* **1978**, *18* (04), 242–252. https://doi.org/10.2118/6844-PA.

(40) Salager, J. L.; Morgan, J. C.; Schechter, R. S.; Wade, W. H.; Vasquez, E. Optimum Formulation of Surfactant/Water/Oil Systems for Minimum Interfacial Tension or Phase Behavior. *Soc. Pet. Eng. J.* **1979**, *19* (02), 107–115. https://doi.org/10.2118/7054-PA.

(41) Salager, J.-L. Microemulsions. In *Handbook of Detergents, Part A*; CRC Press, 1999.

(42) Kunitake, M.; Sakata, K.; Nishimi, T.; Kunitake, M.; Sakata, K.; Nishimi, T. Mesostructured Polymer Materials Based on Bicontinuous Microemulsions. In *Microemulsions - An Introduction to Properties and Applications*; IntechOpen, 2012. https://doi.org/10.5772/38642.

(43) Hayes, D. G.; Ye, R.; Dunlap, R. N.; Anunciado, D. B.; Pingali, S. V.; O'Neill, H. M.; Urban, V. S. Bicontinuous Microemulsions as a Biomembrane Mimetic System for Melittin. *Biochim. Biophys. Acta BBA - Biomembr.* **2018**, *1860* (2), 624–632. https://doi.org/10.1016/j.bbamem.2017.11.005.

(44) Wellert, S.; Karg, M.; Imhof, H.; Steppin, A.; Altmann, H.-J.; Dolle, M.; Richardt, A.; Tiersch, B.; Koetz, J.; Lapp, A.; Hellweg, T. Structure of Biodiesel Based Bicontinuous Microemulsions for Environmentally Compatible Decontamination: A Small Angle Neutron Scattering and Freeze Fracture Electron Microscopy Study. *J. Colloid Interface Sci.* **2008**, *325* (1), 250–258. https://doi.org/10.1016/j.jcis.2008.05.062.

(45) Trotta, M. Influence of Phase Transformation on Indomethacin Release from Microemulsions. *J. Control. Release Off. J. Control. Release Soc.* **1999**, *60* (2–3), 399–405. https://doi.org/10.1016/s0168-3659(99)00094-2.

(46) Jiao, J. Polyoxyethylated Nonionic Surfactants and Their Applications in Topical Ocular Drug Delivery. *Adv. Drug Deliv. Rev.* **2008**, *60* (15), 1663–1673. https://doi.org/10.1016/j.addr.2008.09.002.

(47) Shah, M. R.; Imran, M.; Ullah, S. Chapter 11 - Niosomal Drug Delivery. In *Lipid-Based Nanocarriers for Drug Delivery and Diagnosis*; Shah, M. R., Imran, M., Ullah, S., Eds.; Micro and Nano Technologies; William Andrew Publishing, 2017; pp 317–342. https://doi.org/10.1016/B978-0-323-52729-3.00011-1.

(48) Seldes, D. *Adjuvants 101: Nonionic Surfactants*. Brewer International. https://brewerint.com/news-insights/101-guides/adjuvants-101-nonionic-surfactants/ (accessed 2024-08-13).

(49) Rana, A. A.; Yusaf, A.; Shahid, S.; Usman, M.; Ahmad, M.; Aslam, S.; Al-Hussain, S. A.; Zaki, M. E. A. Unveiling the Role of Nonionic Surfactants in Enhancing Cefotaxime Drug Solubility: A UV-Visible Spectroscopic Investigation in Single and Mixed Micellar Formulations. *Pharmaceuticals* **2023**, *16* (12), 1663. https://doi.org/10.3390/ph16121663.

(50) Ferreira, T. M.; Bernin, D.; Topgaard, D. Chapter Three - NMR Studies of Nonionic Surfactants. In *Annual Reports on NMR Spectroscopy*; Webb, G. A., Ed.; Academic Press, 2013; Vol. 79, pp 73–127. https://doi.org/10.1016/B978-0-12-408098-0.00003-3.

(51) Holmberg, K.; Jonsson, B.; Kronberg, B.; Lindmann, B. *Surfactants and Polymers in Aqueous Solution, 2nd ed. | Sigma-Aldrich*. http://www.sigmaaldrich.com/ (accessed 2022-09-05).

(52) Lipshutz, B.; Ghorai, S. Transition-Metal-Catalyzed Cross-Couplings Going Green: In Water at Room Temperature. *Aldrichimica Acta* **2008**, *41*.

(53) Yamamoto, J.; Suzuki, Y.; Ogawa, Y.; Kamata, T.; Hashimoto, H.; Kunitake, M.; Kato, D. Lipophilic Probe Behavior in Microemulsions Evaluated by Fluorescence Correlation Spectroscopy. *Anal. Sci. Int. J. Jpn. Soc. Anal. Chem.* **2022**, *38* (2), 401–408. https://doi.org/10.2116/analsci.21P316.

(54) Acosta, E. J.; Yuan, J. Sh.; Bhakta, A. Sh. The Characteristic Curvature of Ionic Surfactants. *J. Surfactants Deterg.* **2008**, *11* (2), 145–158. https://doi.org/10.1007/s11743-008-1065-7.

(55) Gonçalves, R. A.; Holmberg, K.; Lindman, B. Cationic Surfactants: A Review. *J. Mol. Liq.* **2023**, *375*, 121335. https://doi.org/10.1016/j.molliq.2023.121335.

(56) Murray, C. J. L.; Ikuta, K. S.; Sharara, F.; Swetschinski, L.; Aguilar, G. R.; Gray, A.; Han, C.; Bisignano, C.; Rao, P.; Wool, E.; Johnson, S. C.; Browne, A. J.; Chipeta, M. G.; Fell, F.; Hackett, S.; Haines-Woodhouse, G.; Hamadani, B. H. K.; Kumaran, E. A. P.; McManigal, B.; Achalapong, S.; Agarwal, R.; Akech, S.; Albertson, S.; Amuasi, J.; Andrews, J.; Aravkin, A.; Ashley, E.; Babin, F.-X.; Bailey, F.; Baker, S.; Basnyat, B.; Bekker, A.; Bender, R.; Berkley, J. A.; Bethou, A.; Bielicki, J.; Boonkasidecha, S.; Bukosia, J.; Carvalheiro, C.; Castañeda-Orjuela, C.; Chansamouth, V.; Chaurasia, S.; Chiurchiù, S.; Chowdhury, F.; Donatien, R. C.; Cook, A. J.; Cooper, B.; Cressey, T. R.; Criollo-Mora, E.; Cunningham, M.; Darboe, S.; Day, N. P. J.; Luca, M. D.; Dokova, K.; Dramowski, A.; Dunachie, S. J.; Bich, T. D.; Eckmanns, T.; Eibach, D.; Emami, A.; Feasey, N.; Fisher-Pearson, N.; Forrest, K.; Garcia, C.; Garrett, D.; Gastmeier, P.; Giref, A. Z.; Greer, R. C.; Gupta, V.; Haller, S.; Haselbeck, A.; Hay, S. I.; Holm, M.; Hopkins, S.; Hsia, Y.; Iregbu, K. C.; Jacobs, J.; Jarovsky, D.; Javanmardi, F.; Jenney, A. W. J.; Khorana, M.; Khusuwan, S.; Kissoon, N.; Kobeissi, E.; Kostyanev, T.; Krapp, F.; Krumkamp, R.; Kumar, A.; Kyu, H. H.; Lim, C.; Lim, K.; Limmathurotsakul, D.; Loftus, M. J.; Lunn, M.; Ma, J.; Manoharan, A.; Marks, F.; May, J.; Mayxay, M.; Mturi, N.; Munera-Huertas, T.; Musicha, P.; Musila, L. A.; Mussi-Pinhata, M. M.; Naidu, R. N.; Nakamura, T.; Nanavati, R.; Nangia, S.; Newton, P.; Ngoun, C.; Novotney, A.; Nwakanma, D.; Obiero, C. W.; Ochoa, T. J.; Olivas-Martinez, A.; Olliaro, P.; Ooko, E.; Ortiz-Brizuela, E.; Ounchanum, P.; Pak, G. D.; Paredes, J. L.; Peleg, A. Y.; Perrone, C.; Phe, T.; Phommasone, K.; Plakkal, N.; Ponce-de-Leon, A.; Raad, M.; Ramdin, T.; Rattanavong, S.; Riddell, A.; Roberts, T.; Robotham, J. V.; Roca, A.; Rosenthal, V. D.; Rudd, K. E.; Russell, N.; Sader, H. S.; Saengchan, W.; Schnall, J.; Scott, J. A. G.;

Seekaew, S.; Sharland, M.; Shivamallappa, M.; Sifuentes-Osornio, J.; Simpson, A. J.; Steenkeste, N.; Stewardson, A. J.; Stoeva, T.; Tasak, N.; Thaiprakong, A.; Thwaites, G.; Tigoi, C.; Turner, C.; Turner, P.; Doorn, H. R. van; Velaphi, S.; Vongpradith, A.; Vongsouvath, M.; Vu, H.; Walsh, T.; Walson, J. L.; Waner, S.; Wangrangsimakul, T.; Wannapinij, P.; Wozniak, T.; Sharma, T. E. M. W. Y.; Yu, K. C.; Zheng, P.; Sartorius, B.; Lopez, A. D.; Stergachis, A.; Moore, C.; Dolecek, C.; Naghavi, M. Global Burden of Bacterial Antimicrobial Resistance in 2019: A Systematic Analysis. *The Lancet* **2022**, *399* (10325), 629–655. https://doi.org/10.1016/S0140-6736(21)02724-0.

(57) Kaneda, T. Iso- and Anteiso-Fatty Acids in Bacteria: Biosynthesis, Function, and Taxonomic Significance. *Microbiol. Rev.* **1991**, *55* (2), 288–302. https://doi.org/10.1128/mr.55.2.288-302.1991.

(58) Walde, P.; Cosentino, K.; Engel, H.; Stano, P. Giant Vesicles: Preparations and Applications. *ChemBioChem* **2010**, *11* (7), 848–865. https://doi.org/10.1002/cbic.201000010.

(59) Schwille, P.; Korlach, J.; Webb, W. W. Fluorescence Correlation Spectroscopy with Single-Molecule Sensitivity on Cell and Model Membranes. *Cytometry* **1999**, *36* (3), 176–182. https://doi.org/10.1002/(SICI)1097-0320(19990701)36:3<176::AID-CYTO5>3.0.CO;2-F.

(60) Kahya, N.; Scherfeld, D.; Bacia, K.; Schwille, P. Lipid Domain Formation and Dynamics in Giant Unilamellar Vesicles Explored by Fluorescence Correlation Spectroscopy. *J. Struct. Biol.* **2004**, *147* (1), 77–89. https://doi.org/10.1016/j.jsb.2003.09.021.

(61) Korlach, J.; Schwille, P.; Webb, W. W.; Feigenson, G. W. *Characterization of lipid bilayer phases by confocal microscopy and fluorescence correlation spectroscopy*. https://doi.org/10.1073/pnas.96.15.8461.

(62) Korlach, J.; Baumgart, T.; Webb, W. W.; Feigenson, G. W. Detection of Motional Heterogeneities in Lipid Bilayer Membranes by Dual Probe Fluorescence Correlation Spectroscopy. *Biochim. Biophys. Acta* **2005**, *1668* (2), 158–163. https://doi.org/10.1016/j.bbamem.2004.11.016.

(63) Gielen, E.; vandeVen, M.; Margineanu, A.; Dedecker, P.; Auweraer, M. V. der; Engelborghs, Y.; Hofkens, J.; Ameloot, M. On the Use of *Z*-Scan Fluorescence Correlation Experiments on Giant Unilamellar Vesicles. *Chem. Phys. Lett.* **2009**, *469* (1), 110–114. https://doi.org/10.1016/j.cplett.2008.12.061.

(64) Rhoades, E.; Ramlall, T. F.; Webb, W. W.; Eliezer, D. Quantification of α-Synuclein Binding to Lipid Vesicles Using Fluorescence Correlation Spectroscopy. *Biophys. J.* **2006**, *90* (12), 4692–4700. https://doi.org/10.1529/biophysj.105.079251.

(65) Jameson, D. M. *Introduction to Fluorescence*; Taylor & Francis, 2014.

(66) *XXX. On the change of refrangibility of light | Philosophical Transactions of the Royal Society of London*. https://royalsocietypublishing.org/doi/10.1098/rstl.1852.0022 (accessed 2024-07-27).

(67) Muk Ng, S.; Koneswaran, M.; Narayanaswamy, R. A Review on Fluorescent Inorganic Nanoparticles for Optical Sensing Applications. *RSC Adv.* **2016**, *6* (26), 21624–21661. https://doi.org/10.1039/C5RA24987B.

(68) Sanderson, M. J.; Smith, I.; Parker, I.; Bootman, M. D. Fluorescence Microscopy. *Cold Spring Harb. Protoc.* **2014**, *2014* (10), pdb.top071795. https://doi.org/10.1101/pdb.top071795.

(69) Choyke, P. L.; Kobayashi, H. Medical Uses of Fluorescence Imaging: Bringing Disease to Light. *IEEE J. Sel. Top. Quantum Electron.* **2012**, *18* (3), 1140–1146. https://doi.org/10.1109/JSTQE.2011.2164900.

(70) Jablonski, A. Efficiency of Anti-Stokes Fluorescence in Dyes. *Nature* **1933**, *131* (3319), 839–840. https://doi.org/10.1038/131839b0.

(71) *Two-Photon Excitation Microscopy for the Study of Living Cells and Tissues - Benninger - 2013 - Current Protocols in Cell Biology - Wiley Online Library*. https://currentprotocols.onlinelibrary.wiley.com/doi/epdf/10.1002/0471143030.cb0411s59 (accessed 2024-07-14).

(72) *One vs two-photon microscopy*. Biodock. https://blog.biodock.ai/one-vs-two-photon-microscopy/ (accessed 2024-07-14).

(73) Bush, P. G.; Wokosin, D. L.; Hall, A. C. Two-versus One Photon Excitation Laser Scanning Microscopy: Critical Importance of Excitation Wavelength. *Front. Biosci. J. Virtual Libr.* **2007**, *12*, 2646–2657.

(74) Keller, U. Recent Developments in Compact Ultrafast Lasers. *Nature* **2003**, *424* (6950), 831–838. https://doi.org/10.1038/nature01938.

(75) Piston, D. W. Choosing Objective Lenses: The Importance of Numerical Aperture and Magnification in Digital Optical Microscopy. *Biol. Bull.* **1998**, *195* (1), 1–4. https://doi.org/10.2307/1542768.

(76) Goodman, D. Encyclopedia of Molecular Biology. *CHOICE Curr. Rev. Acad. Libr.* **1999**, *37* (3), 510-.

(77) *Ueber Diffusion - Fick - 1855 - Annalen der Physik - Wiley Online Library*. https://onlinelibrary-wiley-com.utk.idm.oclc.org/doi/10.1002/andp.18551700105 (accessed 2024-07-27).

(78) Wrede, O.; Großkopf, S.; Seidel, T.; Hellweg, T. Dynamics of Proteins Confined in Non-Ionic Bicontinuous Microemulsions: A FCS Study. *Phys. Chem. Chem. Phys.* **2019**, *21* (12), 6725–6731. https://doi.org/10.1039/C8CP06419A.

(79) Lakowicz, J. R. *Principles of Fluorescence Spectroscopy*; 2006.

(80) Magde, D.; Elson, E.; Webb, W. W. Thermodynamic Fluctuations in a Reacting System---Measurement by Fluorescence Correlation Spectroscopy. *Phys. Rev. Lett.* **1972**, *29* (11), 705–708. https://doi.org/10.1103/PhysRevLett.29.705.

(81) Rigler, R.; Mets, U. Diffusion of Single Molecules through a Gaussian Laser Beam. In *Laser Spectroscopy of Biomolecules*; SPIE, 1993; Vol. 1921, pp 239–248. https://doi.org/10.1117/12.146154.

(82) *What is a molar extinction coefficient? | AAT Bioquest*. https://www.aatbio.com/resources/faq-frequently-asked-questions/What-is-a-molar-extinction-coefficient (accessed 2024-07-15).

(83) Ries, J.; Schwille, P. Fluorescence Correlation Spectroscopy. *BioEssays* **2012**, *34* (5), 361–368. https://doi.org/10.1002/bies.201100111.

(84) Hess, S. T.; Webb, W. W. Focal Volume Optics and Experimental Artifacts in Confocal Fluorescence Correlation Spectroscopy. *Biophys. J.* **2002**, *83* (4), 2300–2317.

(85) Schwille, P.; Haupts, U.; Maiti, S.; Webb, W. W. Molecular Dynamics in Living Cells Observed by Fluorescence Correlation Spectroscopy with One- and Two-Photon Excitation. *Biophys. J.* **1999**, *77* (4), 2251–2265. https://doi.org/10.1016/S0006-3495(99)77065-7.

(86) Zipfel, W. R.; Williams, R. M.; Webb, W. W. Nonlinear Magic: Multiphoton Microscopy in the Biosciences. *Nat. Biotechnol.* **2003**, *21* (11), 1369–1377. https://doi.org/10.1038/nbt899.

(87) Neubauer, R.; Höhn, S.; Dulle, M.; Lapp, A.; Schulreich, C.; Hellweg, T. Protein Diffusion in a Bicontinuous Microemulsion: Inducing Sub-Diffusion by Tuning the Water Domain Size. *Soft Matter* **2017**, *13* (10), 1998–2003. https://doi.org/10.1039/C6SM02107G.

(88) Berland, K. M.; So, P. T.; Gratton, E. Two-Photon Fluorescence Correlation Spectroscopy: Method and Application to the Intracellular Environment. *Biophys. J.* **1995**, *68* (2), 694–701.

(89) Walmsley, I.; Waxer, L.; Dorrer, C. The Role of Dispersion in Ultrafast Optics. *Rev. Sci. Instrum.* **2001**, *72* (1), 1–29. https://doi.org/10.1063/1.1330575.

(90) Krichevsky, O.; Bonnet, G. Fluorescence Correlation Spectroscopy: The Technique and Its Applications. *Rep. Prog. Phys.* **2002**, *65* (2), 251–297. https://doi.org/10.1088/0034-4885/65/2/203.

(91) Mütze, J.; Iyer, V.; Macklin, J. J.; Colonell, J.; Karsh, B.; Petrášek, Z.; Schwille, P.; Looger, L. L.; Lavis, L. D.; Harris, T. D. Excitation Spectra and Brightness Optimization of Two-Photon Excited Probes. *Biophys. J.* **2012**, *102* (4), 934–944. https://doi.org/10.1016/j.bpj.2011.12.056.

(92) Petrášek, Z.; Schwille, P. Precise Measurement of Diffusion Coefficients Using Scanning Fluorescence Correlation Spectroscopy. *Biophys. J.* **2008**, *94* (4), 1437–1448. https://doi.org/10.1529/biophysj.107.108811.

(93) Berland, K.; Shen, G. Excitation Saturation in Two-Photon Fluorescence Correlation Spectroscopy. *Appl. Opt.* **2003**, *42* (27), 5566–5576. https://doi.org/10.1364/AO.42.005566.

(94) Scriven, L. E. Equilibrium Bicontinuous Structures. In *Micellization, Solubilization, and Microemulsions: Volume 2*; Mittal, K. L., Ed.; Springer US: Boston, MA, 1977; pp 877–893. https://doi.org/10.1007/978-1-4613-4157-4_23.

(95) Sjöblom, J.; Lindberg, R.; Friberg, S. E. Microemulsions — Phase Equilibria Characterization, Structures, Applications and Chemical Reactions. *Adv. Colloid Interface Sci.* **1996**, *65*, 125–287. https://doi.org/10.1016/0001-8686(96)00293-X.

(96) Kaler, E. W.; Prager, S. A Model of Dynamic Scattering by Microemulsions. *J. Colloid Interface Sci.* **1982**, *86* (2), 359–369. https://doi.org/10.1016/0021-9797(82)90081-9.

(97) Kogan, A.; Shalev, D. E.; Raviv, U.; Aserin, A.; Garti, N. Formation and Characterization of Ordered Bicontinuous Microemulsions. *J. Phys. Chem. B* **2009**, *113* (31), 10669–10678. https://doi.org/10.1021/jp901617g.

(98) Schulreich, C.; Angermann, C.; Höhn, S.; Neubauer, R.; Seibt, S.; Stehle, R.; Lapp, A.; Richardt, A.; Diekmann, A.; Hellweg, T. Bicontinuous Microemulsions with Extremely High Temperature Stability Based on Skin Friendly Oil and Sugar Surfactant. *Colloids Surf. Physicochem. Eng. Asp.* **2013**, *418*, 39–46. https://doi.org/10.1016/j.colsurfa.2012.10.039.

(99) Lapteva, M.; Kalia, Y. N. Microstructured Bicontinuous Phase Formulations: Their Characterization and Application in Dermal and Transdermal Drug Delivery. *Expert Opin. Drug Deliv.* **2013**, *10* (8), 1043–1059. https://doi.org/10.1517/17425247.2013.783008.

(100) Lawrence, M. J.; Rees, G. D. Microemulsion-Based Media as Novel Drug Delivery Systems. *Adv. Drug Deliv. Rev.* **2000**, *45* (1), 89–121. https://doi.org/10.1016/S0169-409X(00)00103-4.

(101) Craciun, A. M.; Mititelu Tartau, L.; Pinteala, M.; Marin, L. Nitrosalicyl-Imine-Chitosan Hydrogels Based Drug Delivery Systems for Long Term Sustained Release in Local Therapy. *J. Colloid Interface Sci.* **2019**, *536*, 196–207. https://doi.org/10.1016/j.jcis.2018.10.048.

(102) Sharsheeva, A.; Iglin, V. A.; Nesterov, P. V.; Kuchur, O. A.; Garifullina, E.; Hey-Hawkins, E.; Ulasevich, S. A.; Skorb, E. V.; Vinogradov, A. V.; Morozov, M. I. Light-Controllable Systems Based on TiO2-ZIF-8 Composites for Targeted Drug Release: Communicating with Tumour Cells. *J. Mater. Chem. B* **2019**, *7* (43), 6810–6821. https://doi.org/10.1039/c9tb01377f.

(103) Hassan, M. R.; Colon, B. A.; Russell, J.; Calhoun, T. R. Small Molecule Sorting: A Fluorescence Study of Microemulsions. *J. Phys. Chem. B* **2022**, *126* (26), 4990–4998. https://doi.org/10.1021/acs.jpcb.2c02774.

(104) Bachynsky, M. O.; Shah, N. H.; Patel, C. I.; Malick, A. W. Factors Affecting the Efficiency of a Self-Emulsifying Oral Delivery System. *Drug Dev. Ind. Pharm.* **1997**, *23* (8), 809–816. https://doi.org/10.3109/03639049709150551.

(105) Nagarajan, R. Molecular Packing Parameter and Surfactant Self-Assembly: The Neglected Role of the Surfactant Tail. *Langmuir* **2002**, *18* (1), 31–38. https://doi.org/10.1021/la010831y.

(106) Kato, D.; Yamamoto, J.; Suzuki, Y.; Kamata, T.; Hashimoto, H.; Kunitake, M. Lipophilic Vitamin E Diffusion through Bicontinuous Microemulsions. *Anal. Chem.* **2021**, *93* (42), 14231–14237. https://doi.org/10.1021/acs.analchem.1c03174.

(107) Oliveira, M. E. C. D. R.; Hungerford, G.; Miguel, M. da G.; Burrows, H. D. Solvatochromic Fluorescent Probes in Bicontinuous Microemulsions. *J. Mol. Struct.* **2001**, *563–564*, 443–447. https://doi.org/10.1016/S0022-2860(00)00888-7.

(108) C, G. W. Calculation of HLB Values of Non-Ionic Surfactants. *J Soc Cosmet Chem* **1954**, *5*, 249–256.

(109) Sripriya, R.; Muthu Raja, K.; Santhosh, G.; Chandrasekaran, M.; Noel, M. The Effect of Structure of Oil Phase, Surfactant and Co-Surfactant on the Physicochemical and Electrochemical Properties of Bicontinuous Microemulsion. *J. Colloid Interface Sci.* **2007**, *314* (2), 712–717. https://doi.org/10.1016/j.jcis.2007.05.080.

(110) Liu, Q.; Wang, J.; Wu, H.; Zong, S.; Wang, N.; Wang, T.; Zhou, L.; Huang, X.; Hao, H. Structure and Pseudo-Ternary Phase Diagram of Water/Triton X-100/1-Pentanol/Cyclohexane Microemulsion. *J. Mol. Liq.* **2022**, *349*, 118425. https://doi.org/10.1016/j.molliq.2021.118425.

(111) Chiappisi, L.; Noirez, L.; Gradzielski, M. A Journey through the Phase Diagram of a Pharmaceutically Relevant Microemulsion System. *J. Colloid Interface Sci.* **2016**, *473*, 52–59. https://doi.org/10.1016/j.jcis.2016.03.064.

(112) Moulik, S. P.; Paul, B. K. Structure, Dynamics and Transport Properties of Microemulsions. *Adv. Colloid Interface Sci.* **1998**, *78* (2), 99–195. https://doi.org/10.1016/S0001-8686(98)00063-3.

(113) Moulik, S. P.; Das, M. L.; Bhattacharya, P. K.; Das, A. R. Thermodynamics of Microemulsion Formation. 1. Enthalpy of Solution of Water in Binary (Triton X 100 + Butanol) and Ternary (Heptane + Triton X 100 + Butanol) Mixtures and Heat Capacity of the Resulting Systems. *Langmuir* **1992**, *8* (9), 2135–2139. https://doi.org/10.1021/la00045a012.

(114) Bisal, S. R.; Bhattacharya, P. K.; MouIik, S. P. Phase Behaviour and Physicochemical Properties of Triton X 100 and Aerosol OT Induced Micro Emulsions of Hydrocarbons and Water in Presence of N-Butanol. *IJC- Vol28A07 July 1989* **1989**.

(115) Kurniasih, I. N.; Liang, H.; Mohr, P. C.; Khot, G.; Rabe, J. P.; Mohr, A. Nile Red Dye in Aqueous Surfactant and Micellar Solution. *Langmuir* **2015**, *31* (9), 2639–2648. https://doi.org/10.1021/la504378m.

(116) Song, M.; Wang, Q.; Liu, W.; Wang, J.; Chai, J. Composition and Solubilization of the Microemulsion Systems Containing Triton X-100: Effects of Aqueous Composition and Oil-Water-Ratios. *Tenside Surfactants Deterg.* **2020**, *57* (2), 138–145. https://doi.org/10.3139/113.110671.

(117) Müller, C. B.; Loman, A.; Pacheco, V.; Koberling, F.; Willbold, D.; Richtering, W.; Enderlein, J. Precise Measurement of Diffusion by Multi-Color Dual-Focus Fluorescence Correlation Spectroscopy. *Europhys. Lett.* **2008**, *83* (4), 46001. https://doi.org/10.1209/0295-5075/83/46001.

(118) Lindman, B.; Shinoda, K.; Olsson, U.; Anderson, D.; Karlström, G.; Wennerström, H. On the Demonstration of Bicontinuous Structures in Microemulsions. *Colloids Surf.* **1989**, *38* (1), 205–224. https://doi.org/10.1016/0166-6622(89)80154-4.

(119) Frank, C.; Frielinghaus, H.; Allgaier, J.; Prast, H. Nonionic Surfactants with Linear and Branched Hydrocarbon Tails: Compositional Analysis, Phase Behavior, and Film Properties in Bicontinuous Microemulsions. *Langmuir* **2007**, *23* (12), 6526–6535. https://doi.org/10.1021/la0637115.

(120) Guo, R.; Zhang, X.; Guo, X. The Phase Behavior and the Structural Properties of Triton X-100/n-C8H17OH/PEG1000aq System. *J. Dispers. Sci. Technol.* **2001**, *22* (5), 443–451. https://doi.org/10.1081/DIS-100107853.

(121) Guo, J.; Baker, G. A.; Hillesheim, P. C.; Dai, S.; Shaw, R. W.; Mahurin, S. M. Fluorescence Correlation Spectroscopy Evidence for Structural Heterogeneity in Ionic Liquids. *Phys. Chem. Chem. Phys.* **2011**, *13* (27), 12395–12398. https://doi.org/10.1039/C1CP20929A.

(122) *Molecular Dynamics Simulation Insight into Interfacial Stability and Fluidity Properties of Microemulsions | Langmuir*. https://pubs-acs-org.utk.idm.oclc.org/doi/full/10.1021/acs.langmuir.9b02325 (accessed 2024-08-24).

(123) Israelachvili, J. N.; Mitchell, D. J.; Ninham, B. W. Theory of Self-Assembly of Lipid Bilayers and Vesicles. *Biochim. Biophys. Acta BBA - Biomembr.* **1977**, *470* (2), 185–201. https://doi.org/10.1016/0005-2736(77)90099-2.

(124) Khalil, R. A.; Zarari, A. A. Theoretical Estimation of the Critical Packing Parameter of Amphiphilic Self-Assembled Aggregates. *Appl. Surf. Sci.* **2014**, *318*, 85–89. https://doi.org/10.1016/j.apsusc.2014.01.046.

(125) Gracie, K.; Turner, D.; Palepu, R. Thermodynamic Properties of Micellization of Sodium Dodecyl Sulfate in Binary Mixtures of Ethylene Glycol with Water. *Can. J. Chem.* **2011**, *74*, 1616–1625. https://doi.org/10.1139/v96-179.

(126) Chakraborty, T.; Ghosh, S.; Moulik, S. P. Micellization and Related Behavior of Binary and Ternary Surfactant Mixtures in Aqueous Medium: Cetyl Pyridinium Chloride (CPC), Cetyl Trimethyl Ammonium Bromide (CTAB), and Polyoxyethylene (10) Cetyl Ether (Brij-56) Derived System. *J. Phys. Chem. B* **2005**, *109* (31), 14813–14823. https://doi.org/10.1021/jp044580o.

(127) Lutz-Bueno, V.; Isabettini, S.; Walker, F.; Kuster, S.; Liebi, M.; Fischer, P. Ionic Micelles and Aromatic Additives: A Closer Look at the Molecular Packing Parameter. *Phys. Chem. Chem. Phys.* **2017**, *19* (32), 21869–21877. https://doi.org/10.1039/C7CP03891G.

(128) Chieng, T. H.; Gan, L. M.; Teot, W. K.; Pey, K. L. Porous Polymeric Membranes by Bicontinuous Microemulsion Polymerization: Effect of Anionic and Cationic Surfactants. *Polymer* **1996**, *37* (26), 5917–5925. https://doi.org/10.1016/S0032-3861(96)00452-1.

(129) Li, X.; Lin, E.; Zhao, G.; Xiao, T. Microemulsion Formation and Phase Behavior of Anionic and Cationic Surfactants with Sodium Dodecyl Sulfate and Cetyltrimethylammonium Bromide. *J. Colloid Interface Sci.* **1996**, *184* (1), 20–30. https://doi.org/10.1006/jcis.1996.0593.

(130) *Rheology of Complex Fluids*; Krishnan, J. M., Deshpande, A. P., Kumar, P. B. S., Eds.; Springer: New York, NY, 2010. https://doi.org/10.1007/978-1-4419-6494-6.

(131) Schulz, H.; Simoes, A.; Lobosco, R. *Hydrodynamics: Advanced Topics*; BoD – Books on Demand, 2011.

(132) Ries, J.; Schwille, P. New Concepts for Fluorescence Correlation Spectroscopy on Membranes. *Phys. Chem. Chem. Phys.* **2008**, *10* (24), 3487–3497. https://doi.org/10.1039/B718132A.

(133) Winkler, R. *Diffusion and segmental dynamics of rodlike molecules by fluorescence correlation spectroscopy | The Journal of Chemical Physics | AIP Publishing*. https://pubs.aip.org/aip/jcp/article-abstract/127/5/054904/931244/Diffusion-and-segmental-dynamics-of-rodlike?redirectedFrom=fulltext (accessed 2024-08-17).

(134) Zana, R. Microviscosity of Aqueous Surfactant Micelles: Effect of Various Parameters. *J. Phys. Chem. B* **1999**, *103* (43), 9117–9125. https://doi.org/10.1021/jp990347s.

(135) Goins, A. B.; Sanabria, H.; Waxham, M. N. Macromolecular Crowding and Size Effects on Probe Microviscosity. *Biophys. J.* **2008**, *95* (11), 5362–5373. https://doi.org/10.1529/biophysj.108.131250.

(136) Jay, A. G.; Hamilton, J. A. Disorder Amidst Membrane Order: Standardizing Laurdan Generalized Polarization and Membrane Fluidity Terms. *J. Fluoresc.* **2017**, *27* (1), 243–249. https://doi.org/10.1007/s10895-016-1951-8.

(137) Parasassi, T.; Di Stefano, M.; Loiero, M.; Ravagnan, G.; Gratton, E. Influence of Cholesterol on Phospholipid Bilayers Phase Domains as Detected by Laurdan Fluorescence. *Biophys. J.* **1994**, *66* (1), 120–132. https://doi.org/10.1016/S0006-3495(94)80763-5.

(138) Orlikowska-Rzeznik, H.; Krok, E.; Chattopadhyay, M.; Lester, A.; Piatkowski, L. Laurdan Discerns Lipid Membrane Hydration and Cholesterol Content. *J. Phys. Chem. B* **2023**, *127* (15), 3382–3391. https://doi.org/10.1021/acs.jpcb.3c00654.

(139) Lakowicz, J. R.; Gryczynski, I.; Kuśba, J.; Danielsen, E. Two Photon-Induced Fluorescence Intensity and Anisotropy Decays of Diphenylhexatriene in Solvents and Lipid Bilayers. *J. Fluoresc.* **1992**, *2* (4), 247–258. https://doi.org/10.1007/BF00865283.

(140) Kuhry, J.-G.; Duportail, G.; Bronner, C.; Laustriat, G. Plasma Membrane Fluidity Measurements on Whole Living Cells by Fluorescence Anisotropy of Trimethylammoniumdiphenylhexatriene. *Biochim. Biophys. Acta BBA - Mol. Cell Res.* **1985**, *845* (1), 60–67. https://doi.org/10.1016/0167-4889(85)90055-2.

(141) Duportail, G.; Weinreb, A. Photochemical Changes of Fluorescent Probes in Membranes and Their Effect on the Observed Fluorescence Anisotropy Values. *Biochim. Biophys. Acta BBA - Biomembr.* **1983**, *736* (2), 171–177. https://doi.org/10.1016/0005-2736(83)90281-X.

(142) Fraňová, M.; Repáková, J.; Čapková, P.; Holopainen, J. M.; Vattulainen, I. Effects of DPH on DPPC−Cholesterol Membranes with Varying Concentrations of Cholesterol: From Local Perturbations to Limitations in Fluorescence Anisotropy Experiments. *J. Phys. Chem. B* **2010**, *114* (8), 2704–2711. https://doi.org/10.1021/jp908533x.

(143) Blaffert, J.; Haeri, H. H.; Blech, M.; Hinderberger, D.; Garidel, P. Spectroscopic Methods for Assessing the Molecular Origins of Macroscopic Solution Properties of Highly Concentrated Liquid Protein Solutions. *Anal. Biochem.* **2018**, *561–562*, 70–88. https://doi.org/10.1016/j.ab.2018.09.013.

(144) Takahashi, D.; Nishimoto, E.; Murase, T.; Yamashita, S. Protein-Protein Interaction on Lysozyme Crystallization Revealed by Rotational Diffusion Analysis. *Biophys. J.* **2008**, *94* (11), 4484–4492. https://doi.org/10.1529/biophysj.107.111872.

(145) *The Fluid Mosaic Model of the Structure of Cell Membranes | Science*. https://www-science-org.utk.idm.oclc.org/doi/abs/10.1126/science.175.4023.720 (accessed 2024-08-08).

(146) Alberts, B.; Johnson, A.; Lewis, J.; Raff, M.; Roberts, K.; Walter, P. The Lipid Bilayer. In *Molecular Biology of the Cell. 4th edition*; Garland Science, 2002.

(147) Lopez, D.; Koch, G. Exploring Functional Membrane Microdomains in Bacteria: An Overview. *Curr. Opin. Microbiol.* **2017**, *36*, 76–84. https://doi.org/10.1016/j.mib.2017.02.001.

(148) Levental, I.; Lyman, E. Regulation of Membrane Protein Structure and Function by Their Paralipidomes. *Nat. Rev. Mol. Cell Biol.* **2023**, *24* (2), 107–122. https://doi.org/10.1038/s41580-022-00524-4.

(149) Michel, V.; Bakovic, M. Lipid Rafts in Health and Disease. *Biol. Cell* **2007**, *99* (3), 129–140. https://doi.org/10.1042/BC20060051.

(150) López, D.; Kolter, R. Functional Microdomains in Bacterial Membranes. *Genes Dev.* **2010**, *24* (17), 1893–1902. https://doi.org/10.1101/gad.1945010.

(151) Kaneda, T. Biosynthesis of Branched Chain Fatty Acids. II. Microbial Synthesis of Branched Long Chain Fatty Acids from Certain Short Chain Fatty Acid Substrates. *J. Biol. Chem.* **1963**, *238*, 1229–1235.

(152) Mostofian, B.; Zhuang, T.; Cheng, X.; Nickels, J. D. Branched-Chain Fatty Acid Content Modulates Structure, Fluidity, and Phase in Model Microbial Cell Membranes. *J. Phys. Chem. B* **2019**, *123* (27), 5814–5821. https://doi.org/10.1021/acs.jpcb.9b04326.

(153) Nickels, J. D.; Chatterjee, S.; Mostofian, B.; Stanley, C. B.; Ohl, M.; Zolnierczuk, P.; Schulz, R.; Myles, D. A. A.; Standaert, R. F.; Elkins, J. G.; Cheng, X.; Katsaras, J. Bacillus Subtilis Lipid Extract, A Branched-Chain Fatty Acid Model Membrane. *J. Phys. Chem. Lett.* **2017**, *8* (17). https://doi.org/10.1021/acs.jpclett.7b01877.

(154) Poger, D.; Caron, B.; Mark, A. E. Effect of Methyl-Branched Fatty Acids on the Structure of Lipid Bilayers. *J. Phys. Chem. B* **2014**, *118* (48), 13838–13848. https://doi.org/10.1021/jp503910r.

(155) Rilfors, L. Difference in Packing Properties between Iso and Anteiso Methyl-Branched Fatty Acids as Revealed by Incorporation into the Membrane Lipids of *Acholeplasma Laidlawii* Strain A. *Biochim. Biophys. Acta BBA - Biomembr.* **1985**, *813* (2), 151–160. https://doi.org/10.1016/0005-2736(85)90228-7.

(156) Kannenberg, E.; Blume, A.; McElhaney, R. N.; Poralla, K. Monolayer and Calorimetric Studies of Phosphatidylcholines Containing Branched-Chain Fatty Acids and of Their Interactions with Cholesterol and with a Bacterial Hopanoid in Model Membranes. *Biochim. Biophys. Acta BBA - Biomembr.* **1983**, *733* (1), 111–116. https://doi.org/10.1016/0005-2736(83)90096-2.

(157) Nair, K. S.; Bajaj, H. Advances in Giant Unilamellar Vesicle Preparation Techniques and Applications. *Adv. Colloid Interface Sci.* **2023**, *318*, 102935. https://doi.org/10.1016/j.cis.2023.102935.

(158) Bacia, K.; Haustein, E.; Schwille, P. Fluorescence Correlation Spectroscopy: Principles and Applications. *Cold Spring Harb. Protoc.* **2014**, *2014* (7), pdb.top081802. https://doi.org/10.1101/pdb.top081802.

(159) Sánchez, S. A.; Gratton, E. Lipid−Protein Interactions Revealed by Two-Photon Microscopy and Fluorescence Correlation Spectroscopy. *Acc. Chem. Res.* **2005**, *38* (6), 469–477. https://doi.org/10.1021/ar040026l.

(160) Kahya, N.; Scherfeld, D.; Bacia, K.; Poolman, B.; Schwille, P. Probing Lipid Mobility of Raft-Exhibiting Model Membranes by Fluorescence Correlation Spectroscopy *. *J. Biol. Chem.* **2003**, *278* (30), 28109–28115. https://doi.org/10.1074/jbc.M302969200.

(161) Scherfeld, D.; Kahya, N.; Schwille, P. Lipid Dynamics and Domain Formation in Model Membranes Composed of Ternary Mixtures of Unsaturated and Saturated Phosphatidylcholines and Cholesterol. *Biophys. J.* **2003**, *85* (6), 3758–3768. https://doi.org/10.1016/S0006-3495(03)74791-2.

(162) Demel, R. A.; De Kruyff, B. The Function of Sterols in Membranes. *Biochim. Biophys. Acta* **1976**, *457* (2), 109–132. https://doi.org/10.1016/0304-4157(76)90008-3.

(163) McMullen, T. P.; McElhaney, R. N. Physical Studies of Cholesterol-Phospholipid Interactions. *Curr. Opin. Colloid Interface Sci.* **1996**, *1* (1), 83–90. https://doi.org/10.1016/S1359-0294(96)80048-3.

(164) Lange, Y.; D'Alessandro, J. S.; Small, D. M. The Affinity of Cholesterol for Phosphatidylcholine and Sphingomyelin. *Biochim. Biophys. Acta BBA - Biomembr.* **1979**, *556* (3), 388–398. https://doi.org/10.1016/0005-2736(79)90127-5.

(165) Yeagle, P. L.; Young, J. E. *Factors contributing to the distribution of cholesterol among phospholipid vesicles - PubMed*. https://pubmed-ncbi-nlm-nih-gov.utk.idm.oclc.org/3722148/ (accessed 2024-10-11).

(166) Brzustowicz, M. R.; Cherezov, V.; Caffrey, M.; Stillwell, W.; Wassall, S. R. Molecular Organization of Cholesterol in Polyunsaturated Membranes: Microdomain Formation. *Biophys. J.* **2002**, *82* (1), 285–298. https://doi.org/10.1016/S0006-3495(02)75394-0.

(167) Ohvo-Rekilä, H.; Ramstedt, B.; Leppimäki, P.; Slotte, J. P. Cholesterol Interactions with Phospholipids in Membranes. *Prog. Lipid Res.* **2002**, *41* (1), 66–97. https://doi.org/10.1016/s0163-7827(01)00020-0.

(168) Angelova, M. I.; Dimitrov, D. S. Liposome Electroformation. *Faraday Discuss. Chem. Soc.* **1986**, *81* (0), 303–311. https://doi.org/10.1039/DC9868100303.

(169) Heinemann, F.; Betaneli, V.; Thomas, F. A.; Schwille, P. Quantifying Lipid Diffusion by Fluorescence Correlation Spectroscopy: A Critical Treatise. *Langmuir* **2012**, *28* (37), 13395–13404. https://doi.org/10.1021/la302596h.

(170) Filpula, D. R.; Lee, S.-M.; Link, R. P.; Strausberg, S. L.; Strausberg, R. L. Structural and Functional Repetition in a Marine Mussel Adhesive Protein. *Biotechnol. Prog.* **1990**, *6* (3), 171–177. https://doi.org/10.1021/bp00003a001.

(171) Belkind, A.; Gershman, S. Plasma Cleaning of Surfaces. *Vac Technol Coat* **2008**, 1–11.

(172) Andersen, O. S.; Ii, R. E. K. Bilayer Thickness and Membrane Protein Function: An Energetic Perspective. *Annu. Rev. Biophys.* **2007**, *36* (Volume 36, 2007), 107–130. https://doi.org/10.1146/annurev.biophys.36.040306.132643.

(173) Regan, D.; Williams, J.; Borri, P.; Langbein, W. Lipid Bilayer Thickness Measured by Quantitative DIC Reveals Phase Transitions and Effects of Substrate Hydrophilicity. *Langmuir* **2019**, *35* (43), 13805–13814. https://doi.org/10.1021/acs.langmuir.9b02538.

(174) Yamamoto, J.; Sasaki, A. Fluorescence Correlation Spectroscopy Measurement Based on Fiber Optics for Biological Materials. *Appl. Sci.* **2021**, *11* (15), 6744. https://doi.org/10.3390/app11156744.

(175) *(PDF) Quantitative FCS: Determination of the Confocal Volume by FCS and Bead Scanning with the MicroTime 200*. https://www.researchgate.net/publication/237612337_Quantitative_FCS_Determination_of_the_Confocal_Volume_by_FCS_and_Bead_Scanning_with_the_MicroTime_200 (accessed 2024-10-15).

(176) Bacia, K.; Scherfeld, D.; Kahya, N.; Schwille, P. Fluorescence Correlation Spectroscopy Relates Rafts in Model and Native Membranes. *Biophys. J.* **2004**, *87* (2), 1034–1043. https://doi.org/10.1529/biophysj.104.040519.

(177) Schote, U.; Seelig, J. Interaction of the Neuronal Marker Dye FM1-43 with Lipid Membranes: Thermodynamics and Lipid Ordering. *Biochim. Biophys. Acta BBA - Biomembr.* **1998**, *1415* (1), 135–146. https://doi.org/10.1016/S0005-2736(98)00188-6.

(178) Blake, M. J.; Castillo, H. B.; Curtis, A. E.; Calhoun, T. R. Facilitating Flip-Flop: Structural Tuning of Molecule-Membrane Interactions in Living Bacteria. *Biophys. J.* **2023**, *122* (10), 1735–1747. https://doi.org/10.1016/j.bpj.2023.04.003.

(179) Blake, M. J.; Page, E. F.; Smith, M. E.; Calhoun, T. R. Miltefosine Impacts Small Molecule Transport in Gram-Positive Bacteria. *RSC Chem. Biol.* **2024**, *5* (10), 981–988. https://doi.org/10.1039/D4CB00106K.

(180) Pomorski, T. G.; Menon, A. K. LIPID SOMERSAULTS: UNCOVERING THE MECHANISMS OF PROTEIN-MEDIATED LIPID FLIPPING. *Prog. Lipid Res.* **2016**, *64*, 69. https://doi.org/10.1016/j.plipres.2016.08.003.

(181) Gaede, H. C.; Gawrisch, K. Lateral Diffusion Rates of Lipid, Water, and a Hydrophobic Drug in a Multilamellar Liposome. *Biophys. J.* **2003**, *85* (3), 1734. https://doi.org/10.1016/S0006-3495(03)74603-7.

(182) Mazza, D.; Stasevich, T. J.; Karpova, T. S.; McNally, J. G. Monitoring Dynamic Binding of Chromatin Proteins In Vivo by Fluorescence Correlation Spectroscopy and Temporal Image Correlation Spectroscopy. *Methods Mol. Biol. Clifton NJ* **2012**, *833*, 177. https://doi.org/10.1007/978-1-61779-477-3_12.

VITA

Grant Foley was born in Pittsburgh, PA to Dennis and Kelly Foley. He was raised in Southaven, MS and graduated high school from Desoto Central High School in 2017. Grant then attended Delta State University and graduated with his Bachelor of Science in Chemistry in 2021. Following graduation, Grant was accepted to The University of Tennessee, Knoxville, where he would pursue a graduate degree in analytical chemistry under the guidance of Dr. Tessa Calhoun.